EXPERIMENTAL INVESTIGATION OF THE THERMAL PERFORMANCE OF GAS-COOLED DIVERTOR PLATE CONCEPTS

A Thesis
Presented to
The Academic Faculty

By
Mitchell D. Hageman

In Partial Fulfillment
Of the Requirements for the Degree
Master of Science in Mechanical Engineering

Georgia Institute of Technology

August 2010

EXPERIMENTAL STUDY OF THE THERMAL PERFORMANCE OF GAS-COOLED DIVERTOR PLATE CONCEPTS

Approved by:

Dr. Said I. Abdel-Khalik, Advisor

School of Mechanical Engineering

Georgia Institute of Technology

Dr. Minami Yoda, Advisor

School of Mechanical Engineering

Georgia Institute of Technology

Dr. Seyed Mostafa Ghiaasiaan

School of Mechanical Engineering

Georgia Institute of Technology

Date Approved: 4/29/2010

ACKNOWLEDGEMENTS

Above all, I would like to thank my advisors, Dr. Said Abdel-Khalik and Dr. Minami Yoda for their guidance and encouragement. Both have offered valuable advice throughout this process, and have been more than willing to offer their time, talent and knowledge to help me through any struggles.

A great deal of credit must also be given to Mr. Dennis Sadowski for his knowledge of fabrication, and his expertise in experimental methods. Dennis has had his hand in nearly every piece of the test set-up and test section fabrication. I would also like to thank my predecessor, Elizabeth Gayton. Ms Gayton gave me her time teaching me to set up and run my experiments, helped me become familiar with the lab, and her thesis provided invaluable guidance throughout my research.

Last, I would like to thank my entire family for their support and encouragement in everything I do, and for the guidance they provided which led to this point. Without them, I would not be here.

TABLE OF CONTENTS

LIST OF TABLES

LIST OF FIGURES

LIST OF SYMBOLS AND ABBREVIATIONS:

Common Variables

A	Area	m^2, mm^2
A_c	Surface area of a single pin tip	m^2, mm^2
A_f	Surface area of a pin wall	m^2, mm^2
A_{PFC}	Area of plasma facing component	m^2, mm^2
A_{prime}	Flat area of pin-covered surface	m^2, mm^2
A_{sl}	Slot area	m^2, mm^2
B	Slot width	m, mm
c	Speed of light	m/s
D	Diameter	m, mm
D_h	Hydraulic Diameter	m, mm
E	Energy	Watts
f	Function	
h	Height	m, mm
h	Heat transfer coefficient	W/(m^2-K)
h_{air}	Heat transfer coefficient with air as coolant	W/(m^2-K)
h_{actual}	Actual heat transfer coefficient of pin-covered surface	W/(m^2-K)
h_{actual}^{Air}	Actual heat transfer coefficient using air as the coolant	W/(m^2-K)
h_{actual}^{He}	Actual heat transfer coefficient using helium as the coolant	W/(m^2-K)
h_{avg}	Average heat transfer coefficient	W/(m^2-K)
h_{bare}	Bare surface heat transfer coefficient	W/(m^2-K)
h_{eff}	Effective heat transfer coefficient	W/(m^2-K)
$h_{eff,calc}$	Calculated effective heat transfer coefficient	W/(m^2-K)
h_{eff}^{He}	Heat transfer coefficient with helium as coolant	W/(m^2-K)
$h_{eff,local}$	Local effective heat transfer coefficient	W/(m^2-K)
h_s	Stagnation point heat transfer coefficient	W/(m^2-K)
I	Current	Amperes
k	Thermal conductivity	W/(m-K)
k_{brass}	Thermal conductivity of brass	W/(m-K)
k_{air}	Thermal conductivity of air	W/(m-K)
k_{He}	Thermal conductivity of helium	W/(m-K)
k_W	Thermal conductivity of tungsten	W/(m-K)
l	Length	m, mm
L	Length of a pin fin	m, mm
L_{FP}	Thickness of tungsten-alloy front plate	m, mm
$\dot{m}$	Mass flow rate	g/s, kg/s

n	Neutron	
N	Number of …	
Per	Perimeter	m, mm
P	Pressure	kPa, psi
P_{in}	Inlet gauge pressure	kPa, psi
P_{nom}	Common system pressure	414 kPa, 60 psia
P_{out}	Outlet gauge pressure	kPa, psi
P_{sys}	Average system pressure	kPa, psi
P_{rot}	Pressure at rotameter outlet	kPa, psi
ΔP	Pressure drop	kPa, psi
$\Delta P'$	Normalized pressure drop	kPa, psi
Q	Heat power	W
q	Heat transfer rate	W
q_f	Pin –fin heat transfer rate	W
q_{max}	Maximum possible heat transfer rate	W
q''	Heat flux	W/m^2
q''_{actual}	Measured incident heat flux	MW/m^2
q''_{max}	Maximum predicted heat flux	MW/m^2
q''_{nom}	Nominal incident heat flux	MW/m^2
R	Thermal resistance	K/W
R_{tot}	Total thermal resistance	K/W
$R_{t,conv}$	Convective thermal resistance	K/W
$R_{t,cond}$	Conductive thermal resistance	K/W
T	Temperature	˚C, K
T_{in}	Inlet temperature	˚C, K
T_{out}	Outlet temperature	˚C, K
T_s	Surface temperature	˚C, K
$T_{s,local}$	Local surface temperature	˚C, K
$T_{s,pins}$	Pin-covered surface temperature	˚C, K
T_{TC}	Thermocouple temperature reading	˚C, K
U	Uncertainty	
U_A	Uncertainty due to statistical fluctuations	
U_B	Uncertainty due to instrumentation	
U_C	Uncertainty in current	
U_{HTC}	Uncertainty in heat transfer coefficient	
U_{MFR}	Uncertainty in mass flow rate	
U_T	Uncertainty in temperature	
U_{Total}	Total experimental uncertainty	
U_V	Uncertainty in voltage	
V	Voltage	Volts
$\overline{V}$	Mean velocity	m/s

V_{max}	Jet centerline velocity	m/s
v'	Root mean square of velocity fluctuations	
w	Width	m, mm
X	Lateral distance along impingement plate	m, mm
Z	Perpendicular distance from impingement plate	m, mm
Z_{cr}	Z-location where potential core ends	m, mm
z	Statistical multiplier	

Greek Symbols

η	Efficiency	
η_f	Fin Efficiency	
π	3.1415	
ρ	Density	kg/m^3
ρ_{rot}	Density at rotameter outlet	kg/m^3
μ	Dynamic viscosity	kg/(m-s)
μ_{in}	Inlet coolant viscosity	kg/(m-s)
σ_{sample}	Standard deviation of a sample	
Δ	Change in a property	

Dimensionless Numbers

Nu	Nusselt number
Nu_s	Stagnation Nusselt number
Pr	Prandtl number
Re	Reynolds number
Tu	Turbulence intensity

Elements/ Substances

Al	Aluminum
Cu	Copper
^{2}H	Deuterium
^{3}H	Tritium
^{4}H	Helium-4 isotope
He	Helium
^{7}Li	Lithium-7
LiOH	Lithium hydroxide
Mo	Molybdenum
W	Tungsten

Abbreviations

2D	Two Dimensional
ARIES	Advanced Reactor Innovations and Evaluations Study
ARIES-CS	ARIES Compact Stellarator
CFD	Computational Fluid Dynamics
EDM	Electro-Discharge Machining

ELMS	Edge Localized Modes
FZK	Forshungzentrum Karlsruhe (Karlsruhe Research Center)
GT	Georgia Tech (Georgia Institute of Technology)
HCFP	Helium Cooled Flat Plate
HEMJ	Helium-cooled Modular divertor with Jet array
HEMP	Helium-cooled Modular divertor with Pin array
HETS	High Efficiency Thermal Shield
HTC	Heat Transfer Coefficient
ID	Inner Diameter
ITER	International Thermonuclear Experimental Reactor
NPT	National Pipe Thread
MFE	Magnetic Fusion Energy
MFR	Mass Flow Rate
OD	Outer Diameter
ODS	Oxide Dispersion Strengthened
PC	Personal Computer
PFC	Plasma Facing Component
ppi	pores per inch
PTFE	Polytetrafluoroethylene
SCFM	Standard Cubic Feet per Minute
SOFIT	ultra low-pressure drop short flow-path
TC	Thermocouple
TZM	Tungsten, Zirconium, Molybdenum (a Mo alloy)
UNC	Unified National Coarse (threads)
UNF	Unified National Fine (threads)

SUMMARY

Magnetic confinement fusion has the potential to provide a nearly inexhaustible source of energy. Current fusion energy research projects involve conceptual "Tokamak" reactors, inside of which contaminants are "diverted" along magnetic field lines onto collection surfaces called divertor plates. Approximately 15% of the reactor's thermal power is focused on the divertor plates, creating a need for an effective cooling mechanism.

Current extrapolations suggest that divertor plates will need to withstand heat fluxes of more than 10 MW/m^2. The cooling mechanism will need to use a coolant compatible with the blanket system; currently helium, and use a minimal fraction of the reactor's available pumping power; ie: will need to experience minimal pressure drops. A leading cooling concept is the Helium Cooled Flat Plate Divertor (HCFP).

This thesis experimentally examines four variations of the HCFP. The objectives are to:

1. Experimentally determine the thermal performance of the HCFP with a hexagonal pin-fin array in the gap between the impinging jet and the cooled surface over a range of flow rates and incident heat fluxes;
2. Experimentally measure the pressure drop associated with the hexagonal pin-fin array over a range of flow conditions;
3. Determine and compare the thermal performance of and pressure drop associated with the HCFP for two different slot widths, 0.5 mm and 2 mm over a range of flow rates and incident heat fluxes;

4. Compare the performance of the HCFP with a hexagonal pin-fin array with that of the HCFP with a metal-foam insert and the original HCFP;
5. Provide an experimental data set which can be used to validate numerical models of the HCFP design and its variants.
6. Analytically determine the maximum heat flux which the HCFP can be expected to withstand at theoretical operating conditions in the original and pin-fin array configurations

CHAPTER 1: INTRODUCTION

1.1: Motivation and objectives

1.1.1: Magnetic confinement fusion energy

Fusion has the potential to provide a nearly inexhaustible source of energy [22]. Furthermore, fusion is inherently safe and environmentally benign. With a continuously increasing global demand for energy, an increasing awareness of the environmental costs of current power generation methods, and the prospect of exhausting fossil fuel resources within the foreseeable future, a clean, nearly inexhaustible, and safe energy technology such as fusion will be critical in meeting future energy demands.

Fusion is a potentially inexhaustible energy source because of the variety of basic fuels available for nuclear fusion. The International Thermonuclear Experimental Reactor (ITER) [11], currently under construction in Cadarache, France, will be the world's first full-scale experimental fusion reactor and will use deuterium and tritium as its fuel. Deuterium, ^{2}H, a naturally occurring stable isotope of hydrogen, is commonly available in the form of heavy or deuterated water, which is 0.0153% of and readily extractable from seawater [22]. Tritium, ^{3}H, a short-lived radioactive isotope of hydrogen, can be produced, or "bred" via neutron capture by lithium-7 (^{7}Li). The deuterium-tritium reaction has been identified as the most promising of the hydrogen-based fusion reaction [11].

Fusion energy therefore does not consume any fossil fuels and emits negligible amounts of greenhouse gases. The fusion process is inherently safe because any amplification of the reaction will cause the plasma to extinguish itself and, even if an accident were to occur that would release fusion fuel to the environment, the amount of fuel present inside the reactor is low enough to ensure that the release to the environment will be at levels much lower than those allowed by current regulations [11].

Fusion is the process of "fusing" two atomic nuclei to form a single nucleus heavier than either of the original nuclei, but lighter than the sum of the masses of both nuclei. This difference in mass is converted to energy, as given by Einstein's mass-energy equivalence formula: $E = \Delta mc^2$. In the fusion of deuterium and tritium to create an isotope of helium, ^{4}He and a neutron (n),

$$^2H + {}^3H \rightarrow {}^4He + n \tag{1.1}$$

the energy produced from the reaction is Q = 17.6 MeV. One gram of ^{3}H combines with 0.67 g of ^{2}H to produce 1.6×10^5 kW-hr of thermal energy [22]. However, since the nuclei of both deuterium and tritium are positively charged, they naturally repel each other, creating a repulsive electrostatic barrier that must be overcome for this reaction to occur. H-H Fusion occurs naturally in the core of the sun because incredibly high temperatures and gravitational pressures there give the atoms enough kinetic energy to overcome this repulsive electrostatic force. Note, however, that the most common H-H reaction at the core of the sun does not generally involve the isotopes ^{2}H and ^{3}H.

Unfortunately, the gravitational pressures present at the core of the sun cannot be achieved on Earth. Therefore, even higher temperatures are required for fusion to occur on Earth. In the ^{2}H -^{3}H reaction, temperatures of 1.5×10^8 °C are required; an order of

magnitude greater than the temperatures required for the H-H reaction at the Sun's core [11]. At such high temperatures, electrons separate from nuclei forming a macroscopically neutral cloud of ions and unbound electrons, referred to as plasma. The short-range attractive nuclear force dominates in this plasma cloud, making it possible for the ^{2}H and ^{3}H nuclei to fuse.

In a commercial power plant, the fusion reactions must occur at a high enough frequency to produce net power, which requires the fusion power produced to exceed the heating power used to maintain the plasma at thermonuclear temperatures. To increase the rate of reactions, the plasma must be confined at a high density. The leading plasma confinement technology at present is magnetic confinement.

The "Tokamak" design shown in Figure 1.1, which is the most common advanced magnetic confinement system, uses a toroidal magnetic field to keep the plasma from contacting the confinement chamber walls, since the charged particles spiral about magnetic field lines. This thesis considers a specific heat removal design concept proposed for a magnetic fusion energy (MFE) power plant based on the Tokamak design.

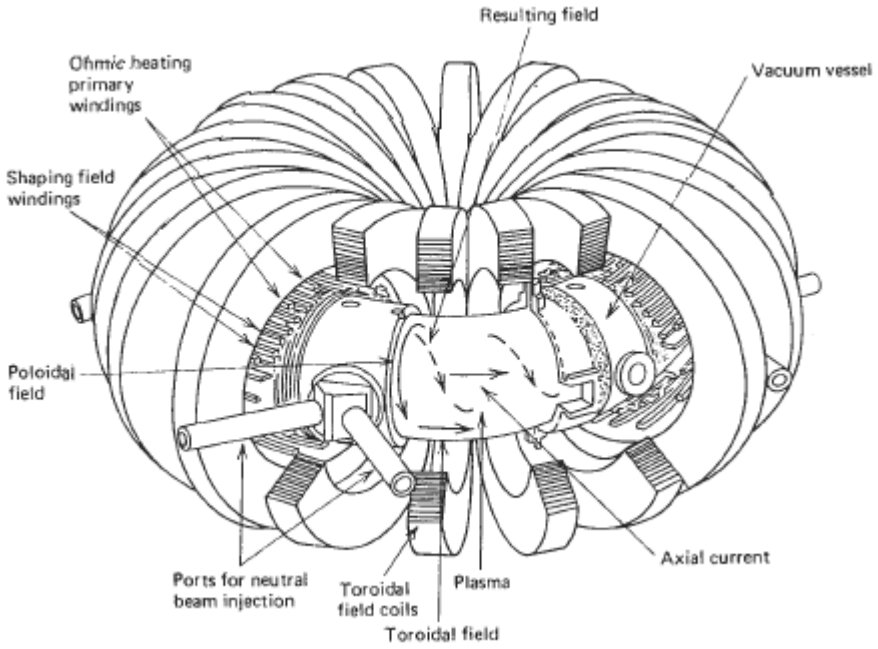

Figure 1.1: Schematic of tokamak fusion reactor

1.1.2: Proposed divertors

The alpha particles (helium nuclei) produced by the ^{2}H -^{3}H fusion reaction will contaminate and cool the plasma over time if the particles are not removed from the plasma. Additionally, the fusion reaction and its products can damage the walls of the reactor, creating debris consisting of particles eroded from the reactor walls. These debris particles can also contaminate and further cool the plasma. Both types of impurities can be removed from the confined plasma along diverted electromagnetic field lines and deposited on a collection surface, called the divertor.

Plasma impurities are therefore focused directly on the divertor target. Current plasma physics extrapolations suggest that future divertors must be capable of handling at least 10 MW/m^2 of heat load [8]. These high incident heat flux levels correspond to approximately 15% of the total fusion thermal power being removed by the divertor

coolant [6]. Recycling and using this heat in the power-conversion system, instead of discarding it as waste heat, could significantly improve the thermodynamic efficiency of MFE power plants. A high-efficiency divertor design should therefore use a coolant which is compatible with the reactor chamber first wall blanket system and can efficiently deliver heat to the power conversion system.

Pressurized water would seem to be an obvious choice of coolant due to its high thermal conductivity and availability. In an experimental reactor, such as ITER, where thermal efficiency and tritium extraction are not a concern, water can, and will, be used as the coolant. However, water has limitations as a practical coolant in future designs.

Pressurized water fission reactors have operating pressures of ~14 MPa (~2000 psi) and maximum coolant temperatures of ~320 ˚C; such high pressures and low (outlet) temperatures are incompatible with most proposed MFE reactor designs. Moreover, the relatively low temperatures required for water limit the thermal conversion efficiency to at most 36% [22]. Using water as a coolant also poses a major safety hazard because water reacts exothermically with certain tritium-breeding materials, including those containing lithium. In the case of a loss-of-coolant event, this exothermic reaction would result in the direct release of significant amounts of energy, and hydrolysis of tritium-breeding materials contained in the reactor blanket. In the case of the hydrolysis of a lithium-containing material, extremely corrosive lithium hydroxide (LiOH) can be formed which has a melting point of 470 ˚C, well below typical operating temperatures for a MFE reactor. For these reasons, water is not considered to be a suitable coolant for a commercial fusion power plant.

Helium (He), on the other hand, has the advantages that it is the gas coolant for which there exists the greatest engineering experience base, and as a noble gas, it is much less chemically reactive than water. Although the thermal conductivity of He is much less than that of water, He can be used as a coolant at very high temperatures and can therefore be used in power conversion systems with much higher thermodynamic efficiencies than those suitable for water. A number of studies have found helium to be the most suitable coolant for MFE divertors because it is an inert gas, compatible with blanket materials, and able to achieve high plant efficiencies [6]. However, since the thermal conductivity of He is not as high as water, divertor geometry designs using He as a coolant must focus more on heat transfer enhancement than those for water. Given its desirability as a coolant for MFE power plants, a number of He-based divertor cooling schemes have been designed and tested, as summarized in the next section.

1.1.3: Helium-cooled flat plate divertor concept

The specific divertor design that was experimentally studied in this thesis is the He-cooled flat plate divertor (HCFP) concept, which was originally developed at the Karlsruhe Research Center (FZK) in Germany and designed to withstand heat fluxes up to 10 MW/m^2. The major advantage of the HCFP design is that each module can cover an area of about 1000 cm^2, more than two orders of magnitude greater than the area covered by modules of alternative divertor concepts such as the T-tube and the He-cooled multi-jet (HEMJ) finger designs, which cover areas of about 13 cm^2 and 2.5 cm^2, respectively. The resultant reduction in the complexity of the manifold system required to

supply coolant to cool a divertor with a typical area of (10 m^2) is a major engineering advantage in a commercial fusion power plant.

The HCFP design uses two-dimensional (2D), or planar, helium jet impingement to cool a tungsten (W) tile surface. Nine identical 50 cm long cooling units are arranged side-by-side to create a single cooling module with dimensions of 50 cm × 19.2 cm × 6 cm. An isometric view of the assembled section is shown in figure 1.2.

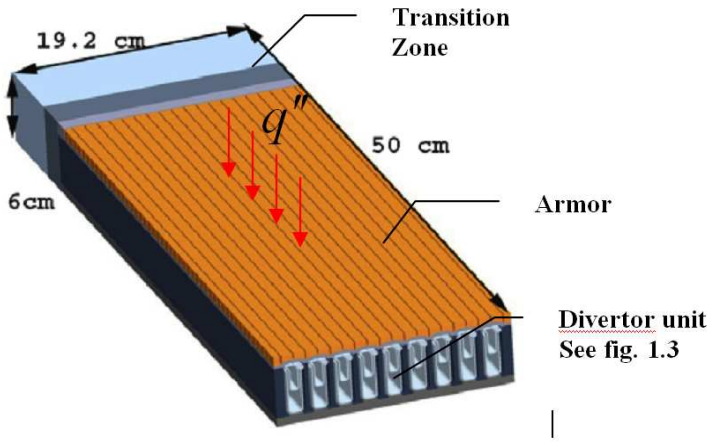

Figure 1.2: Assembled HCFP design: isometric view [25]

The plasma-facing component (PFC) is a castellated and grooved W plate. The side plates which separate the cooling units and the back plate are made with a tungsten alloy, and are brazed together along with the castellated W front plate. The inlet and outlet manifolds are made of oxide dispersion-strengthened (ODS) steel [25]. The inlet manifold is inserted into the W-alloy shell, and aligned with the front plate. The outlet manifold is inserted next with a similar procedure, completing the basic geometry of the divertor unit. Finally, transition zones (shown at the rear of figure 1.2) are joined to the end of each unit.

The frontal cross-section of a single inlet/outlet unit is shown in figure 1.3. The coolant, gaseous He, flows in through the inlet manifold at 10 MPa and 600-700 ˚C and exits the manifold through a 0.5 mm wide slot in the top of the manifold as a 2D jet which impinges on and cools the plasma-facing heated surface [25]. The heated coolant flows down the sides of the inlet manifold and into the outlet manifold where it is removed from the divertor. Thermomechanical analyses of the original FZK design of the HCFP determined that this design had a "cold spot" on the side wall which created significant thermal stresses [25]. In order to increase the temperature at and thereby decrease the thermal stresses on the side wall, a 2 mm gap filled with stagnant He is used to separate each outlet manifold from the W-alloy side walls.

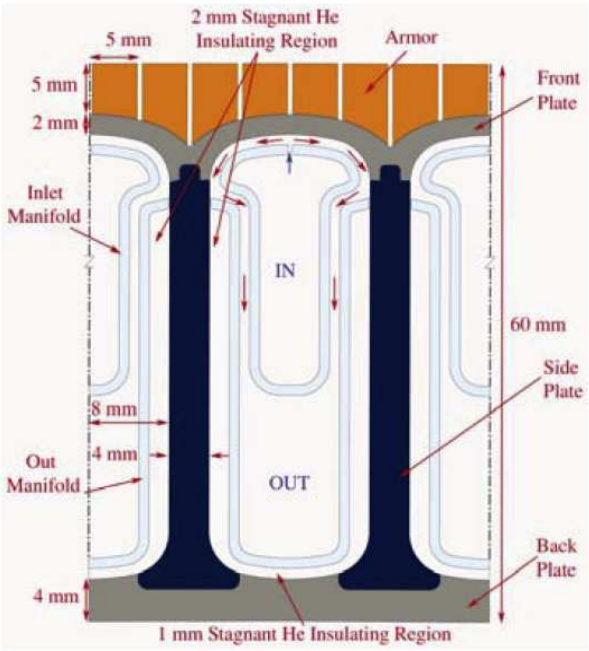

Figure 1.3: Cross-section of HCFP unit [25]

Multiple iterations of thermal-fluid and thermo mechanical analyses have improved the cooling performance, decreased the pumping power, and reduced the thermal stresses of the original HCFP design [25]. The analyses predict heat transfer coefficients (h) as high as 39 kW/(m^2-K) for the most recent HCFP design at a pumping power of less than 10% of the thermal power. Experimental data, collected by E. Gayton at Georgia Tech on several variants of the HCFP design, were also used to validate computational fluid dynamics (CFD) simulations [6].

Gayton's dynamically similar experiments, which used air as the coolant, were performed with a test module similar to that used in this thesis. The objectives of this work were to validate the performance of the HCFP, and evaluate the performance of the design variations described in the next paragraphs.

The performance of the original HCFP design was compared with that for the same design with a molybdenum (Mo) metal foam inserted between the inlet manifold and the heated surface. Numerical simulations by S. Sharafat at UCLA indicated that open-cell metallic foams could greatly enhance heat transfer with a modest increase in pressure drop, and such foams were then used in the advanced ultra low-pressure drop short flow-path (SOFIT) concept [21]. In SOFIT, the foam is sandwiched between the inlet manifold and the cooled surface, as shown in figure 1.4. This creates thermal contact between the foam and the cooled surface, greatly increasing the cooled surface area. The coolant, after impinging on the cooled surface, flows through the porous foam, and out the sides of the manifold just as in the original HCFP geometry.

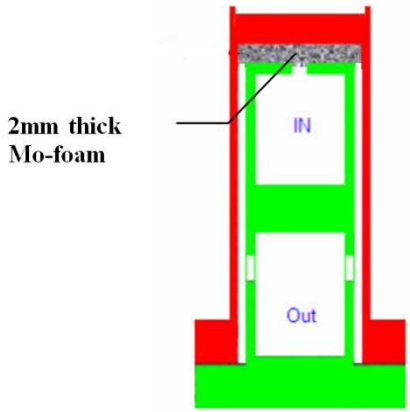

Figure 1.4: Slotted test section with Mo foam insert [6]

Gayton's experiments showed that inserting the Mo foam resulted in a significant increase (as much as 50%) in *h*. Unfortunately they also showed a significant increase (as much as 100%) in pressure drop [6].

An alternative concept for increasing the *h* by increasing the cooled surface area is to insert an array of pins (cylindrical fins) between the inlet manifold and cooled surface so that the impinging air is forced past a pin-fin array as it spreads over the cooled surface. The pin-fins approach has been proposed both for the flat-plate divertor concept as well as in a finger-shaped helium-cooled modular divertor with pin array concept (HEMP) which will be discussed in more detail later. Although manufacturing such a design can be a challenge, the pin-fin array should significantly the increase heat transfer rates with a smaller increase in pressure drop compared with metal foams.

However, no experimental studies have been done to validate predictions of the thermal performance of a pin-fin array. This thesis revisits the concept of using a pin-fin array, and applies it to the flat-plate divertor geometry. The associated increases in heat

transfer are compared with those achieved with metal foam inserts and bare cooled surfaces.

Gayton's experiments used a 2 mm wide slot instead of the 0.5 mm slot specified in the original HCFP design, and also evaluated the performance of an array of circular jets, *vs*. the slot concept. Here, in addition to comparing bare and pin fin-covered geometries, the performance of the 2 mm slot was compared to that of a 0.5 mm slot.

1.1.4: Objectives:

Divertors are at present designed to accommodate heat fluxes of at least 10 MW/m^2, and it is likely that their design values will increase in the near future as more is learned about off-normal events such as edge localized modes (ELMS) [19].
A major objective of divertor designs is to maximize the heat transfer rate so that the high incident heat fluxes can be accommodated within the maximum temperatures dictated by material properties (1300º C for load-bearing tungsten alloys). The SOFIT design identified possibilities for increasing *h*, but at the expense of more pumping power. Pin-fin arrays have been suggested as an alternative to metallic foams that give a high *h* with smaller increase in pressure drop. Experimental validation and optimization of this concept is required, however. .

The objectives of this master's thesis are therefore to:

1. Experimentally determine the thermal performance of the HCFP with a hexagonal pin-fin array in the gap between the impinging jet and the cooled surface over a range of flow rates and incident heat fluxes;

2. Experimentally measure the pressure drop associated with the hexagonal pin-fin array over a range of flow conditions;
3. Determine and compare the thermal performance of and pressure drop associated with the HCFP for two different slot widths, 0.5 mm and 2 mm over a range of flow rates and incident heat fluxes;
4. Compare the performance of the HCFP with a hexagonal pin-fin array with that of the HCFP with a metal-foam insert and the original HCFP;
5. Provide an experimental data set which can be used to validate numerical models of the HCFP design and its variants.

In all cases, *h* is estimated from the temperature distributions measured over the cooled surface, and the pressure drop is measured across the test section.

The nomenclature used to describe the four different test module configurations is presented in table 1.1. In all cases, the thermal performance of each configuration is evaluated over a range of flow rates which span the non-dimensional thermal-hydraulic parameters of interest for the prototypical operating conditions.

Table 1.1: Summary of experimental test module configurations

NAME	DESCRIPTION
0.5 mm Bare	0.5 mm planar jet impinging on a bare surface
0.5 mm Pins	0.5 mm planar jet impinging on surface, then flowing through a hexagonal pin array
2 mm Bare	2 mm planar jet impinging on a bare surface
2 mm Pins	2 mm planar jet impinging on surface, then flowing through a hexagonal pin array

1.2: Literature review:

This section reviews some previous divertor cooling concepts which employ the jet-impingement cooling techniques used by the HCFP. The discussion begins with circular-channel divertors that use an impinging planar jet similar to that examined here, as well as the "T-tube" design studied by L. Crosatti at Georgia Tech. Next, divertor designs that use an array of round jets, specifically the HEMP design, will be described, and previous studies of the HCFP design and its variants by E. Gayton are also discussed. The discussion of these divertor designs is followed by a review of previous research on the thermal-hydraulics of 2D jets impinging on a flat plate and the thermal performance of pin-fin arrays.

1.2.1: Circular channel slot-jet impingement designs

Hermsmeyer and Kleefeldt [7] identified five basic gas-cooled divertor concepts, which are the basis for nearly all the gas-cooled divertor designs proposed to date. The HCFP design is based on two of these concepts, the "porous medium concept" and the "slot concept."

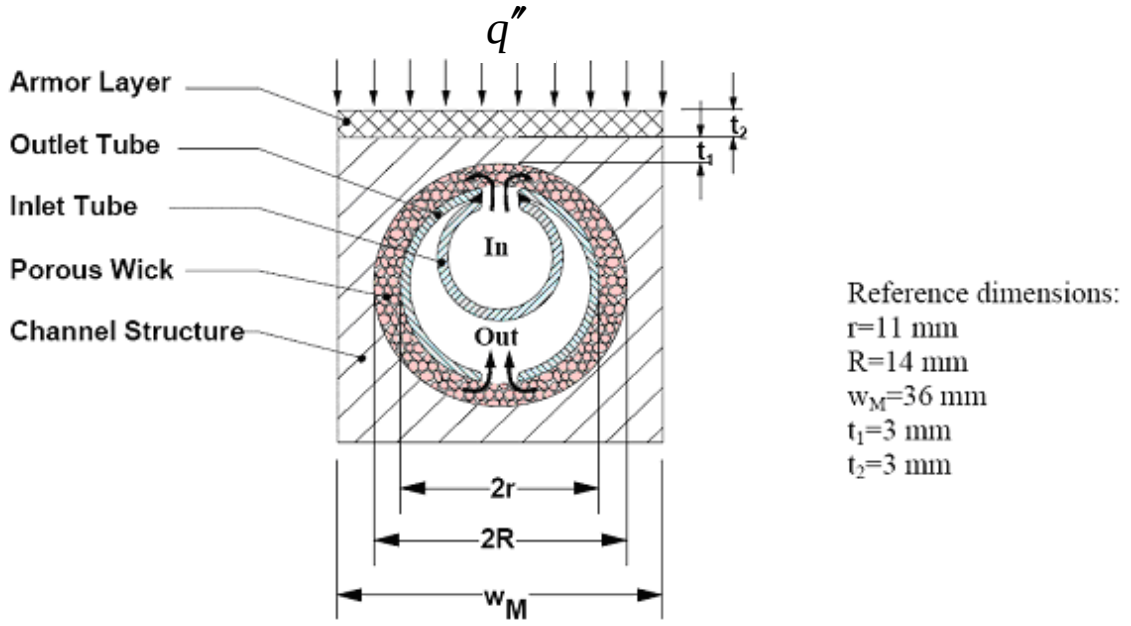

Figure 1.5: Cross-sectional view: Porous medium concept with cross-flow pattern [7]

The porous medium concept combines impinging-jet cooling with a porous metal foam. In the cross-sectional view of this design shown in figure 1.5, two staggered tubes, both with slots, are surrounded by a porous hollow cylinder or "wick" which promotes heat transfer via conduction. The coolant flows in through the smaller inlet tube (labeled In) and is forced via the slot at the top into the wick. It then passes through the porous wick surrounding the outside of the outer tube, and exits through the bottom slot in the outer tube into the sickle-shaped channel between the inner and outer tubes. A longitudinal section of the porous medium concept shown in figure 1.6 illustrates the tapered design of the inner and outer tubes from inlet to exit; this taper is necessary to balance flow velocities in the tube. The cross-section shown in figure 1.5 is taken approximately in the center of this longitudinal section.

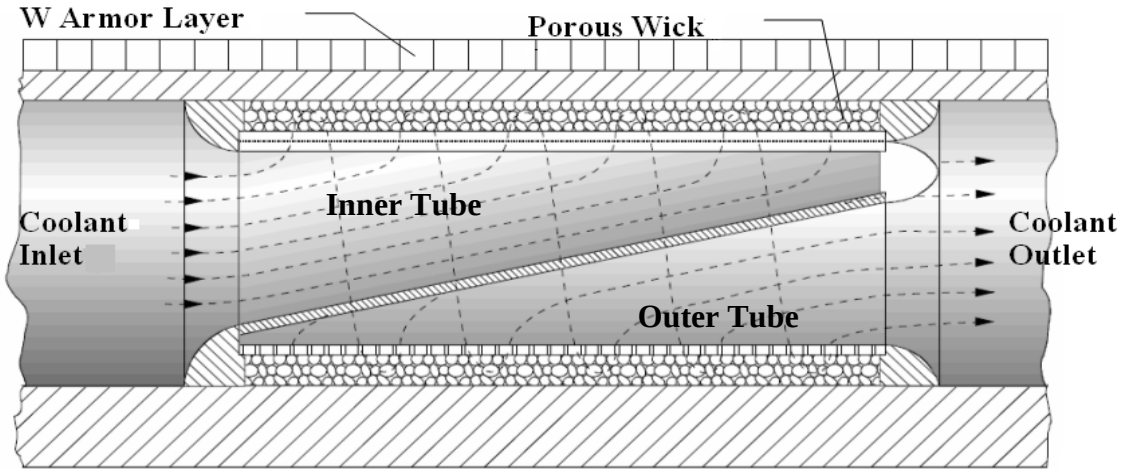

Figure 1.6: Longitudinal section of porous medium concept [7]

The porous wick is of the same material (*i.e.*, W or Mo alloy) as the channel structure and cools the PFC via conduction. The PFC is protected by a 3 mm W armor layer, and q'', the heat flux from the plasma, is directed as shown in figure 1.5. Kleefeldt and Gordeev [12] performed a parametric study of this design to predict its cooling and thermal-hydraulic performance, and used a finite-element analysis to determine its thermal-mechanical properties. They reported that this design could tolerate a maximum heat flux of 5.5-6 MW/m^2 based on the allowable temperature, thermal stress and deformation windows for either W or Mo alloys.

For this design and all the designs discussed hereafter, the operating temperature cannot fall below 600-700 °C because Mo and W alloys undergo a ductile to brittle transition below these temperatures. The major manufacturing issue for the porous media concept involves obtaining a reliable and robust bond between the foam and the heated structure, especially since these two materials are subject to different thermal stresses. Although a pin-fin array machined for example into the channel structure could be used

in lieu of the porous material, such an array would be difficult to manufacture inside a cylindrical cavity. Kleefeldt and Gordeev concluded that the peak heat fluxes associated with the porous wick would most likely be insufficient for a MFE power plant, and that the *h* predicted for the porous foam by their numerical simulations required experimental validation.

To eliminate the bonding issues with the porous medium, a slot concept that was much more easily manufactured was then devised which eliminates the porous medium. Perhaps the best-studied example of this slot concept is the T-Tube divertor design that was proposed for the ARIES compact stellarator (ARIES-CS) study. The T-tube consists of two concentric tubes separated by a 1.25 mm (radial) gap with a flat W armor layer attached to the upper surface of the outer tube facing the plasma. Figure 1.7 shows a cross-section of the T-tube design on the left, with a magnified view of the impinging jet on the right.

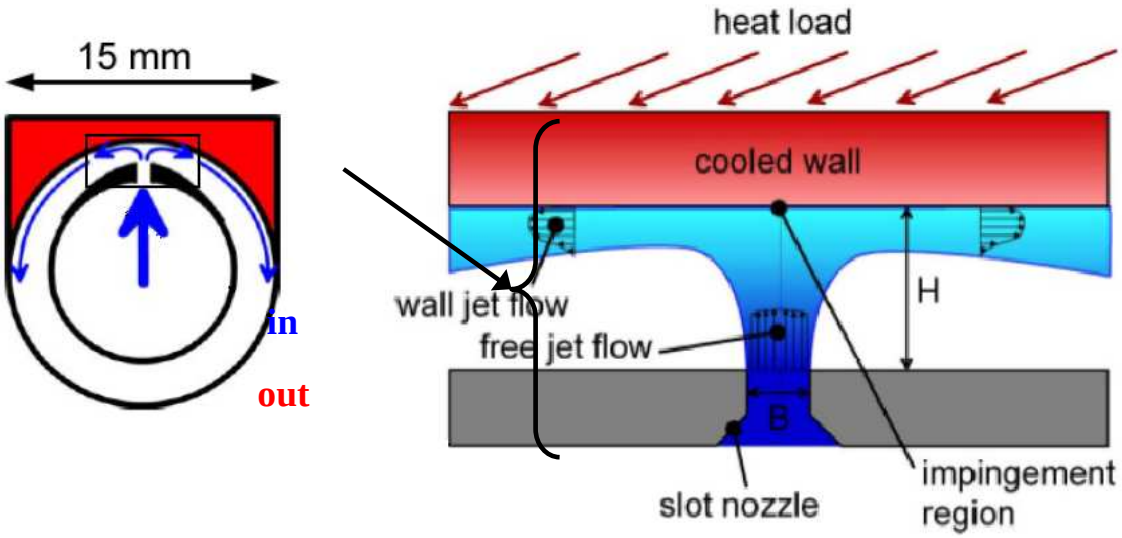

Figure 1.7: T-tube cross-section and impinging jet geometry [9]

As in the HCFP, the primary cooling mechanism for the T-tube is 2D jet impingement cooling. Unlike the porous medium design, the T-tube consists of two concentric and constant-diameter (*i.e.*, untapered) tubes. The coolant, He, enters the T-tube at 10 MPa and 600 ºC through the central inlet port and is accelerated through a 0.5 mm slot in the inner tube (blue region) at a mass flow rate per unit length of 0.4 kg/(s·m) as a planar jet, which then impinges upon the inner surface of the outer tube (*i.e.*, the pressure boundary) bonded to the W-armor layer that faces the actual plasma. The coolant flows along the gap between the two tubes and exits the T-tube at ~9.9 MPa and 680 ºC. The flow of coolant entering the inlet (blue) and outlet (light blue) in the ports at the center of the T-tube can be seen in the longitudinal view shown in Figure 1.8.

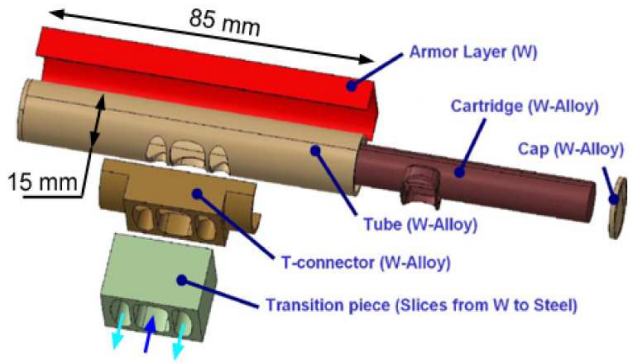

Figure 1.8: Assembly view of a single T-tube module [9]

Recently, the T-tube concept has been experimentally and numerically investigated by L. Crosatti [3] of Georgia Tech, who determined *h* using air as the coolant under conditions matching the helium Reynolds number for the nominal operating conditions proposed for the T-tube. Crosatti's experimental results confirmed the exceptionally high heat transfer coefficients predicted in the preliminary design

simulations for the T-tube, and concluded that this design could indeed accommodate incident heat flux values up to 10 MW/m^2 [3]. Although the T-tube design was shown to meet the design specifications, each module covers a rather small area of about 13 cm^2, tens of thousands of T-tube modules would be required to cool the (100 m^2) areas typical of most divertors.

1.2.2: Multiple jet impingement and pin-array designs:

A number of divertor cooling designs have been proposed that rely on an array of impinging round jets instead of a single 2D planar jet. Perhaps the best-studied of these concepts is the helium-cooled multi jet (HEMJ), which was originally proposed by researchers at FZK and studied experimentally and numerically by J. B. Weathers and L. Crosatti at Georgia Tech [3]. Researchers at FZK also proposed a similar design where a single round jet impinging on a bare surface (the high- efficiency thermal shield, or HETS concept), but this concept has not been experimentally studied [2,15] As shown in the diametric section of the HETS concept in figure 1.9, the coolant exits through a single jet, impinges upon the inside of the cooled surface or cap which is attached to a non-load-bearing tungsten armor that faces the plasma, then flows uniformly along the cooled surface in all directions, exiting in the gap between the “thimble” and its “cap.” .

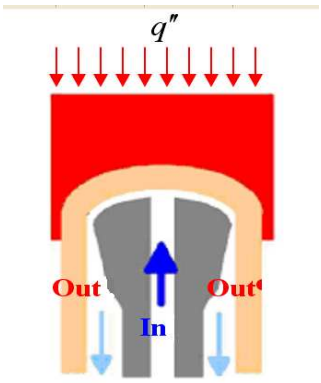

Figure 1.9: Diametric slice of the HETS concept [2]

The HEMP design is, to our knowledge, the only previous divertor design that has considered a pin-fin array. In the HEMP design, an array of Mo-alloy (TZM) fingers, or pin fins, of different sizes is brazed to the inside of a W "cap." The coolant flows through the pin fins radially inwards as shown in figure 1.10 (right), exiting through a single hole in the center of the thimble inside the cap.

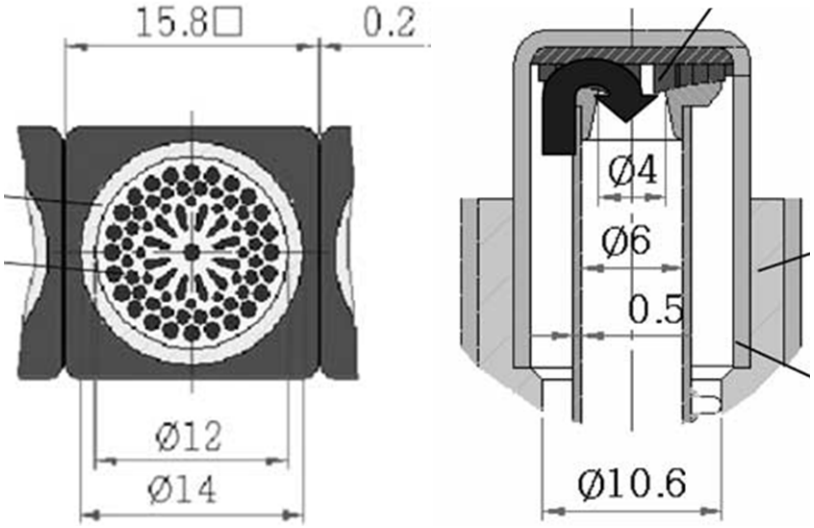

Figure 1.10: HEMP concept pin geometry aerial view (left) and cross-sectional view (right); dimensions in mm [15]

The HEMP concept was designed to accommodate a heat flux of at least 15 MW/m^2 with *h*'s in excess of 60 $kW/(m^2\text{-}K)$ while using less than 10% of the total power for pumping coolant [4]. Diegele and Kruessman [4] analytically determined the difference between outlet and inlet temperatures (ΔT), *h*, the pressure drop across the HEMP; ΔP and the pumping power for the pin-fin design shown in figure 1.10 over a range of inlet pressures This pin-fin geometry was produced by brazing TZM fingers to W tile. Their simulations predicted that this pin-fin arrangement had a maximum *h* of 60 $kW/(m^2\text{-}K)$ and required less than 5% of the total power to pump the coolant.

Diegele and Kruessmann numerically studied the mechanical stresses in the HEMP design, and concluded that mechanical stresses do not exceed allowable design limits under any of the operational conditions studied. They also suggested that the arrangement and geometry of the pin-fin array could be optimized using CFD codes, but to date such an optimization has not been performed, nor have any of their thermal-hydraulic or thermal-mechanical predictions been experimentally validated. Nevertheless, these promising results for pin-fin arrays inspired the configuration studied in this thesis.

1.2.3: Previous HCFP research

E. Gayton studied a number of variations of the HCFP concept for her Master's thesis in Nuclear and Radiological Engineering at Georgia Tech. Simulated HCFP modules cooled using impinging rectangular jets (identical to the 2 mm jet in this study) and a hexagonal array of impinging circular jets (Figure 1.11) were studied. The effects

of inserting a 2 mm thick section of 45 pores per inch (ppi), 65 ppi or 100 ppi open-cell Mo foam in the gap between the jet exit(s) and the cooled surface were also studied.

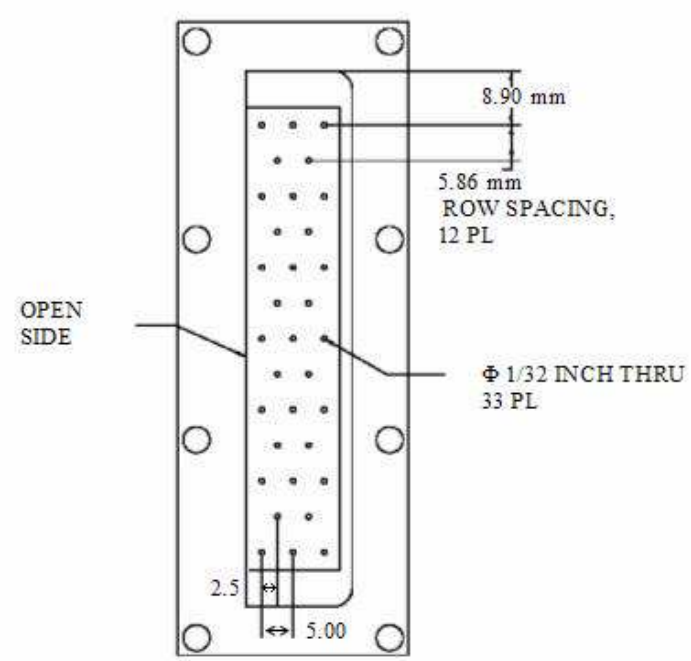

Figure 1.11: Top view of aluminum insert for the hexagonal array of impinging circular jets [6]

The thermal-hydraulic performances of these configurations were evaluated based on their *h* and pressure drop; the best configuration was considered to be one that maximized *h* while minimizing the increase in pressure drop across the test section. Figures 1.12 and 1.13 summarize Gayton's results for the average heat transfer coefficient, h_{avg} and $\Delta P'$; the pressure drop across the test section rescaled to a nominal inlet pressure of 414 kPa, as a function of the coolant mass flow rate $\dot{m}$. In the figures, "Slot-100," "Slot-65," and "Slot-45" denote a 2D jet flowing through 100, 65, and 45 ppi foam, respectively; "Holes-65" describes an array of round jets flowing through 65 ppi foam, "Slot" denotes a 2D impinging jet with no foam, and "Holes" describes an array of round impinging jets with no foam. Overall, the array of round jets gives a higher h_{avg}

than a single 2D jet for otherwise similar operating conditions, and increasing the number of pores per inch in the metallic foam tends to result in a higher h_{avg}. The array of round jets and the addition of metallic foam both result, however, in a higher pressure drop. Comparing the pressure drops for the "Holes-65" case with that for the "Holes" case at a mass flow rate of about 25 g/s, the addition of the 65 ppi foam more than doubles $\Delta P'$ and gives at best a modest increase in h_{avg}. Gayton therefore concluded that the increase in h_{avg} was in most cases not worth the associated increase in pressure drop. Given the increase in pressure drop associated with the array of circular jets (*vs.* that for a single 2D jet), only impinging planar jets were studied in these experiments.

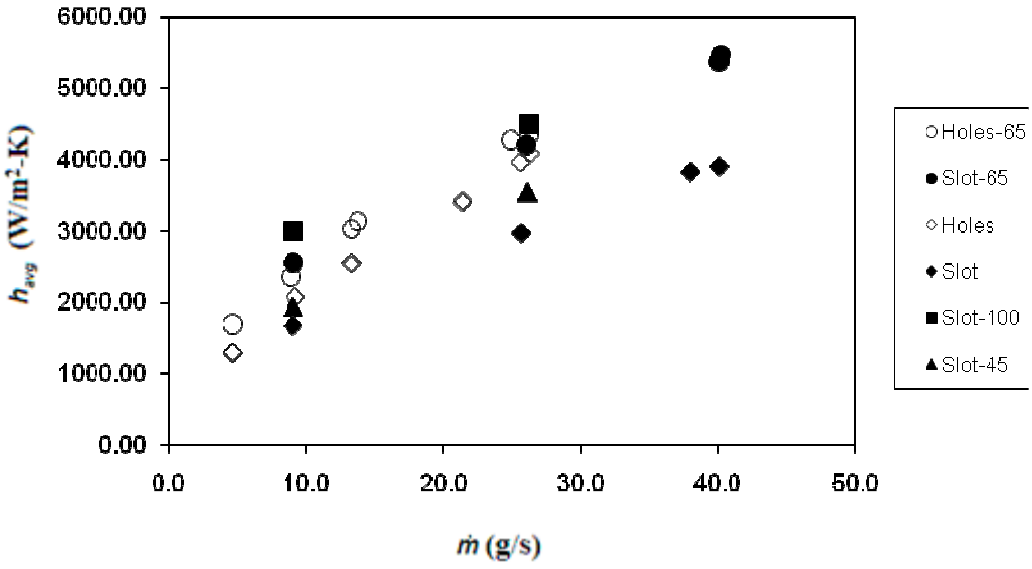

Figure 1.12: Heat transfer coefficient vs. mass flow rate [6]

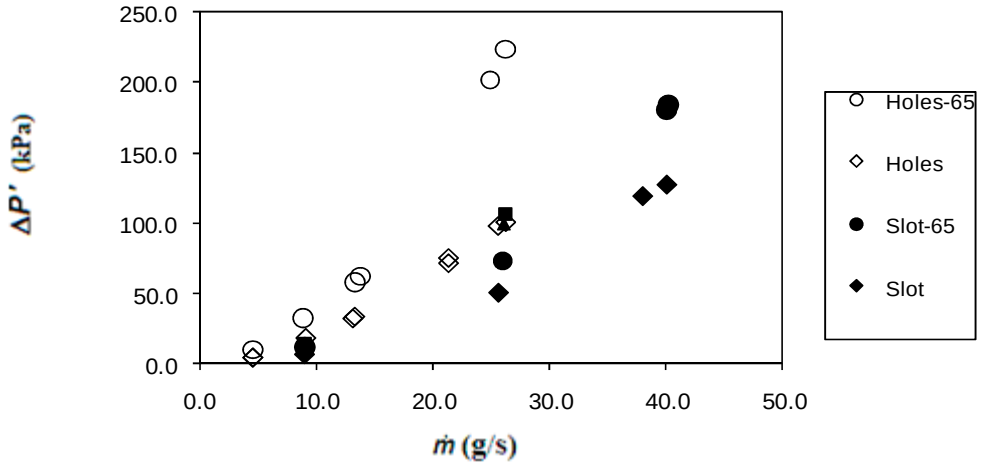

Figure 1.13: Normalized pressure drop vs. mass flow rate [6]

1.2.4: Jet impingement cooling

In the divertor designs examined in this thesis, the primary cooling mechanism is confined turbulent planar jet impingement of cool air impinging on a heated surface. Turbulent jets are preferred over laminar jets because turbulence increases Nu thereby increasing *h*. This section reviews the thermal-hydraulic characteristics of both round and 2D jets impinging and stagnating on a flat plate. Most of the research on these flows has focused on applications involving the cooling of microelectronic components. The thermal management requirements of microelectronics given their exponentially increasing component density and hence ever-increasing power requirements are a major area of research in heat transfer. Most of the literature in this area focuses on the heat transfer characteristics of unconfined impinging jets, however Lin and Chou [14] performed a series of experiments with confined laminar (Re = 190-1537) planar impinging jets.

i. Planar jet impingement *vs*. round jet impingement

According to Lin and Chou [14], impinging round jets have the drawback that their cooling effects are restricted to a relatively small impingement zone on the heated surface. This can be remedied by using an array of multiple jets, but this can lead to flow blockage between neighboring jets and a complicated flow distribution downstream of the impingement zone. On the other hand, a 2D jet issuing from a slot can create a much larger impingement zone than a round jet, although the zone is still restricted along the dimension normal to the slot, and has a much more uniform flow downstream of the impingement zone, simplifying exhausting the hot coolant.

ii. Nozzle to Plate Spacing

Most of the studies in this area have characterized the local *h* at the stagnation point in the center of the impingement zone as a function of the jet Reynolds number (Re) (Zhou & Lee: Re= 2715- 25005), and the ratio between the nozzle width, B and the nozzle-to-plate spacing, Z. Lin and Chou used a slot width of B = 5 mm with Z/B values ranging from 1-8. Zhou and Lee used a slot width of B =11.08 mm and tested Z/B values ranging from 1-30. Figure 1.14 (modified from Ref. [29]) gives a definition sketch of the flow geometry; *X* is the lateral distance along the impingement plate. In this thesis, Z/B = 1 and Z/B = 4 in the test sections studied.

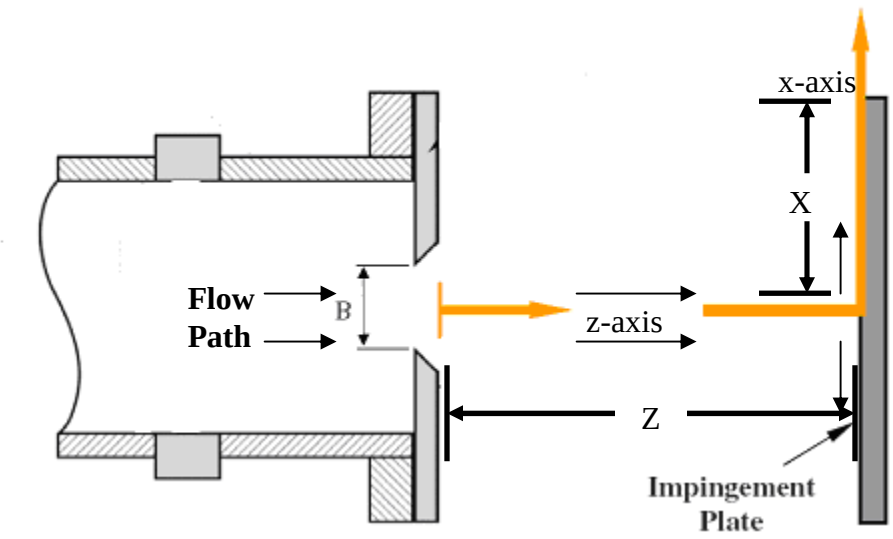

Figure 1.14: Geometry of an impinging planar jet [29] (modified)

The heat transfer coefficient at the stagnation point, h_s depends on the Stagnation Nusselt number Nu_s:

$$h_s = \frac{Nu_s k}{B} \tag{1.2}$$

Nu_s increases primarily with increases in arrival jet centerline velocity, V_{max} and turbulence intensity, Tu on the jet centerline [23,12] where

$$Tu = \frac{v'}{\bar{V}} \tag{1.3}$$

Here, v' is the root mean square of velocity fluctuations, and $\bar{V}$ is the mean velocity. As the cool jet leaves the nozzle exit, it begins to entrain the surrounding hot quiescent fluid due to friction. At low Z this effect is minimal, Tu is low, and h_s is dominated by jet centerline velocity. As Z increases, the potential core width decreases, and will eventually end at a location Z_{cr} on the z-axis. In the potential core ($Z < Z_{cr}$), the jet centerline velocity is equal to the nozzle velocity [14]. Beyond the potential core (Z >

Z_{cr}), the centerline velocity decreases, and would, for a turbulent 2D jet in the self-similar region, decay as $Z^{-0.5}$ [26]:

$$V_{\max} = \frac{Z^{0.5}}{K\rho B} \qquad K \approx 0.016 \tag{1.4}$$

The jet centerline velocity would then have the greatest effect on Nu_s at $Z \le Z_{cr}$. The turbulence intensity will also, in general, increase with Re and hence jet centerline velocity, but as Zhou and Lee discovered, as Z increases and the potential core decreases, *Tu* still increases gradually, and dominates the convection heat transfer beyond the potential core ($Z \ge Z_{cr}$)[29] where jet centerline velocity is decreasing. Since Nu_s increases with both *Tu* and jet centerline velocity, h_s is governed by two conflicting factors. Zhou and Lee empirically determined the following relationship between Nu_s and *Tu:*

$$Nu / \mathrm{Re}^{1/2} = 0.014 Tu\, \mathrm{Re}^{1/2} + 0.517 \tag{1.5}$$

The results of Zhou and Lee [29] for Nu_s as a function of Z/B at Re = 3100, 12500, and 18720 are shown in figure 1.17. At the two higher Re values, Nu_s is maximum around Z/B = 6; the jet at the lowest Re may not have been fully turbulent.

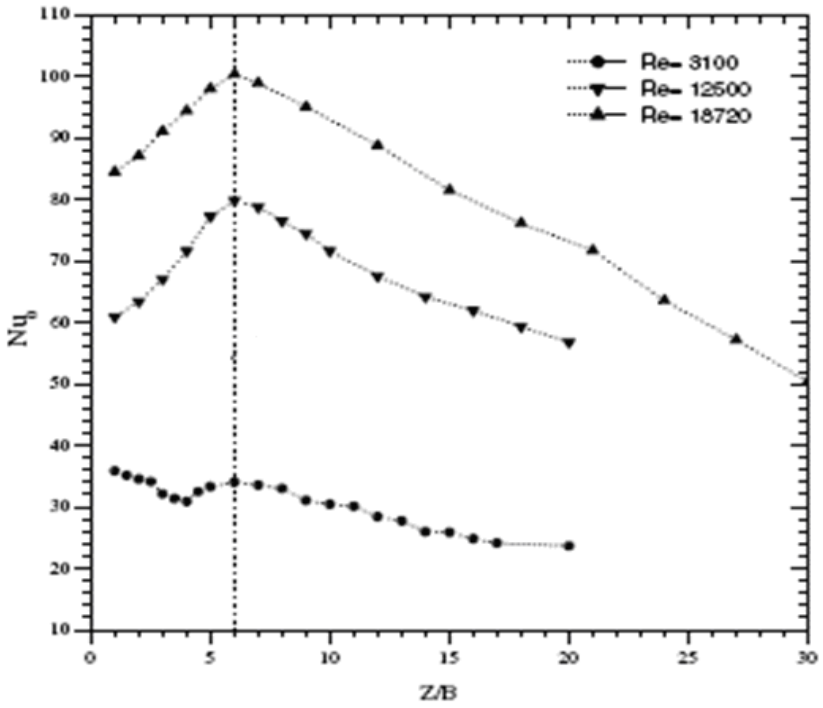

Figure 1.15: Nu vs. Z/B [299]

Downstream of the stagnation point, the impinging jet changes its direction by 90°, and flows along the impinged surface (the x-axis). Local *h* changes with Z/B, but is also a function of X/B. Figure 1.16 shows local *h* as a function of X/B for Z/B = [2:8] as determined by Gardon and Akfirat [5]. This graph shows that the local HTC is maximum at the stagnation point (X/B = 0) and rapidly decreases until about $|X/B| \approx 7$, where a secondary peak occurs for Z/B ≤ 8. Gardon and Akfirat attributed these secondary peaks in the near-field of the flow to the laminar to turbulent boundary-layer transition on the plate surface.

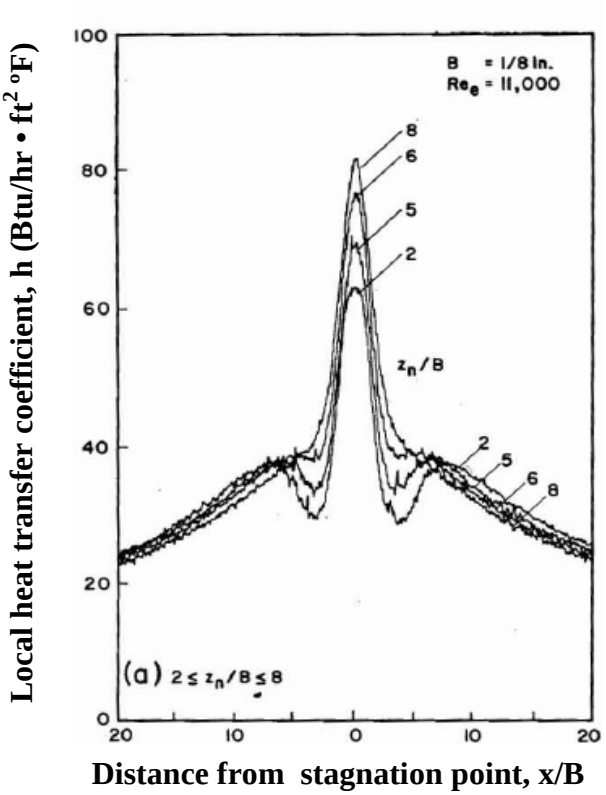

Figure 1.16: Lateral variation of local heat transfer coefficients between a plate and an impinging two-dimensional air jet [5]

As shown in figure 1.17, Zhou and Lee [29] observed similar "secondary peak" behavior, for the local Nusselt number as a function of X/B. Zhou and Lee reported this peak at X/B ≈ 2.3, whereas Gardon and Akfirat recorded it around X/B ≈ 7. Zhou and Lee used a sharp edged nozzle with B = 11.08 mm and the cross section shown in figure 1.14, while Gardon and Akfirat's results are for a nozzle with B = 3.175 mm and the cross section shown in figure 1.18. Finally, Gardon and Akfirat's results are reported for Re = 11,000, whereas Zhou and Lee's results are reported for 12,500. The secondary peaks observed by Zhou and Lee decreased with increasing Z/B, as was the case for the results reported by Gardon and Akfirat.

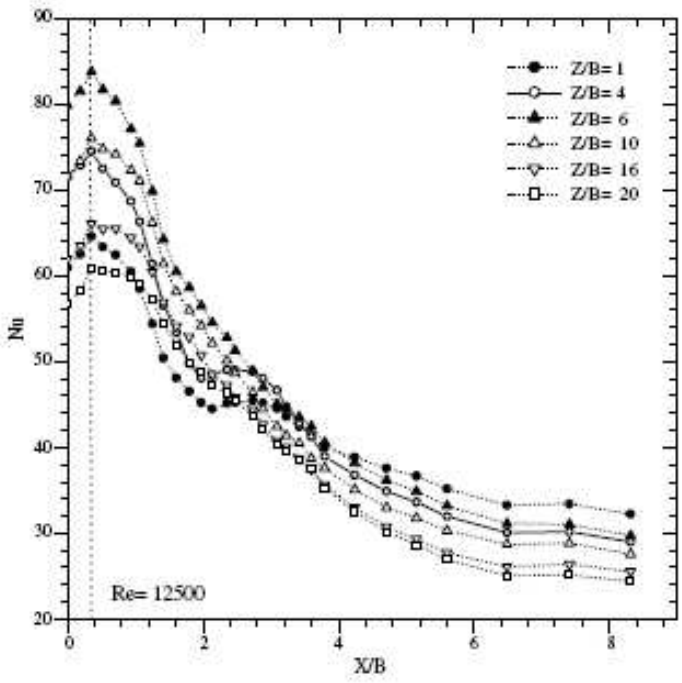

Figure 1.17: Lateral variation of local Nu at a given nozzle-to-plate spacing [29]

Figure 1.18: Cross section of nozzle used by Gardon and Akfirat [5]

Gardon and Akfirat also reported that the maximum *h* occurred at the stagnation point for Re up to 50,000 and that local *h* then rapidly decreases, reaching a roughly constant value around X/Z = 1. The heat transfer coefficient will therefore be the greatest at the center of the jet; i.e., at the stagnation point, and will drop off quickly as it spreads out along the surface. Obviously, *h* also increases with Re. They also mentioned that a larger nozzle (*i.e.*, larger B) produced progressively higher Nu_s, similar to previous results for round or axisymmetric jets [5].

1.2.5: Pin-fin arrays

Pin-fin arrays for cooling have also been studied for the most part for thermal management of microelectronic components. Several studies have focused on how varying the geometry and configuration of the pin fins affect their thermal performance. Pin density, shape, configuration (staggered, *vs*. inline), hydraulic diameter, cross-sectional area, length, tip condition, and number of rows all have effects on the performance of a pin fin array.

Yang, et al. studied the performance of pin fins having cylindrical, square, and elliptic cross sections, in order to determine if there is an optimal fin shape. Each of these cross sections was studied at different fin densities and in staggered and inline configurations. Two performance parameters for each configuration were the pressure drop caused by the configuration and *h* obtained with the configuration.

Figure 1.19 (a, b) summarizes the results of these two performance parameters. Figure 1.19(a) shows the performance of all geometries in an inline configuration, and figure 1.19(b) shows the performance of all geometries in a staggered configuration. N is the number of fins in a 45 mm x 45 mm square area, meaning pin density increases with increasing N. Also, all fin geometries have a 2 mm hydraulic diameter.

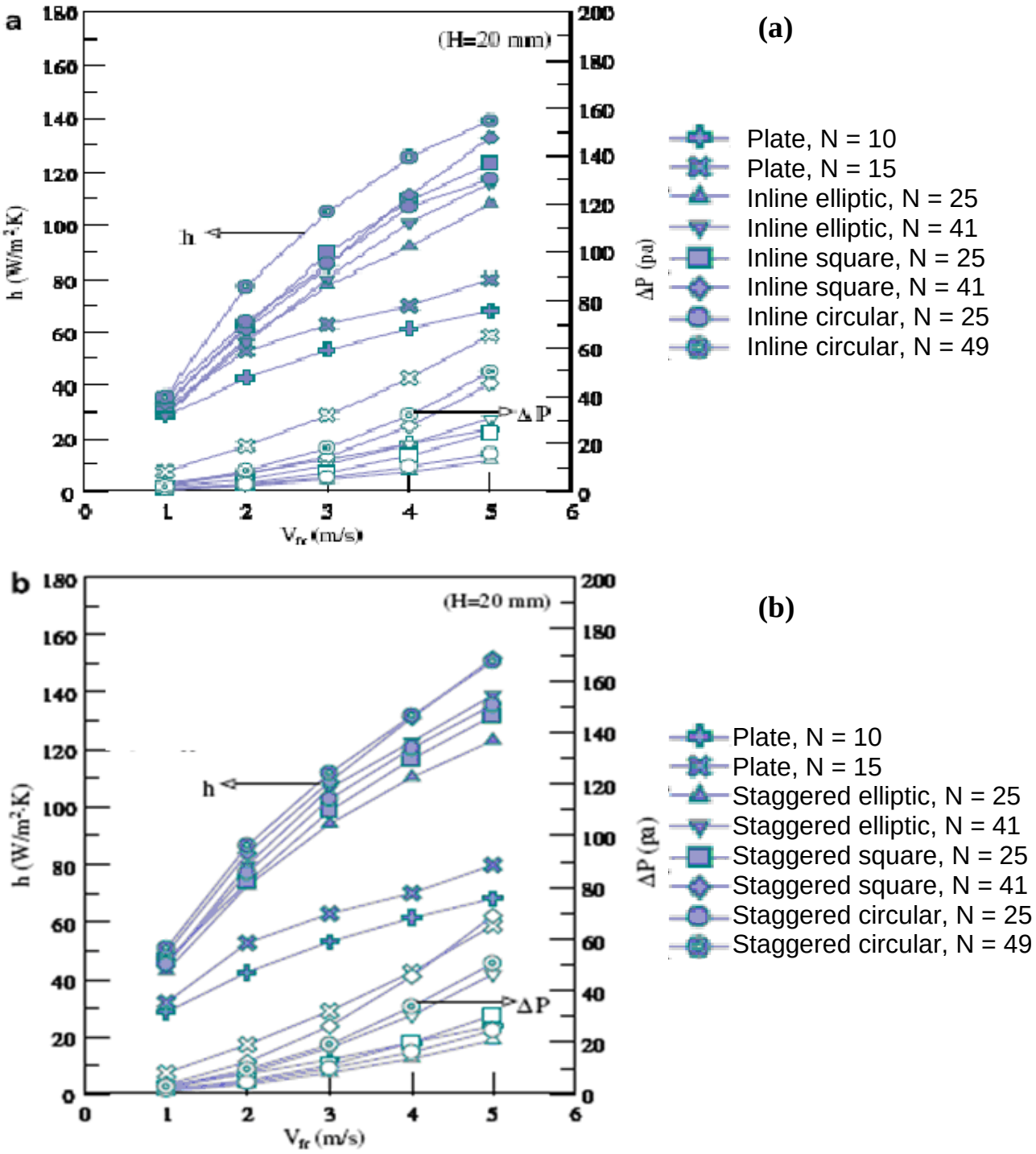

Figure 1.19: Heat transfer coefficient and pressure drop vs. velocity for plate fin and : (a) pin fin with an inline arrangement and (b) pin fin with a staggered arrangement [27]

These results show that circular pin fins generally have the highest *h*, followed by square and elliptic pin fins respectively. Also, higher pin densities increase *h*, and if graphs (a) and (b) are compared very closely, it is apparent that the staggered arrangement tends to create a higher *h* than the inline arrangement. Unfortunately, although a staggered arrangement and higher pin density mean a higher *h*, they also contribute to a higher pressure drop. Of the three geometries studied, square pins create the highest pressure drop, followed by circular, followed by elliptic.

The results of Yang, et al. suggest a difference in flow patterns among the pin geometries. This difference is attributed partially to the Coanda effect. The Coanda effect is the tendency of fluids to follow a curved surface. "For air-flow across the two adjacent tubes, the gap flow may direct to right or left which is known as a deflection flow. The existence of deflection flow may change the general vortex structure behind tubes, causing a better mixing and heat transfer performance."[27]

The deflection of flow due to the Coanda effect depends on the pin spacing. More curved geometries will see higher heat transfer performance with higher density. This explains why a rise in fin density creates the greatest rise in *h* for circular pins, a moderate rise in *h* for the elliptic pins, and an almost negligible rise in *h* for the square pins.

Another important parameter of pin fin performance is the cross-sectional area of the fin. Cross sectional area not only affects the conduction between base and pin, it also has an effect on the surface area of the array, and it can change the hydraulic diameter, which will affect flow patterns.

A very useful performance parameter for the pin fin heat sink concept is the thermal resistance, (R), between the base and the cooling fluid. Peles and Kosar were able to describe R as a function of circular pin diameter under a given pressure drop. They discovered that R decreases rapidly for increasing diameter D, at small D. However, the D:R curve gradually reaches a minimum, and after this point, increasing D will result in higher R. This is a result of two competing factors that affect R as D is varied. On one hand, *h* drops as D increases for a given Re. However, smaller D's result in lower Re for a given mass flow rate. Therefore, for a fixed pressure drop, flow rates are reduced which reduces *h*. This means that R is determined mostly by flow resistance at small (~50 micrometers) D, and by reduction in *h* at large D.

Peles and Kosar also showed that the thermal resistance depends on the geometric configuration, Re, and Pr, not the heat flux. Therefore, R obtained under a certain heat flux can be used without any modification to find the surface temperature for a different heat flux, assuming the geometry, Re, and Pr are not changed.

Incropera and DeWitt also discuss the performance of pin fins in a variety of configurations. They discuss tip conditions, effects of pin shape, and fin length as parameters which effect pin performance. Detailed discussion of these parameters is more in depth than is needed for the purpose of this paper. Therefore, the specific formulas and correlations used from the Incropera and DeWitt text will be discussed when evaluating the performance of the pins geometry.

CHAPTER 2: EXPERIMENTAL APPARATUS AND PROCEDURES

This chapter describes the experimental test section used to simulate the helium-cooled flat plate (HCFP) divertor. It then details the experimental flow loop and the procedures used to conduct the experiments.

2.1: Experimental test section

The experimental test section consists of an aluminum (Al) inner cartridge, a brass outer shell, and a copper (Cu) heater block. The test section is inserted in an air flow loop, and connected to various instruments to allow measurement of the overall pressure drop and local heat transfer coefficient on the cooled surface. The test section was designed and fabricated to closely simulate the actual HCFP design within practical limitations. The various parts of the test section will be detailed in the following sections.

2.1.1: Aluminum inner cartridge

The aluminum inner cartridge of the test section, shown in figure 2.1, simulates the inlet and outlet manifolds of the HCFP divertor module. Although the HCFP design specifies ODS steel for these manifolds, Al was used instead because of its low cost, ease of machining, and availability. The outer dimensions of the cartridge are 40.9 mm (height) $\times$ 19 mm (length) $\times$ 88.2 mm (width). A base flange (outer dimensions 6.48 mm (h) $\times$ 37.0 mm (l) $\times$ 104 mm (w)) was added to the bottom of the cartridge so that the

cartridge can be bolted to the outer shell, increasing the overall height of the inner cartridge to 47.4 mm. The air inlet and outlet ports on the opposite ends of the cartridge both have nominal diameters of 12.7 mm (0.5 in) with a UNF thread profile of 20. The ports are connected to brass 9.53 mm (0.375 in) ID inlet and outlet tubes that pass through the brass outer shell and connect to the exterior flow loop.

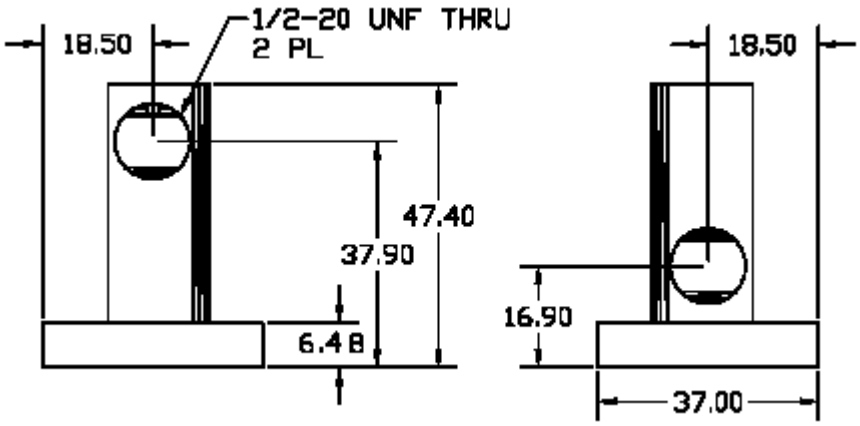

Figure 2.1: Inlet-side view (left) and outlet-side view (right) of inner cartridge; dimensions in mm

Figure 2.2 shows the interior of the inner cartridge. The inlet and outlet manifolds (top and bottom, respectively) are two rectangular channels with dimensions of 76.2 mm (l) × 19 mm (w) × 15 mm (h) separated by an interior rib. As shown in the left sketch, the inner cartridge was machined as a single piece except for one of the side walls. The remaining side wall was modeled by a cover plate fastened to the rest of the cartridge with three machine screws through the middle rib; the sketch on the right depicts the fully assembled inner cartridge.

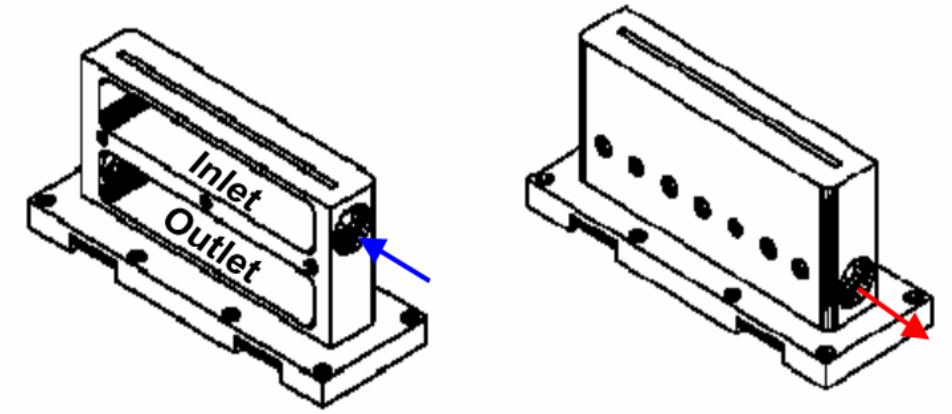

Figure 2.2: Views of the interior of the inner cartridge without the cover plate (left) and the exterior of the slotted inner cartridge after assembly (right)

Two different versions of the inner cartridge, one with a 2 mm wide slot, and one with a 0.5 mm wide slot, were tested, as shown in figure 2.3. In both cases, the slots extended over the entire length of the interior of the inlet manifold, or 76.2 mm. In addition to the difference in materials, the inner cartridge differs from the proposed HCFP design in its length. Although each of the nine cooling channels in the HCFP design has a length of 100 cm, the two-dimensional flow in the central portion of the channel should be accurately simulated by a much shorter channel. To minimize costs and space requirements, the test section therefore reproduces only a central portion of a single HCFP channel with a length of 7.62 cm. This length should be sufficient to provide 2D flow over the central portion of the slot.

Figure 2.3: Photograph of inner cartridges with 2 mm (left) and 0.5 mm (right) wide slots; inlet port is visible for both cartridges

2.1.2: Brass outer shell

The outer shell of the test section, shown in figure 2.4 is machined from C3600 free-machining brass. The thermal conductivity of this alloy, 115 W/(m-K) (at 20^{o}C, www.MatWeb.com), is similar to that of the W alloy at prototypical conditions which has a thermal conductivity of 95-107 W/(m-K) at temperatures of 500-1300 ^{o}C. This brass alloy was used instead of the W alloy because of cost and its ease of machinability. The geometry of the outer shell closely duplicates the W flat plate (which is also the pressure boundary) and the attached W alloy armor within machining limitations, except for the reduction in the length of the channel. The outer dimensions of the shell are 104 mm (l) $\times$ 37.0 mm (w) $\times$ 47.4 mm (h), and the thickness of the shell wall is 5 mm on the top and 2 mm on the sides. A 1 mm raised edge along the exterior sides at the top of the shell helps to center the Cu heater block, which contacts the exterior of and heats the top of the brass shell. When the test section is assembled, the flange on the lower periphery of the outer shell is bolted to the base flange of the Al inner cartridge with eight 6-32 UNC screws

(four on each side); five of the through-holes for these screws are visible on the sketch on the left in figure 2.4

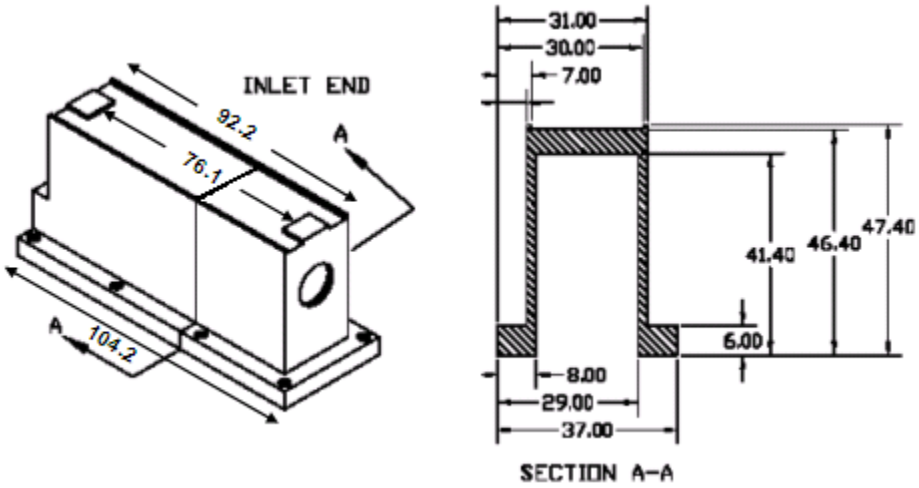

Figure 2.4: Schematic (left) and cross-sectional view (right) of outer shell

Two versions of this outer shell were fabricated: one with a bare inner surface at the top (with 5 mm of brass between the surface where the jet impinges and the surface contacting the Cu heater block); and an otherwise identical shell whose inner surface is covered by a hexagonal array of 808 circular brass pins 1 mm in diameter, 2 mm in height with a pitch of 1.2 mm. As shown in figure 2.5, the array of pin fins populate the entire inner surface of the shell except for a 2 mm wide "strip" in the center of the shell that allows the jet to impinge on the inner surface. The array of pin-fins was formed in the brass by burning away the surrounding material by electro-discharge machining (EDM).

Figure 2.5: Interior view of brass shell showing pin-fin array

As shown in figures 2.6 and 2.7, both outer shells are instrumented with five E-type thermocouples (TCs) (OMEGA EMQSS-020G-6) to measure the temperature distribution over the cooled surface. The center of the 0.81 mm (0.032 in) diameter TC beads are all embedded in the brass shell 1 mm below the cooled surface of the brass shell. Following the coordinate system defined in figure 2.6 where the origin of the coordinate system is defined to be at the center of the slot, the TCs are placed along the slot to measure the temperature profile along x and to verify that temperature distribution is independent of y-position, as would be expected for 2D flow. Table 2.1 gives the (x, y) locations of TCs #1-5; in all cases, the z-location of these TCs is -0.5 mm in a right-handed Cartesian coordinates system.

Table 2.1: Cooled surface thermocouple positions and reference numbers [6]

Thermocouple Reference #	***x*** [mm]	***y*** [mm]
1	-4.5	-10
2	0	0
3	-8.5	10
4	8.5	-5
5	4.5	5

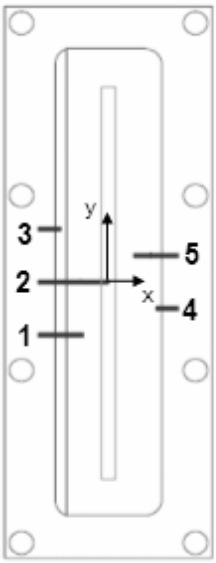

Figure 2.6: TC positions with respect to slot [6]

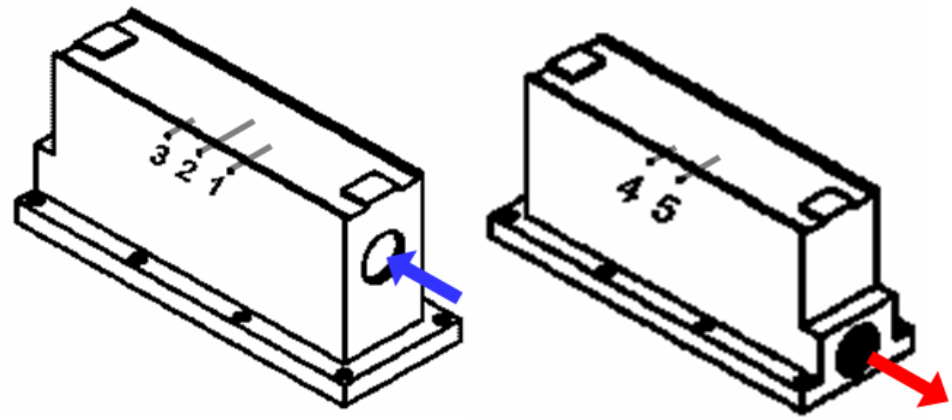

Figure 2.7: Sketch of brass outer shell showing surface TC locations; inlet view (left) and outlet view (right) [28]

When assembling the test section, great care was taken to minimize bending of the TC wires and leads to prevent internal damage which could lead to faulty readings. Each TC was carefully inserted the full distance into its respective borehole, and double-checked to make sure it maintained its position in the borehole while the test section was being insulated.

Figure 2.8 shows the four test configurations studied in this thesis:

1. 2 mm wide jet impinging on a bare surface
2. 2 mm wide jet passing through a hexagonal pin-fin array
3. 0.5 mm wide jet impinging on a bare surface
4. 0.5 mm wide jet passing through a hexagonal pin-fin array.

In this figure, the Al inner cartridge is shown in green, and the brass outer shell (detailed subsequently) is shown in red. In all cases, the gap between the inner cartridge and the flat inner surface of the outer shell is 2 mm (this gap is completely spanned by the 2 mm tall pin fins in configurations 2 and 4).

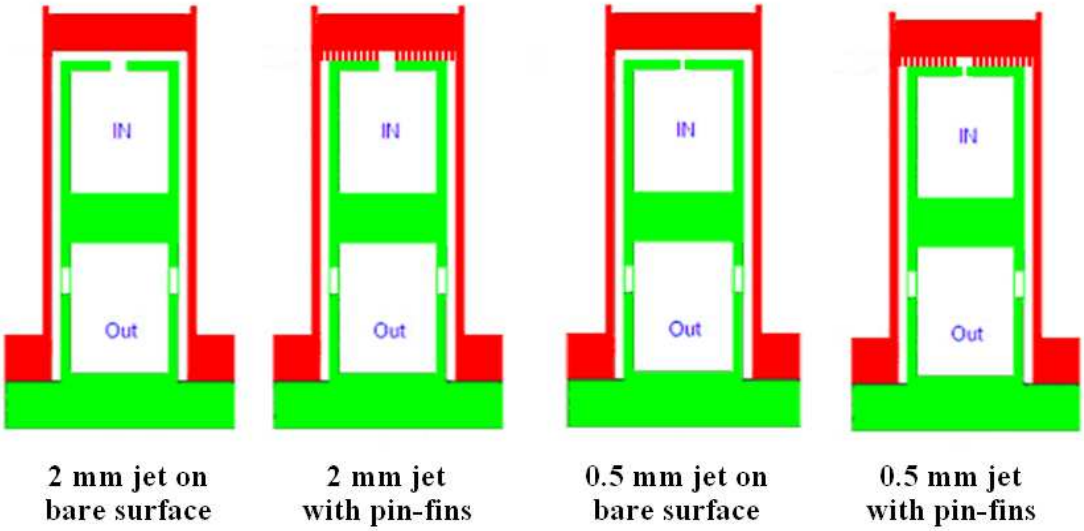

Figure 2.8: Cross-sectional views of test module configurations

During the experiments, the coolant, air at room temperature (~22°C), enters the inlet manifold, accelerates through the slot and impinges as a planar jet on the inner surface of the heated brass outer shell. The resulting stagnation flow efficiently cools the bare surface. For the pin-fin configurations, the 2 mm gap in the pins directly over the slot allows the jet to impinge on the surface before being forced through the array of pin

fins. The coolant then flows around the outside of the inner cartridge in the gap between the cartridge and the shell, enters the exit manifold through seven 4.9 mm diameter holes on each of the two sides of the test section (figure 2.2, right, figure 2.3 both), and finally exits the test section via the exit port.

2.1.3: Copper heater block

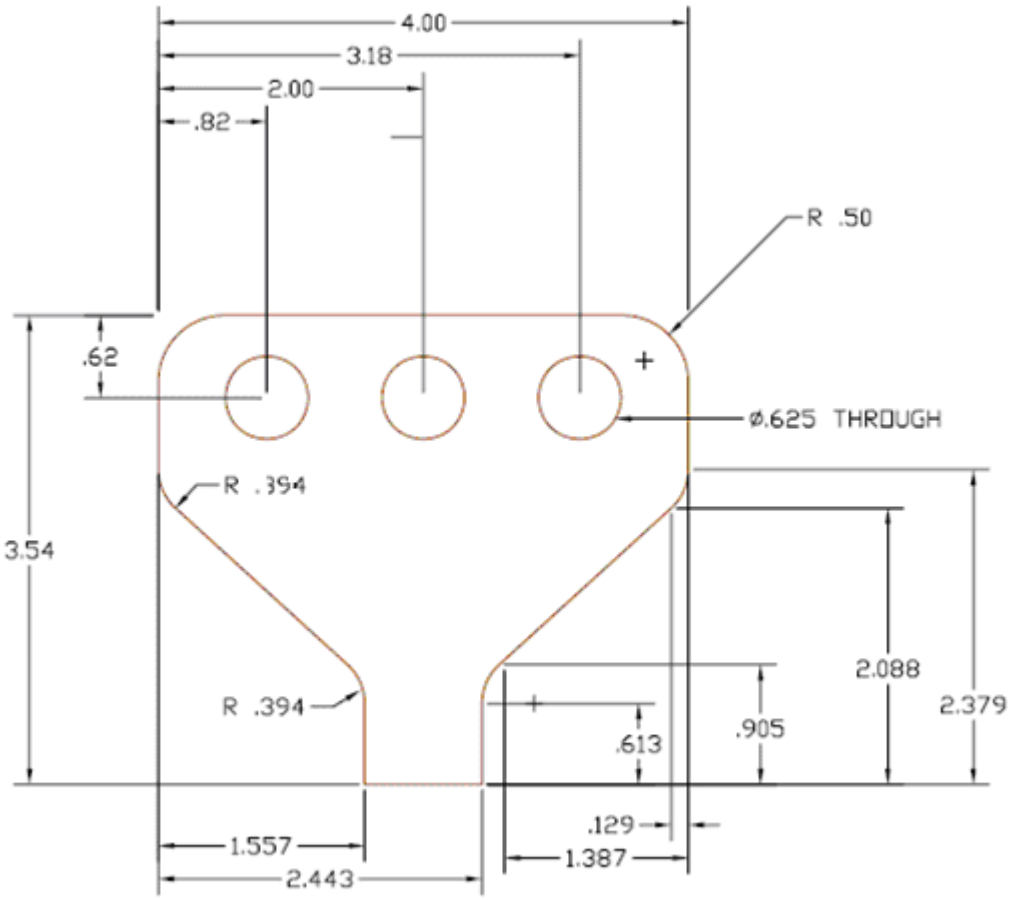

Figure 2.9: Copper heater block dimensions

The C14500 Cu-alloy heater block, or concentrator, shown in figure 2.9, is heated by three "FAST-HEAT® CH47474" 120 V, 750 W cartridge heaters. This block produces a uniform and concentrated axial heat flux on the top of the brass outer shell,

simulating the heat flux incident on the divertor plate surface. The block is 102 mm (4 in) wide at the top where the cartridge heaters are inserted, and tapers down to a width of 22 mm (0.865 in) at the neck where it contacts the top of the brass outer cartridge.

Since much of the test section and set-up are similar to the setup used by Gayton, the following description from her thesis [6] is still valid: "*The cartridge heaters are connected in parallel. The input voltage is adjusted by a variable autotransformer (General Electric Volt-Pac). The input power and current are measured by a digital multimeter (Hewlett Packard 34401 A) and an AC ammeter (Shurile Model 8508), respectively. Each cartridge heater has a maximum output of 750 W, yielding a maximum possible heat flux of 1.35 MW/m^2.*

Six E-type TCs (OMEGA® EMQSS-020G-6) are embedded in the "neck" of the concentrator… located on two x-z planes corresponding to 1/3 and 2/3 of the copper block length (y) and extend to the midpoint of the copper neck width (x). The (z) positions correspond to 3.0, 7.0 and 12.0 mm above the contact surface with the brass outer shell [Figure 2.10]. Additionally, two 1.59 mm diameter OMEGA Type-E thermocouples are embedded in the top of the copper heater block to a depth of 0.62 mm (corresponding to the centerline of the heater cartridges) and are located halfway between the middle heater and the side heaters. This provides a monitor of the peak temperature of the copper heater block, which is limited to 500°C (half of the melting temperature for this copper alloy)." Table 2 gives the (*y*, *z*) locations of TCs #6-10 in the copper heater block, and the TC locations are shown in figure 2.10.

Table 2.2: TC positions and reference numbers for the CU heater block

Thermocouple Reference #	*y* [mm]	*z* [mm]
6	25.4	3
7	25.4	7
8	25.4	12
9	50.8	3
10	50.8	7
11	50.8	12

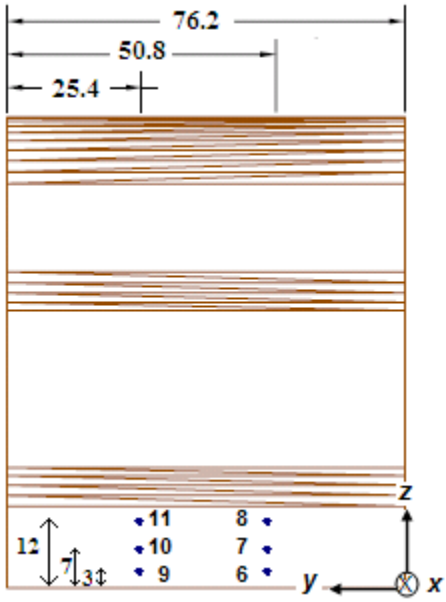

Figure 2.10: Side view of copper heater block with neck TC positions

2.1.4: Assembled HCFP test section

As previously mentioned, the Al inner cartridge is inserted into the brass outer shell. The two are separated by a rubber O-ring, and fastened to each other with eight bolts. Once this portion of the test section is assembled, the thickness of the combined inner and outer flanges is checked in eight separate locations to ensure that the eight bolts have been uniformly tightened, and that the gap between the inner cartridge and the outer shell is consistent over the test section. The Cu input and output ports are then, after

being wrapped at the threads with PTFE thread seal tape and fitted with rubber O-rings, threaded into the Al cartridge just until the O-rings are compressed against the brass outer shell. A 0.13 mm thick graphite sheet is placed between the concentrator heater and the brass shell to ensure good thermal contact. The test section is clamped to the heater with two flat plates located above the heater block and below the test section, and secured with four long 0.25 in UNC threaded rods. Exploded and assembled views of the test section are shown in figure 2.11

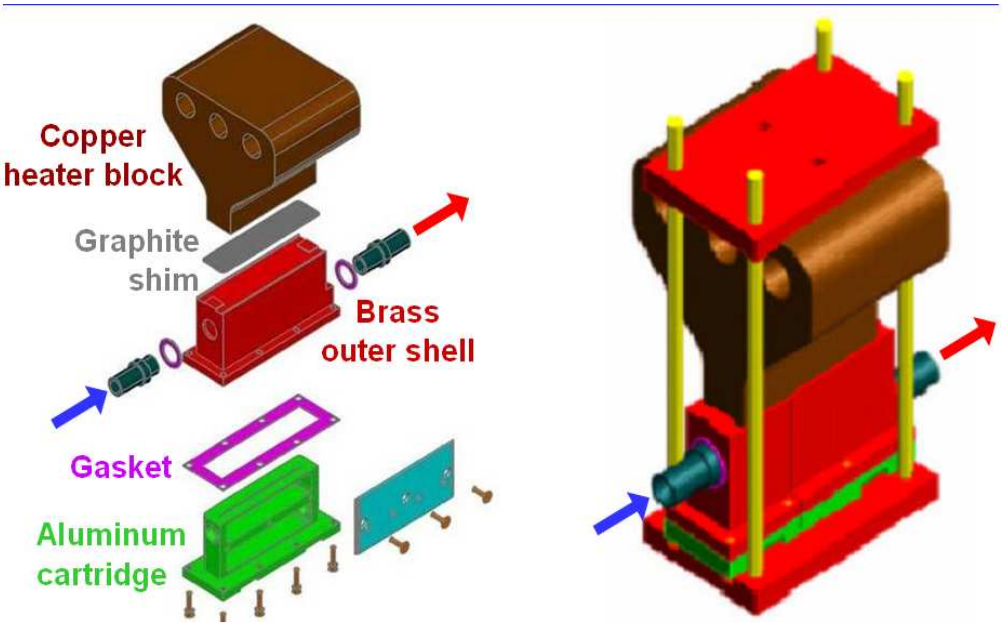

Figure 2.11: Assembled (right) and exploded (left) views of HCFP test section [28]

The test section depicted in figure 2.11 is connected to the air flow loop via the inlet and outlet ports, and the entire loop is pressure-tested to check for leaks. The test section and heater block are then instrumented with TCs #1-5 and #6-11, respectively and insulated with 5 cm thick panels of mineral wool which form a cube around the test section. All the empty space between the insulation panels and the test section is then

filled with loose mineral wool, and the cube is wrapped with wire to secure the insulation during experiments, as shown in figure 2.12.

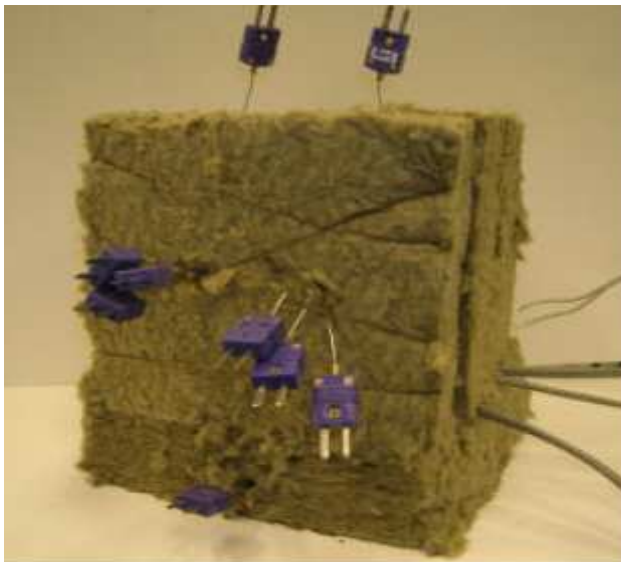

Figure 2.12: Photograph of insulated HCFP divertor test section [6]

2.2: Experimental flow loop

The test section is attached to an air flow loop. Air flows from the building compressed-air line at gauge pressures of 116–524 kPa through a Brooks R12M-25-4 rotameter (calibrated to measure air flows from 0-50 SCFM) that measures the volume flow rate at the test section inlet. The pressure at the test section inlet is measured by an analog pressure gauge (Marsh 100 psi) with a resolution of 6.8 kPa (1 psig) located at the exit of the rotameter. The mass flow rate through the test section is then calculated from these measurements of the volume flow rate and the air density, which is determined from the inlet temperature (measured as described subsequently) and pressure.

A 1.7 m (5.5 ft) section of 12.7 mm (0.5 in) ID reinforced Tygon tubing (Kuriyama K3150 200psi/1.4MPa) connects the rotameter and inlet pressure gauge to a

25.4 mm (1 in) NPT brass cross, which is connected to the brass inlet tube on the opposite side via a 12.7 mm (0.5 in) ID Swagelok fitting. The inlet temperature T_{in} is measured by a Type-E thermocouple (OMEGA® EMQSS-125G-6) which is inserted into the flow through another port on the brass cross; the final port on the cross is connected to the inlet side of a 689.5 kPa (100 psi) differential pressure transducer (OMEGA® PX180-060DV), which monitors the pressure drop across the entire test section.

Similarly, a 25.4 mm (1 in) NPT brass cross is connected to the brass outlet tube via a 12.7 mm (0.5 in) ID Swagelok fitting. This cross houses a Type-E thermocouple (OMEGA® EMQSS-125G-6) that measures the outlet temperature T_{out}, a 0.675 in butterfly valve (Milwaukee Valve Co. BB2) to control the mass flow rate, $\dot{m}$, and a small stainless steel cross. This cross is connected in turn to the outlet side of the differential pressure transducer and a pressure gauge (OMEGA® 100 psi; resolution of 0.5 psi) that measures the outlet pressure P_{out}. The remaining port on the stainless cross is plugged.

The butterfly valve at the outlet controls the mass flow rate through the test section, allowing the system pressure to be elevated in the test section to prevent choking of the flow within the test section. Finally, the ambient pressure, *i.e.*, that of the surroundings, is measured by an absolute pressure transducer (OMEGA PX302-015AV). Figures 2.13 and 2.14 show a schematic of the flow loop and a photograph of the instrumented test section, respectively. The instruments are connected to an Agilent 34970 60-channel data acquisition unit (three 20-channel A/D cards #34901A) connected to a PC with a RS-232 serial cable. The Agilent Bench Link Data Logger 3 software on the PC is used to control and monitor the instrumentation.

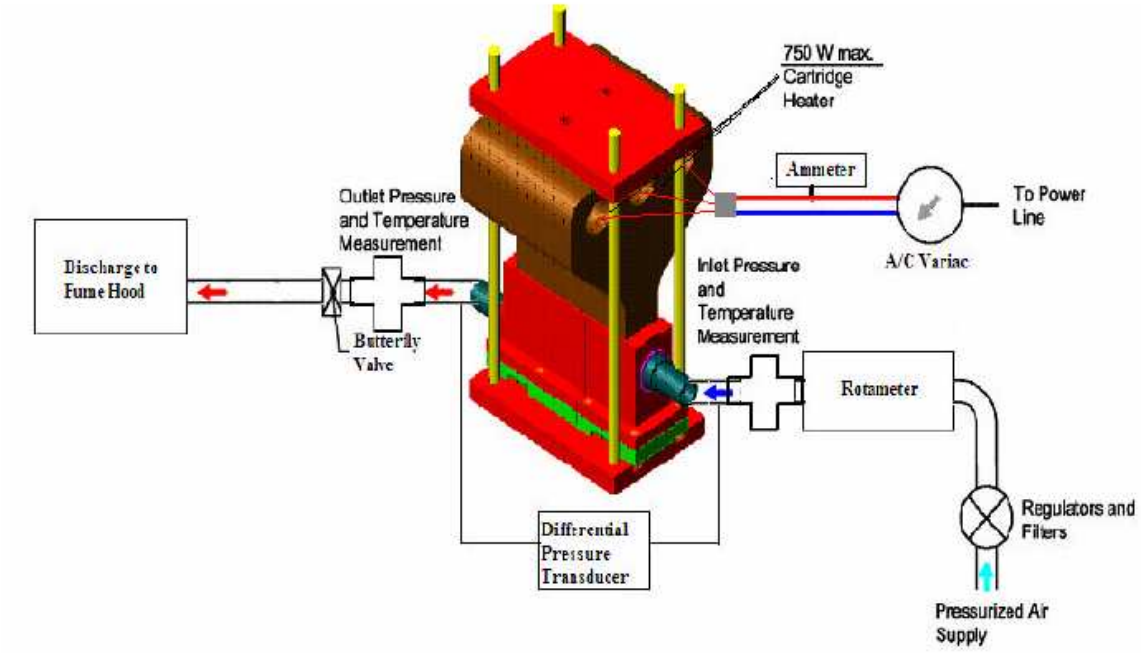

Figure 2.13: Diagram of air flow loop [6]

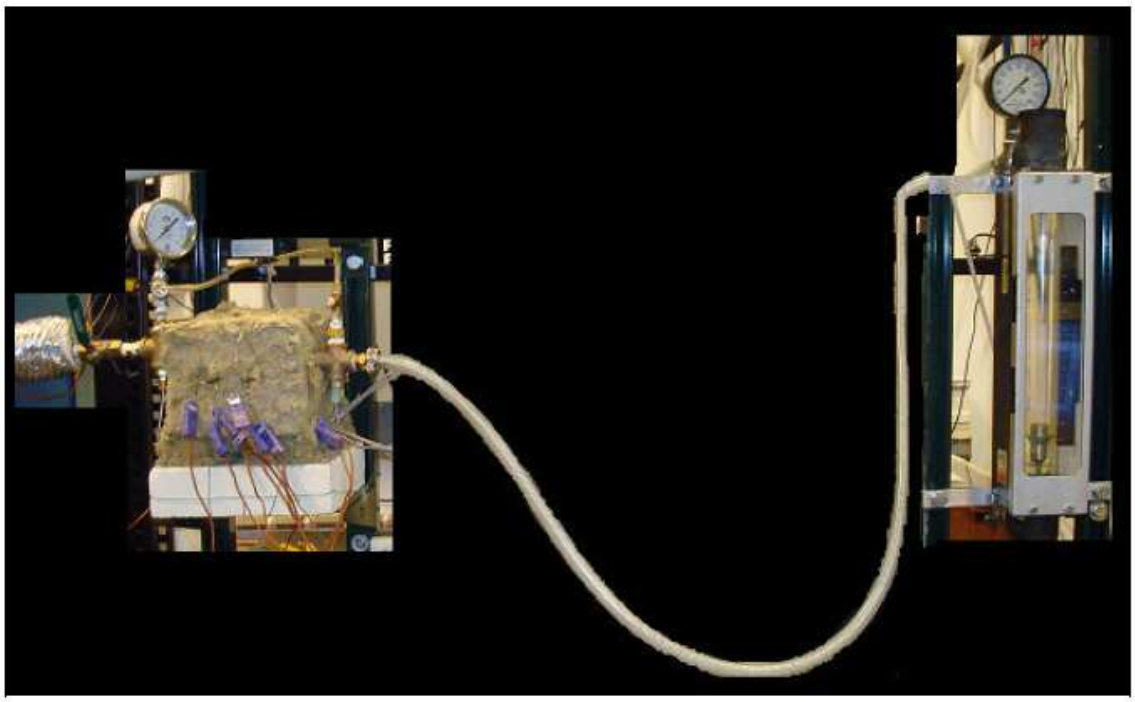

Figure 2.14: Photograph of insulated and instrumented test section [6]

2.3: Experimental parameters and procedures

2.3.1: Experimental operating conditions

The experimental operating conditions (*e.g.* pressures, volumetric flow rates) are characterized by the Reynolds number Re based on the hydraulic diameter of the slot in the inlet manifold, D_h = 2w = 4 mm (where w is the slot width, the average speed of the coolant exiting the slot, $\bar{V} = \dot{m}/(\rho A)$ (where A is the slot area), and the coolant viscosity at the test section inlet μ_{in}:

$$\mathrm{Re} = \frac{\dot{m} D_h}{A \mu_{in}} \tag{2.1}$$

For the same $\dot{m}$ and μ_{in}, Re for both W = 0.5 mm and 2 mm are identical, since both D_h and A are proportional to w.

Experiments were conducted at nominal Re values of 1.2×10^4, 3.0×10^4, and 4.5×10^4. The Reynolds number based on the 0.5 mm slot expected for the baseline HCFP divertor design is 3.3×10^4 [25]. Experiments were performed at experimental heat fluxes q''_{nom} ranging from 0.22 MW/m^2 to 0.72 MW/m^2. Here, q''_{nom} is defined to be the target total power input to the cartridge heaters divided by the area of the concentrator "neck" of 1.67×10^{-3} m^2. The power input was selected such that the peak temperature in the Cu block never exceeded 500 °C, or half the melting point of the C14500 copper alloy. Table 2.3 details the nominal operating conditions of the ARIES HCFP divertor and the GT baseline test module (slot) in an air flow loop. The difference between the Prandtl

numbers Pr of air (0.73) and helium (0.66) should have a minor effect on the measured Nusselt number, and thus the convective *h*, since for turbulent flows $Nu \propto Pr^{0.4}$ [5].

Table 2.3: Comparison of thermal-hydraulic parameters for HCFP and GT experimental study using air [6]

Coolant	T_{in} [°C]	P_{sys} [MPa]	q''_{nom} [MW/m^2]	$\dot{m}$ [g/s-m]	Re [x 10^3]	Pr [-]
He (ARIES)	600	10	10.0	702	33	0.66
Air (GT)	21.6-23.5	0.116-0.524	0.22-0.72	61-527	12-45	0.73

2.3.2: Experimental procedure

Each experiment is performed as follows:

1. The test section is assembled with the appropriate slot width and shell configuration and connected to the heat concentrator and flow loop as previously described.
2. All TCs are inserted, secured, and double-checked to ensure full and accurate insertion.
3. Insulation is added around the test section, with care taken to not disturb the TC. The insulation is secured with wire.
4. The Agilent data acquisition unit, voltage multi-meter, and power supply are switched on. The Bench Link Data Logger 3 software is opened from the PC, the correct acquisition configuration is confirmed, and data scanning is initiated. The Data Logger software records all TC readings, input voltage, test section ΔP, and ambient pressure. Scans are acquired every 30 s.

5. The power supply is adjusted to the desired value by turning the dial on the variable autotransformer while monitoring the voltage and current: the power $Q = IV$, where I and V are the current and voltage. As mentioned previously, the Data Logger measures V, while I is measured by a analog ammeter (15 A full scale) connected to the variable autotransformer.
6. Once the test section temperatures are near the expected steady-state values, the air supply is turned on. The mass flow rate is adjusted to the desired value using the butterfly valve at the test section outlet and the pressure regulator, which controls the pressure of the air supplied to the system. The "uncorrected" volumetric flow rate, SCFM, is read from the rotameter (with a resolution of 0.25 SCFM). The test section inlet pressure is also recorded by reading the pressure gauge at the rotameter exit. These two flow parameters are monitored manually throughout the experiment to ensure that they remain constant over the course of the experiment. The volumetric flow rate is corrected for pressure and multiplied by density to obtain the mass flow rate:

$$\dot{m}\left(\frac{kg}{s}\right) = \dot{m}\left(\frac{ft^3}{\min}\right)\left[\sqrt{\frac{14.7}{P_{rot}}}\rho_{air,rot}\left(\frac{kg}{m^3}\right)\left(\frac{1m^3}{35.3\,ft^3}\right)\left(\frac{1\min}{60\sec}\right)\right] \qquad (2.2)$$

7. The data are continuously recorded in the Data Logger every 30 s until the TC readings for the brass outer shell have reached their steady-state values, which are defined to be values that vary by no more than 1˚C over 30 min. Once steady state has been reached, 60 scans spanning a total of 30 min are taken of TC #1-5; these 60 temperature profiles are then used for data analysis.

Experiments were performed spanning a range of Re and q''_{nom} to determine how the h depends on the operating conditions and to evaluate the robustness of the design. As summarized in table 2.4, data were obtained for the three Re values mentioned earlier of 1.2×10^4, 3.0×10^4, and 4.5×10^4, at q''_{nom} = 0.22, 0.49 and 0.62 MW/m^2, respectively; the range of q''_{nom} at a given Re was limited by the requirements for achieving steady-state conditions. Data were also obtained for Re = 4.5×10^4 at q''_{nom} = 0.65 MW/m^2, and, for the two configurations with pin fins, for Re = 3.0×10^4 at q''_{nom} = 0.62 MW/m^2. The repeatability of each experimental condition was verified by two independent realizations.

Table 2.4: Summary of test conditions

Geometry	Re	q''_{nom}	# of Runs
2 mm, Bare	1.2×10^4	0.22 MW/m^2	2
2 mm, Bare	3.0×10^4	0.49 MW/m^2	2
2 mm, Bare	4.5×10^4	0.60MW/m^2	2
2 mm, Bare	4.5×10^4	0.72MW/m^2	2
0.5 mm, Bare	1.2×10^4	0.22 MW/m^2	2
0.5 mm, Bare	3.0×10^4	0.49 MW/m^2	2
0.5 mm, Bare	4.5×10^4	0.60MW/m^2	2
0.5 mm, Bare	4.5×10^4	0.72MW/m^2	2
2 mm, Brass Pins	1.2×10^4	0.22 MW/m^2	2
2 mm, Brass Pins	3.0×10^4	0.49 MW/m^2	2
2 mm, Brass Pins	3.0×10^4	0.60MW/m^2	2
2 mm, Brass Pins	4.5×10^4	0.60MW/m^2	2
2 mm, Brass Pins	4.5×10^4	0.72MW/m^2	2
0.5 mm, Brass Pins	1.2×10^4	0.22 MW/m^2	2
0.5 mm, Brass Pins	3.0×10^4	0.49 MW/m^2	2
0.5 mm, Brass Pins	3.0×10^4	0.60MW/m^2	2
0.5 mm, Brass Pins	4.5×10^4	0.60MW/m^2	2
0.5 mm, Brass Pins	4.5×10^4	0.72MW/m^2	2

In these studies, q''_{nom} is the target heat flux. The actual experimental heat flux, q''_{actual}, is found by dividing the known power input ($V \times I$) by the top surface area of the brass outer shell (1.589×10^{-3} m^2) ;

$$q''_{actual} = \frac{V \times I}{A_{PFC}} \tag{2.3}$$

Since the inlet pressure varies between experiments, the pressure drops ΔP were rescaled to a common system pressure P_{sys}, which was defined as the average of the inlet and outlet pressures for each experiment. Since the pressure drop is proportional to the dynamic pressure $\rho\bar{V}^2/2$, which itself is proportional to $\dot{m}^2/\rho$, for a given mass flow rate $\dot{m}$:

$$\Delta P \propto 1/\rho \propto 1/P_{sys} \tag{2.4}$$

All measured pressure drops were rescaled to a common system pressure P_{nom} = 414 kPa (60 psia), giving a rescaled pressure drop $\Delta P'$:

$$\Delta P' \equiv \Delta P \, (P_{sys} / P_{nom}) \tag{2.5}$$

These rescaled pressure drops were then compared directly over all the test conditions and configurations studied here.

2.3.3: Experimental test conditions

Nominal experimental test conditions are presented in tables 2.5-2.8, and are identified using 4-digit identifiers. The identifiers for each experiment are given as follows:

- The first digit specifies the slot geometry: "1" specifies the 2 mm slot, while "2" specifies the 0.5 mm slot.
- The second digit specifies the surface geometry: "1" specifies the bare surface, while "2" specifies the surface with the pin-fin array
- The third digit specifies one of the three nominal Reynolds numbers: Re = 1.2×10^4 (1), 3.0×10^4 (2), or 4.5×10^4 (3).

- The fourth digit specifies one of four different nominal heat flux values: q''_{nom} = 0.22 MW/m^2 (1), 0.49 MW/m^2 (2), 0.6 MW/m^2 (3), or 0.72 MW/m^2 (4).
- The letter, A or B, following the dash identifies the two different experiments for this particular set of experimental parameters.

Table 2.5: 0.5 mm slot; bare test cases

Exp. #	$\dot{m}$ [g/s]	Re [-]	q''_{nom} [MW/m^2]	P_{in} [kPa]
2111-A	9.0	12,600	0.22	334
2122-A	21.7	30,500	0.49	199
2133-A	32.5	45,500	0.60	356
2134-A	32.5	45,500	0.72	360
2111-B	9.0	12,600	0.22	417
2122-B	21.3	29,900	0.49	192
2133-B	32.2	45,000	0.60	367
2134-B	32.5	45,500	0.72	367

Table 2.6: 0.5 mm slot; pins test cases

Exp. #	$\dot{m}$ [g/s]	Re [-]	q''_{nom} [MW/m^2]	P_{in} [kPa]
2211-A	8.8	12,400	0.22	334
2222-A	21.9	30,700	0.49	223
2223-A	21.9	30,700	0.60	222
2233-A	33.3	46,700	0.60	369
2234-A	33.3	46,700	0.72	369
2211-B	8.8	12,400	0.22	333
2222-B	21.9	30,700	0.49	219
2223-B	21.9	30,700	0.60	219
2233-B	33.3	46,700	0.60	369
2234-B	33.3	46,700	0.72	369

Table 2.7: 2 mm slot; bare test cases

Exp. #	$\dot{m}$ [g/s]	Re [-]	q''_{nom} [MW/m^2]	P_{in} [kPa]
1111-A	9.0	12,600	0.22	415
1122-A	21.7	30,500	0.49	210
1133-A	31.4	44,000	0.60	359
1134-A	32.2	45,100	0.72	376
1111-B	8.8	12,400	0.22	333
1122-B	21.7	30,500	0.49	207
1133-B	32.5	45,500	0.60	363
1134-B	32.5	45,500	0.72	363

Table 2.8: 2 mm slot; pins test cases

Exp. #	$\dot{m}$ [g/s]	Re [-]	q''_{nom} [MW/m^2]	P_{in} [kPa]
1211-A	9.0	12,600	0.22	416
1222-A	25.7	36,000	0.49	331
1223-A	25.7	36,000	0.60	330
1233-A	32.5	45,500	0.60	371
1234-A	32.5	45,500	0.72	371
1211-B	9.0	12,600	0.22	416
1222-B	25.7	36,000	0.49	331
1223-B	20.6	28,900	0.60	257
1233-B	34.7	48,600	0.60	363
1234-B	34.7	48,600	0.72	362

CHAPTER 3: EXPERIMENTAL RESULTS

This chapter presents and discusses the experimental results for the 18 different test cases examined in this investigation. Several comparisons of test configurations and test section geometry performance are made. First, the performance of the 0.5 mm slot is compared to that of the 2 mm slot while keeping the surface geometry constant. Second, the performance of the pin-covered surface is compared with that of the bare surface for a given slot width. The performance of each geometry is based primarily on two criteria: 1) the "effective" h, h_{eff}, associated with that geometry; and 2) the normalized pressure drop across the test section, $\Delta P'$. These performance characteristics are also compared for varying flowrates and input powers. The objective of these comparisons is to determine the optimum combination of slot width and surface geometry, and to verify that this is the best option over the range of flowrates and input powers studied here. For the pin-covered surface configuration, h_{eff} is the heat transfer coefficient at which the bare surface configuration would have the same cooled surface temperature at the same incident heat flux. For the bare surface, $h_{eff} = h$. For all geometries, a local h_{eff} is calculated for each surface thermocouple location as:

$$h_{eff,local} = \frac{q''_{actual}}{T_{s,local} - T_{in}} \tag{3.1}$$

$T_{s,local}$ is the local surface temperature found by extrapolating the thermocouple temperature reading, T_{TC} to the surface:

$$T_{s,local} = T_{TC} - \frac{lq''}{k_{brass}} \tag{3.2}$$

and k_{brass} is the thermal conductivity of the brass shell at T_{TC}. The distance from the thermocouple bead to the surface, l is 1 mm. The effective heat transfer coefficient for the surface, h_{eff} is the average of the five local heat transfer coefficients.

3.1: The effect of slot width

Two slot widths, namely 0.5 mm and 2 mm, were evaluated experimentally to determine the effect of slot width on performance, and, based on this evaluation, to determine which slot width gave superior performance. For a given pressure and flow rate, the Re based on hydraulic diameter and average velocity is independent of the slot width, and so the effects of slot width were evaluated at a given Re. This section compares the performance of the two slot widths for both the bare and pin-covered geometries. Table 3.1 tabulates the effect of different slot width for a rectangular jet impinging on a bare surface, and table 3.2 compares the effect of different slot width for a rectangular jet impinging on a pin-covered surface.

Table 3.1: Comparison of slot geometries; performance on a bare surface

	$\dot{m}$ [g/s]	**Re** [-]	q''_{actual} [MW/m^2]	$\Delta P'$ [kPa]	h_{eff} [W/m^{2}K]	T_{out} [^{o}C]
1111-A	8.99	12590	0.224	1.4	1547	63.3
1111-B	8.84	12390	0.230	2.1	1523	63.0
2111-A	9.03	12652	0.230	3.6	1415	59.8
2111-B	8.99	12590	0.225	4.3	1661	64.1
1122-A	21.74	30493	0.485	39.7	2593	55.9
1122-B	21.74	30493	0.490	37.5	2623	55.1
2122-A	21.74	30493	0.485	55.1	2635	53.9
2122-B	21.25	29820	0.486	53.4	2441	54.8
1133-A	31.44	44067	0.634	84.5	3299	48.2
1133-B	32.49	45530	0.625	88.9	3361	46.8
2133-A	32.49	45530	0.615	157.2	3635	43.8
2133-B	32.17	45092	0.627	165.0	3585	47.4
1134-A	32.17	45092	0.742	96.9	3416	52.1
1134-B	32.49	45530	0.741	88.2	3407	51.9
2134-A	32.49	45530	0.671	162.6	3313	50.1
2134-B	32.49	45530	0.669	166.0	3307	52.7

In the case of the bare surface impingement, the difference in h_{eff} is negligible between the 2 mm and 0.5 mm slot widths, but there is a large difference in pressure drop. The pressure drop at a slot width of 0.5 mm can be as much as double that for a slot width of 2 mm.

Table 3.2: Comparison of slot geometries; performance on a pin-covered surface

	$\dot{m}$ [g/s]	**Re** [-]	q''_{actual} [MW/m^2]	$\Delta P'$ [kPa]	h_{eff} [W/m^{2}K]	T_{out} [^{o}C]
1211-A	8.99	12590	0.226	2.3	3811	62.3
1211-B	8.99	12590	0.229	3.0	3672	60.4
2211-A	8.84	12390	0.225	7.8	3187	63.2
2211-B	8.84	12390	0.226	6.9	3133	63.9
1222-A	25.73	36063	0.499	60.6	7601	51.8
1222-B	25.73	36063	0.480	60.6	7373	48.3
2222-A	21.89	30708	0.480	71.4	5918	54.4
2222-B	21.89	30708	0.484	69.3	5424	54.2
1223-A	25.73	36063	0.645	59.5	7764	60.5
1223-B	20.58	28860	0.647	40.6	6854	70.1
2223-A	21.89	30708	0.644	72.0	6050	65.4
2223-B	21.89	30708	0.643	68.1	5999	65.7
1233-A	32.49	45537	0.625	149.1	8734	50.4
1233-B	34.67	48594	0.615	145.3	8718	46.4
2233-A	33.34	46723	0.621	162.9	7724	48.0
2233-B	33.34	46723	0.627	162.6	7766	48.9
1234-A	32.49	45537	0.758	149.1	8886	56.7
1234-B	34.67	48594	0.748	145.1	8808	52.3
2234-A	33.34	46723	0.747	162.7	7837	53.7
2234-B	33.34	46723	0.742	162.1	8033	53.2

For the pin-covered surface, the discrepancy between the pressure drops for the 0.5 mm and 2 mm slots are smaller, but the pressure drop for the 0.5 mm slot is still consistently higher than that for the 2 mm slot. This result suggests that a significant part of the pressure drop is due to the presence of the pins. Unlike in the case of the bare surface, h_{eff} is consistently slightly higher for the jet issuing from the 2 mm slot for the pin-covered surface. This may be due in part to the configuration of the pin bank. As mentioned earlier, the pin bank contains a 2 mm wide channel down its center, which allows the air to impinge on the surface before flowing through the pin bank. The width

of this channel matches that of the 2 mm wide slot, but allows some spreading of the jet issuing from the 0.5 mm slot, which may reduce the cooling performance of this case.

3.2: Pins vs. bare surface

The most important modification studied here is the addition of the pin-covered surface. When comparing the performance of the pin-covered surface with a bare surface, the pin-covered surface should give a higher h_{eff} and therefore better cooling, but at the cost of higher pressure drop. The objective of this section is to compare the pin-covered surface with the bare and determine the trade-off between h_{eff} and $\Delta P'$. Tables 3.3 and 3.4 compare results for the bare and pin-covered surfaces for slot widths of 2 mm and 0.5 mm, respectively.

Table 3.3: Bare surface vs. pins; 2 mm slot width

	$\dot{m}$ [g/s]	Re [-]	q''_{actual} [MW/m^2]	$\Delta P'$ [kPa]	h_{eff} [W/m^{2}K]	T_{out} [°C]
Bare Surface						
1111-A	8.99	12590	0.224	1.4	1547	63.3
1111-B	8.84	12390	0.230	2.1	1523	63.0
1122-A	21.74	30493	0.485	39.7	2593	55.9
1122-B	21.74	30493	0.490	37.5	2623	55.1
1133-A	31.44	44067	0.634	84.5	3299	48.2
1133-B	32.49	45530	0.625	88.9	3361	46.8
1134-A	32.17	45092	0.742	96.9	3416	52.1
1134-B	32.49	45530	0.741	88.2	3407	51.9
Pin-Covered Surface						
1211-A	8.99	12590	0.226	2.3	3811	62.3
1211-B	8.99	12590	0.229	3.0	3672	60.4
1222-A	25.73	36063	0.499	60.6	7602	51.8
1222-B	25.73	36063	0.480	60.6	7373	48.3
1233-A	32.49	45537	0.625	149.1	8734	50.4
1233-B	34.67	48594	0.615	145.3	8718	46.4
1234-A	33.34	46723	0.747	162.7	8886	53.7
1234-B	33.34	46723	0.742	162.1	8808	53.2

From Table 3.2.1, it is clear that for the 2 mm slot width, the pin covered surface increases the pressure drop by 40% to 70%. However, the increase in h_{eff} from the bare surface to the pins is as high as 180%, and on average, about 150%, suggesting a significantly better heat transfer performance in the pin covered surface.

Table 3.4: Bare surface vs. pins; 0.5 mm slot width

	$\dot{m}$ [g/s]	Re [-]	q''_{actual} [MW/m^2]	$\Delta P'$ [kPa]	h_{eff} [W/m^{2}K]	T_{out} [^{o}C]
2111-A	9.03	12,652	0.230	3.6	1415	59.8
2111-B	8.99	12,590	0.225	4.3	1661	64.1
2211-A	8.84	12,390	0.225	7.8	3187	63.2
2211-B	8.84	12,390	0.226	6.9	3133	63.9
2122-A	21.74	30493	0.485	55.1	2634	53.9
2122-B	21.25	29820	0.486	53.4	2441	54.8
2222-A	21.89	30708	0.480	71.4	5918	54.4
2222-B	21.89	30708	0.484	69.3	5911	54.2
2133-A	32.49	45,530	0.615	157.2	3634	43.8
2133-B	32.17	45,092	0.627	165.0	3585	47.4
2233-A	33.34	46723	0.621	162.9	7724	48.0
2233-B	33.34	46723	0.627	162.6	7766	48.9
2134-A	32.49	45,530	0.671	162.6	3313	50.1
2134-B	32.49	45,530	0.669	166.0	3307	52.7
2234-A	33.34	46723	0.747	162.7	7837	53.7
2234-B	33.34	46723	0.742	162.1	8033	53.2

For a slot width of 0.5 mm, however, the bare and pin-covered surfaces have similar pressure drops, especially at the higher flow rates. This, combined with the results of section 3.1, suggests that the pressure drop associated with the flow through a 0.5 mm wide slot is significantly greater than the pressure drop associated with the flow through the pin array, especially at higher flow rates. Nevertheless, the pin-covered surfaces give h_{eff} values that are more than 100% greater than that for the corresponding bare surface case.

In all the tables in sections 3.1 and 3.2, the pressure drop results at the lowest flow rate do not follow the same trends as the data at higher flow rates. This is most likely due to the uncertainty in the $\Delta P'$ measurements, which is as high as 200% for $\Delta P' < 2$ psi, as detailed in appendix section A.3.

3.3: Graphical representation of flow rate, heat transfer coefficient, and pressure drop relationships

A graphical representation of the data in tables 3.1-3.4 is provided in Figures 3.1 and 3.2. As shown in Figure 3.1, the two highest rates of $\Delta P'$ with Re are associated with the 0.5 mm slot, while the pins geometry contributes slightly less to pressure drop. In fact, there is almost no difference between the two surface geometries for the 0.5 mm slot. The smallest pressure drop is associated with the 2 mm slot and bare surface geometry. However, as shown in Figure 3.2, the bare surface geometry consistently results in a lower h_{eff}. The pins geometry approximately doubles h_{eff} in all cases. These results match those of tables 3.1-3.4.

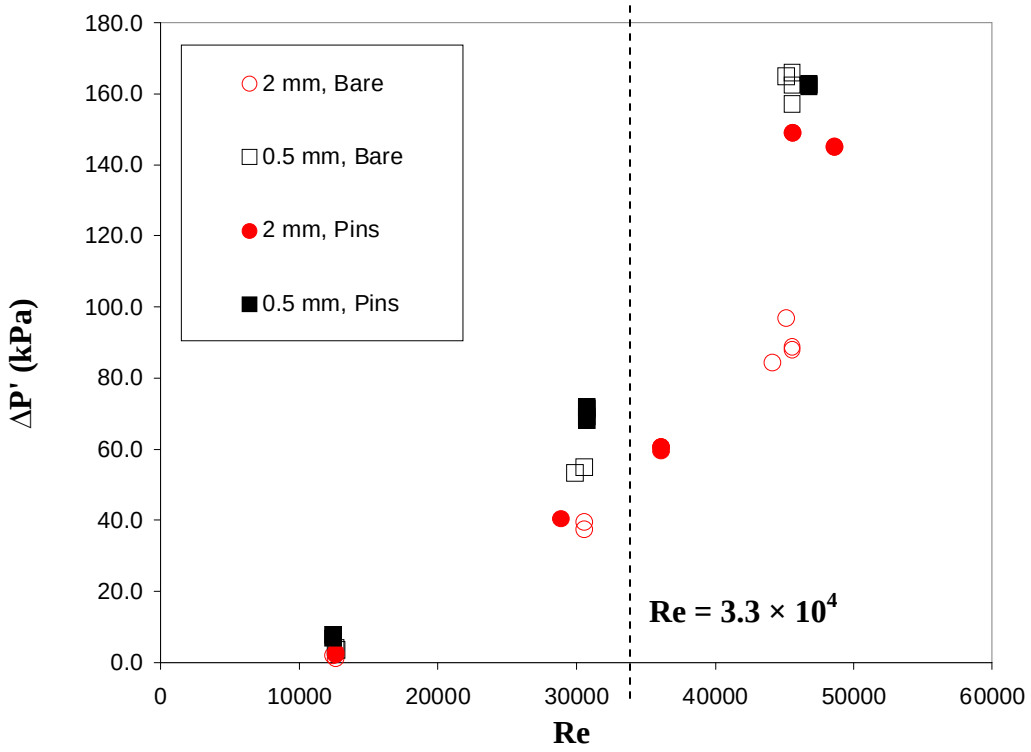

Figure 3.1: Experimental summary: pressure drop vs. mass flow rate

The dashed vertical line in each of the graphs represents the Reynolds number at which the HCFP is expected to operate.

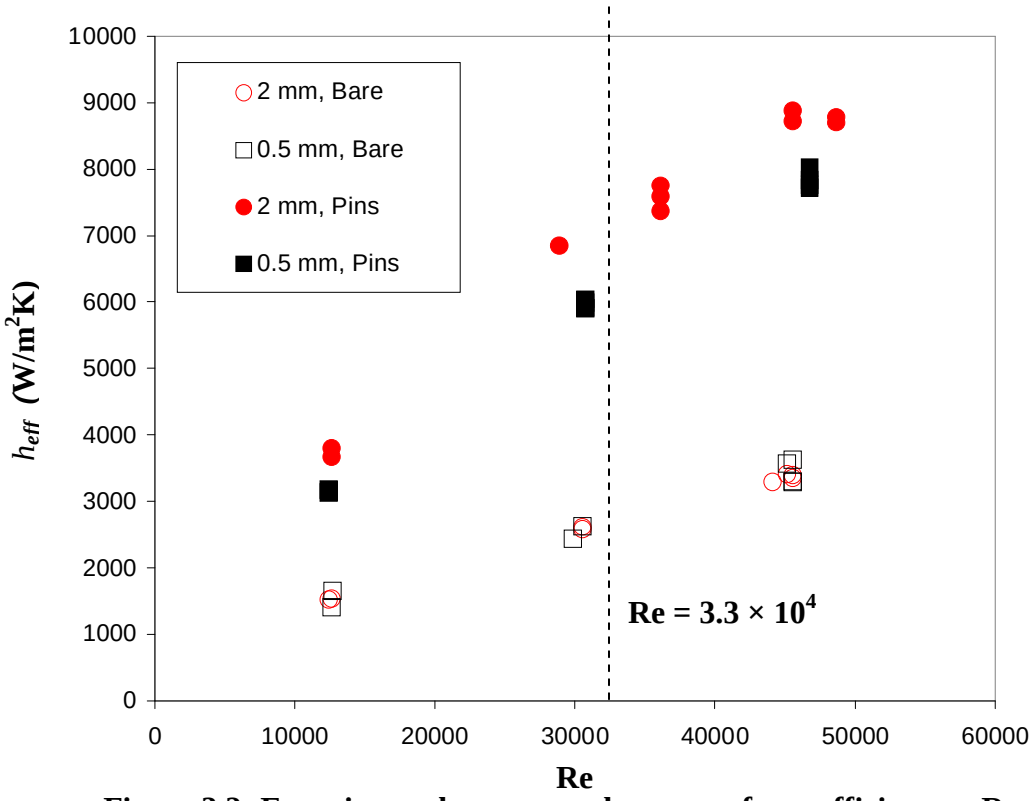

Figure 3.2: Experimental summary: heat transfer coefficient vs. Re

Another important result seen in Figures 3.1 and 3.2 is that both $\Delta P'$ and h_{eff} increase with increasing flow. The effective heat transfer coefficient consistently rises by about 60% with each 100% increase in Re. Although the relationship between Re and $\Delta P'$ is not linear or consistent for all cases, $\Delta P'$ rises much more quickly with Rein all cases than h_{eff} does, suggesting that there will be an increasing tradeoff between h_{eff} and $\Delta P'$ with increasing Re.

3.4: Calculated vs. experimental performance of pin fin array

3.4.1: Calculation of effective heat transfer coefficient

An array of fins will increase the surface area, and should therefore increase h_{eff}. The effective heat transfer coefficient for the pin-covered surface $h_{eff,calc}$ can be predicted using basic heat transfer considerations, as discussed briefly here. This section compares $h_{eff,calc}$ with the experimentally measured effective heat transfer coefficient for the pin-covered surface h_{eff}.

In the simplest model, $h_{eff,calc}$ would simply be the heat transfer coefficient for the bare cooled surface h_{bare} under otherwise identical experimental conditions corrected for the effect of the pins. Although the pins will increase the cooled surface area, not all of this additional surface area will be at the same surface temperature as the bare surface due to conduction in the pins. This increase in surface area will therefore be corrected by a pin-fin efficiency η_f. The expected heat transfer coefficient for the pin-covered surface is therefore:

$$h_{eff,calc} A_{bare} = \left(A_{prime} + N \eta_f A_f\right) h_{bare} \tag{3.3}$$

Where: A_{bare} = 1.589×10^{-3} m^2 is the area of the original bare cooled surface, A_c = 7.854×10^{-7} m^2 is the area of a single pin tip, A_{prime} = 9.544×10^{-4} m^2 is the area of the bare surface which remains after the addition of the pins. Mathematically,

$$A_{prime} = A_{bare} - N \times A_c \tag{3.4}$$

Finally, A_f = 6.28×10^{-6} m^2 is the surface area of the pin wall which is found by multiplying the perimeter of a pin, *Per* = 3.142×10^{-3} m, by the length of the pin, *L* = 2 mm.

The fin efficiency, η_f measures the thermal performance of a single pin by comparing the maximum heat transfer rate for convection, q_{max} which would occur if A_f were at a surface temperature $T_{s,pins}$ subject to h_{bare}, to the calculated heat transfer rate, q_f which accounts for conduction resistance in the pin:

$$\eta_f \equiv \frac{q_f}{q_{\max}} = \frac{q_f}{h_{bare} A_f (T_{s,pins} - T_{in})} \tag{3.5}$$

Here, $T_{s,pins} - T_{in}$ is the temperature difference between the surface and inlet coolant temperatures for the pin-covered surface; note that this temperature difference is obtained experimentally under otherwise identical conditions as those used to measure $T_{s,bare} - T_{in}$. From the correlations given in Incropera and DeWitt [10], q_f, the pin-fin heat transfer rate, can be approximated as:

$$q_f = M \tanh(mL) \tag{3.6}$$

where

$$m = \sqrt{\frac{h_{bare}(Per)}{kA_c}} \tag{3.7}$$

and

$$M = (T_{s,pins} - T_{in}) \sqrt{h_{bare}(Per) k A_c} \tag{3.8}$$

Here, *k* is the thermal conductivity of brass at the measured surface temperature and q_f is defined assuming an adiabatic tip condition. Figure 3.3 plots $h_{eff,calc}$ and h_{eff} as a function of Re.

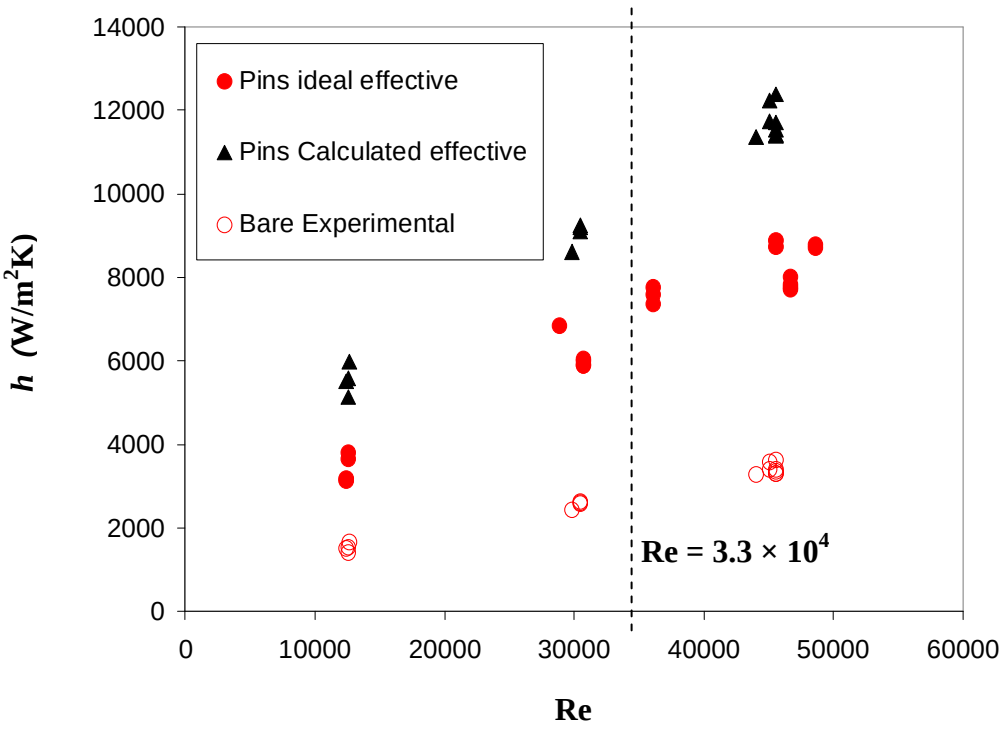

Figure 3.3: Calculated and experimental heat transfer coefficient vs. Re

The value for $h_{eff,calc}$ should be lower than h_{eff} because it does not account for other heat transfer mechanisms. The assumption of an adiabatic fin tip assumes that there is no convection past the fin tips, but there are likely to be imperfections in the contact between the pins and the surface of the aluminum insert, which would allow some convection and increase q_f. This is not accounted for in the calculation of $h_{eff,calc}$, and will increase h_{eff}. There is also some heat lost to the surroundings. Yet the results show that $h_{eff,calc}$ is consistently around 30% higher than h_{eff}. This unexpected difference may be partially explained by instrumental uncertainties. As detailed in appendix A, the uncertainty in h_{eff} depends on the uncertainties in the q''_{actual} measurement and the TC readings, and ranges from 4.4% for the high flow, high power case to 6.9% for the low flow, low power case.

The primary reason for this difference is that the calculation of $h_{eff,calc}$ accounts for the change in surface area and the fin efficiency, but it does not account for the change in flow characteristics around the pins. Until now, only the "effective" heat transfer coefficient for the pins has been discussed. Calculation of the effective heat transfer coefficient assumes that the actual heat transfer coefficient for the pins is the same as that for the bare surface. This assumption introduces error because heat transfer coefficient depends on Nu, which is a function of Re. The local Re will be much different when flowing around the pins than it is on the flat surface. Since it is impossible to experimentally determine the local Re around the pins, it is also impossible to experimentally determine the actual heat transfer coefficient associated with the pins. However, using the experimentally determined effective heat transfer coefficient, the actual heat transfer coefficient can be approximated using an iterative process. Equation 3.3 is used in the form:

$$h_{eff} A_{bare} = \left(A_{prime} + N\eta_f A_f\right) h_{actual} \tag{3.9}$$

Where h_{eff} is the experimentally determined heat transfer coefficient for the pin-covered surface. The fin efficiency is found using equations 3.5-3.8 and replacing h_{bare} with h_{actual}. h_{actual} is assumed to be h_{bare} for the first iteration. Once the fin efficiency is found, it is inserted into equation 3.9, and a new value for h_{actual} is found. This new value for h_{actual} is used to find a new value for fin efficiency, and the process is repeated until the value for h_{actual} converges. This process also gives a more accurate estimation of the fin efficiency. Figure 3.4 compares the actual heat transfer coefficient with the pins geometry against the heat transfer coefficient of the bare geometry.

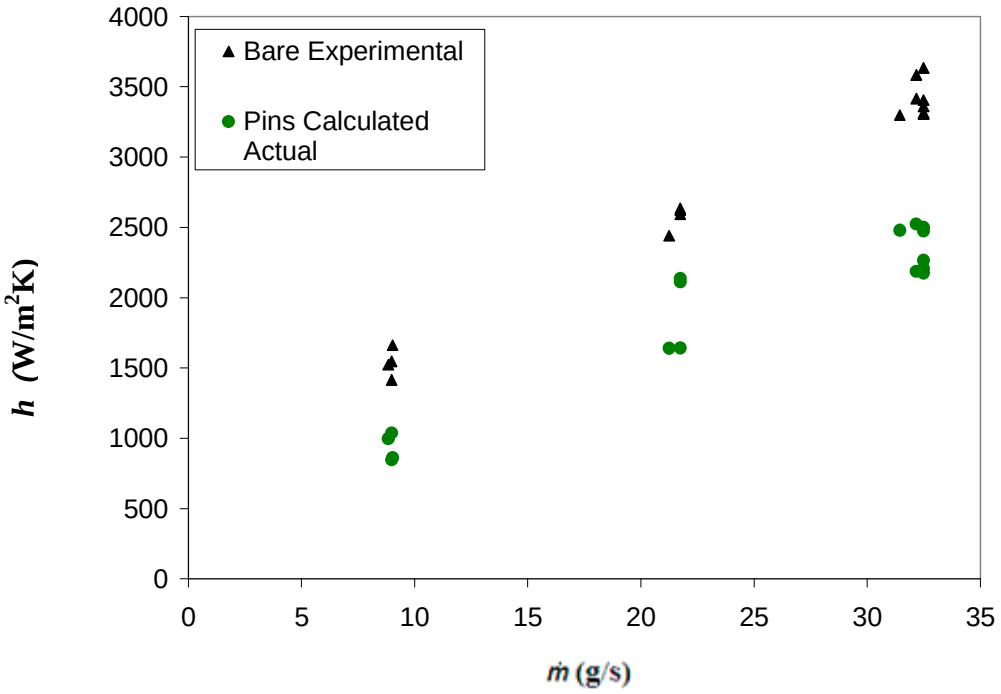

Figure 3.4: Actual heat transfer coefficient for pin-covered surface and experimentally determined heat transfer coefficient for bare surface vs. mass flow rate

Since the actual heat transfer coefficient is consistently lower than h_{bare}, using h_{bare} in the calculation of $h_{eff,calc}$ results in the overestimation of $h_{eff,calc}$ seen in figure 3.3. The value of the fin efficiency was found to be greater than 90 % and found to decrease with increasing mass flow rate. This relationship is shown in Figure 3.5:

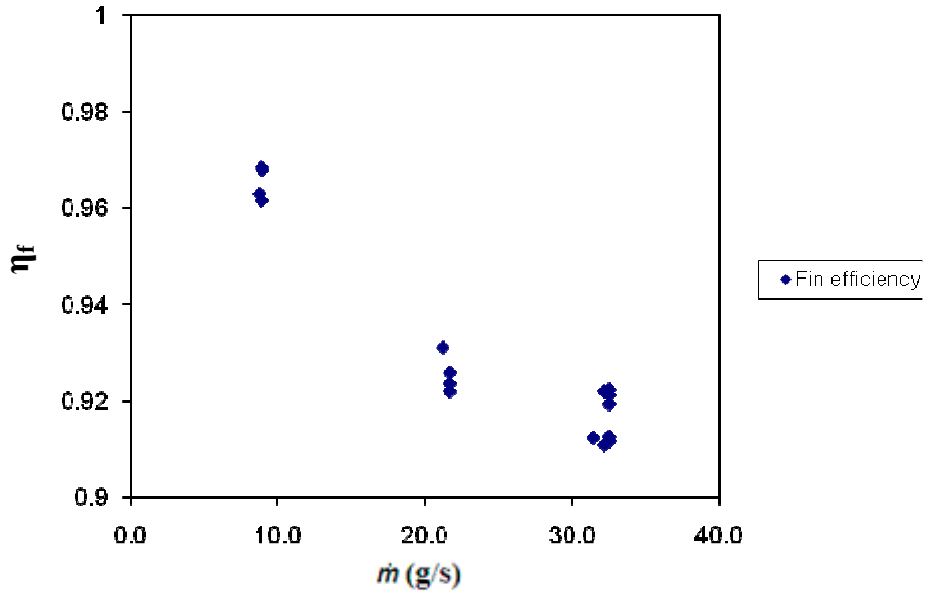

Figure 3.5: Fin efficiency vs. mass flow rate

3.4.2: Assumption of a uniform heat transfer coefficient

The experimental heat transfer coefficients used in the calculations of $h_{eff,calc}$ and h_{actual} are the average of five local heat transfer coefficients. In the calculations, the heat transfer coefficient is assumed to be uniform over the surface. The surface temperature $T_{s,pins}$ was assumed to be constant over the cooled surface when calculating $h_{eff,calc}$. This section discusses the accuracy of these assumptions and presents some representative temperature profiles.

The experimentally determined local heat transfer coefficient fluctuates only with the local surface temperature since for each location, the inlet temperature and heat flux are the same. The local heat transfer coefficient is inversely proportional to the local surface temperature, and is directly related to the accuracy of the TC measurements. As discussed in the experimental setup section, the TCs are placed symmetrically along the slot in the *x*-direction to measure the temperature profile along *x* and along the *y*-direction

to verify that temperature distribution in the 2D jet is independent of *y*-position. If the assumption of uniform heat transfer coefficient is correct, all five TC readings should give the same temperature. The manufacturer's stated instrumental uncertainty U_B is ±1.5 ˚C, and the uncertainty due to statistical fluctuation, U_A is about ±1% for the temperature profiles shown. The total experimental uncertainty $U_{\text{Total}} = \sqrt{U_A^2 + U_B^2}$ is consistently about 1.3% of the measured temperature. For the bare surface profiles shown, this means that profiles that vary by up to 2.6%, or about 6 ˚C, are considered uniform within experimental uncertainty. For the pin-covered surface profiles shown, temperature profiles with a range of 3 ˚C are considered uniform within experimental uncertainty.

Figures 3.6 and 3.7 show temperature profiles along the *x*-direction obtained from the five TCs at high flow rates (corresponding to a nominal Re of 45,000) for the bare surface and pin-covered surface, respectively. At a given heat flux, a comparison of the data shown in figures 3.6 and 3.7 shows that the variation in surface temperature for the bare surface is significantly greater than that for the pin-covered surface. The temperature measurements for cases 1233 and 2233 for the pin-covered surface, for example, vary by less than 3 ˚C and can therefore be considered uniform. The temperature measurements for the corresponding bare surface however, most notably cases 2134 and 2133, vary by as much as 20 ˚C. These data suggest that the assumption of uniform heat transfer coefficient is valid for the pin-covered surface but may lead to some error for the bare surface.

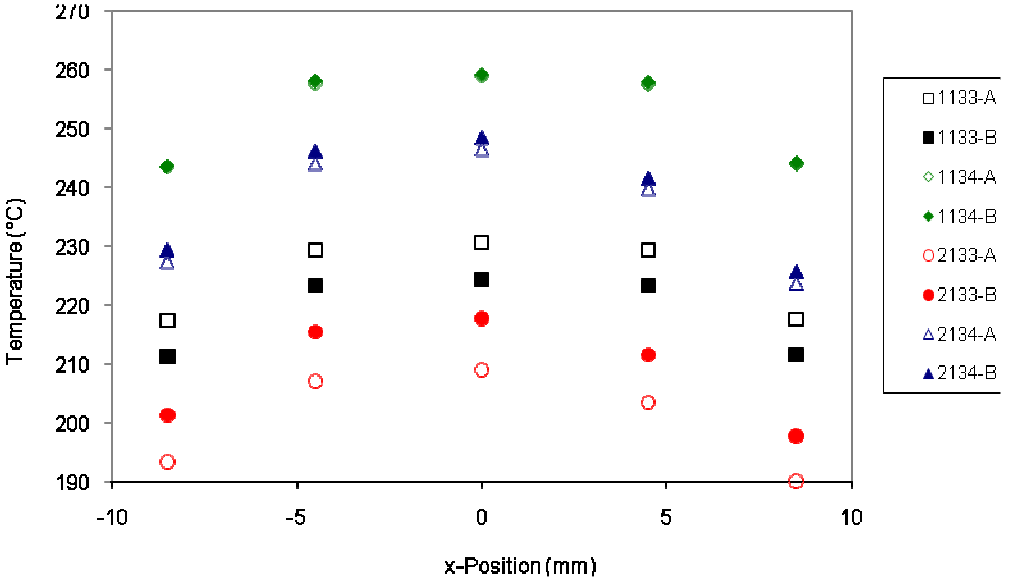

Figure 3.6: Representative bare surface geometry temperature profiles for different heat fluxes; Re = 45,000

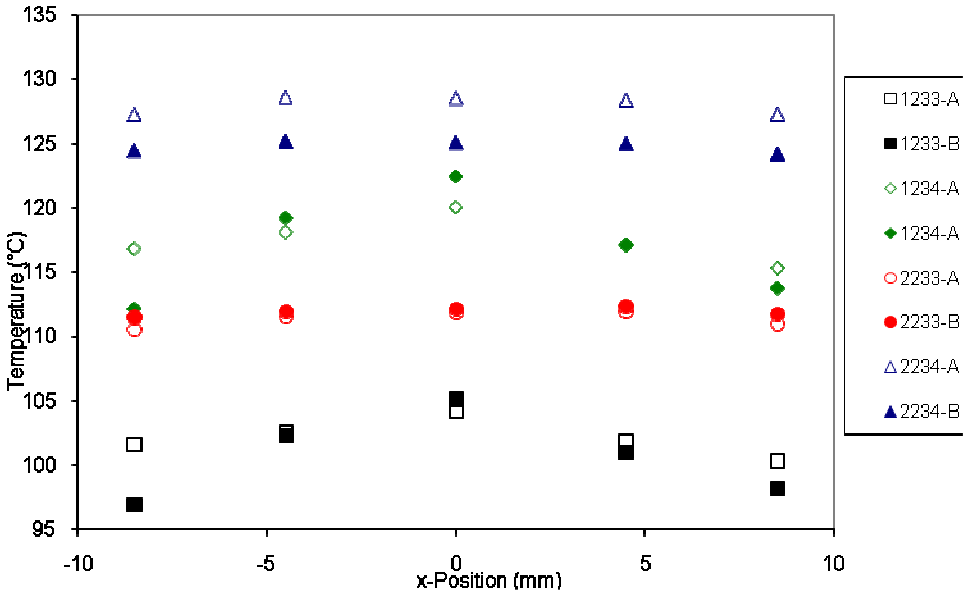

Figure 3.7: Representative pin-covered surface geometry temperature profiles for different heat fluxes at Re = 45,000

In all cases, the temperature profile is symmetric about the *y*-axis, despite the different *x*-positions of the TCs, suggesting that the surface temperature and heat transfer coefficient are uniform along *y*. The difference between the bare surface and pin-covered surface temperature profiles also suggests that the pin-covered surface creates more uniform cooling.

The surface temperature $T_{s,pins}$ is taken to be the average of the five surface thermocouple measurements for that particular case. For the pin-covered surface, this does not lead to significant error, since the temperature profiles are within experimental uncertainty.

For the bare surface, since the temperatures vary significantly in the *x*-direction, the calculations underestimate h_{eff} in the center where $x = 0$, and overestimate h_{eff} near the edges at $x = \pm 8.5$ mm Figure 3.5 shows this error graphically for cases 2134-A and 2134-B, which were the bare surface cases with the highest fluctuation in surface temperature. The average heat transfer coefficient is plotted in figure 3.5 as a uniform heat transfer coefficient. For these cases, this assumption overestimates the heat transfer coefficient at the stagnation point by about five percent. The heat transfer coefficient at the edge of the surface is underestimated by about five percent.

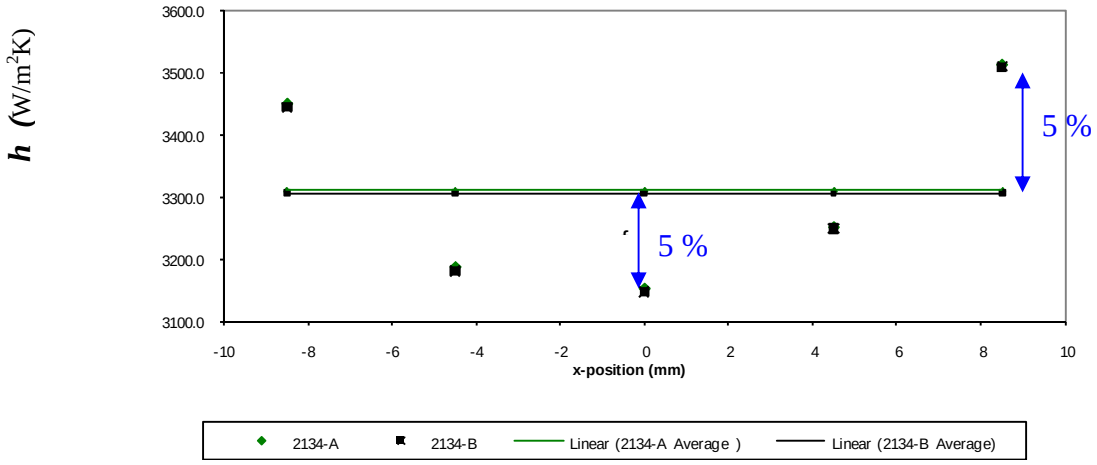

Figure 3.8: Characteristic fluctuation of local heat transfer coefficient on the bare surface showing error caused by uniform heat transfer coefficient assumption

3.5: Expected maximum heat flux

The most important objective of this study is to use the experimental results to predict the expected maximum allowable heat flux, $q''_{\max}$ that the HCFP design can withstand at various operating conditions. For these predictions, the plasma-facing side of the tungsten-alloy front plate is assumed to operate at surface temperature, T_s= 1300 ºC (1573 K), and the coolant, gaseous He, is assumed to have an inlet temperature T_{in} = 600 ºC (873 K). Since the Nusselt number Nu and the hydraulic diameter D_h are identical regardless of coolant, h_{actual} using air as the coolant h_{actual}^{air} is used to determine an expected h_{actual} using He as the coolant h_{actual}^{He}

$$h_{actual}^{He} = \frac{(Nu)k_{He}}{D_h} = \frac{\left(\frac{h_{actual}^{air} D_h}{k_{air}}\right)k_{He}}{D_h} = \left(\frac{k_{He}}{k_{air}}\right)h_{actual}^{air} \qquad (3.10)$$

The convective thermal resistance, $R_{t,conv}$ depends on the effective heat transfer coefficient for He, h_{eff}^{He}. For the bare cooled surface, $h_{actual}^{He} = h_{eff}^{He}$, and the result of equation 3.10 can be used directly to find $R_{t,conv}$. For the pin covered surface, h_{eff}^{He} is related to h_{actual}^{He} by the difference in areas and the fin efficiency:

$$h_{eff}^{He} A_{bare} = \left(A_{prime} + N\eta_f A_f\right) h_{actual}^{He} \tag{3.11}$$

The importance of considering the change in fin efficiency can be seen in Figure 3.9.

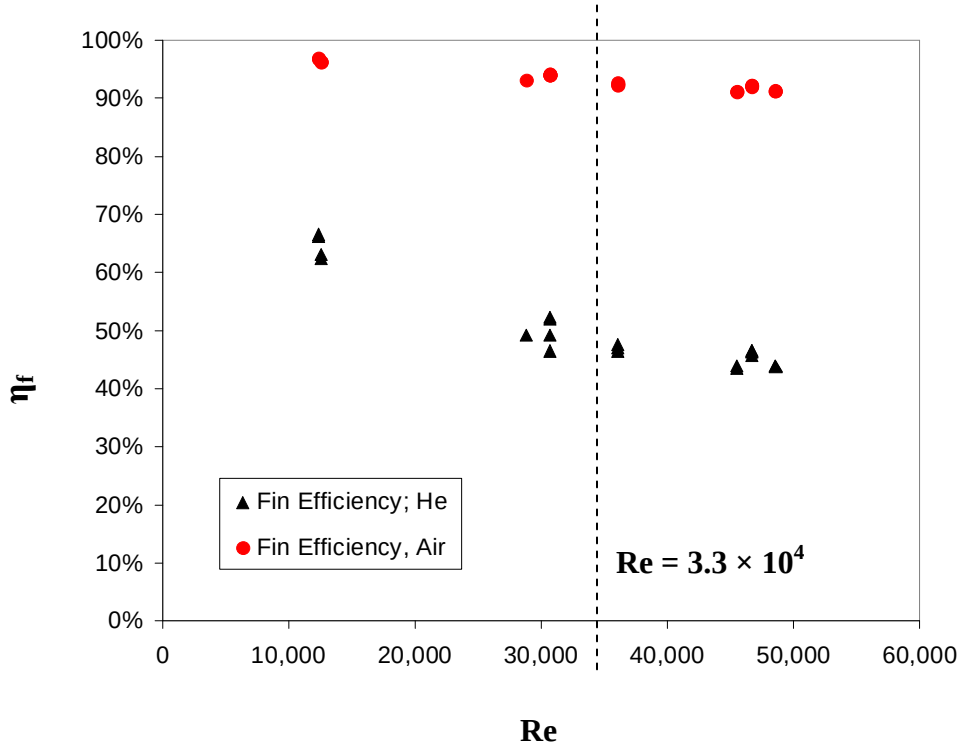

Figure 3.9: Fin efficiency vs. Re, He and air

Figure 3.9 shows that the fin efficiency drops from over 90% with air as the coolant to only about 50% in the range of the expected Re using He as the coolant. In both cases, the fin efficiency decreases with increasing flow rate. Both of these results are explained by the fact that fin efficiency decreases with increasing heat transfer coefficient. Since increasing flow rate increases heat transfer coefficient, and He has a higher heat transfer

coefficient than are because of its higher thermal conductivity, both changes result in a lower fin efficiency.

The total thermal resistance, R_{tot} is the sum of the convective thermal resistance, $R_{t,conv}$ and the conductive thermal resistance, $R_{t,cond}$.

$$R_{tot} = R_{t,conv} + R_{t,cond} = \frac{1}{h_{eff}^{He} A_{PFC}} + \frac{L_{FP}}{k_W A_{PFC}} \tag{3.12}$$

where L_{FP} = 2 mm is the thickness of the tungsten-alloy front plate. Since the particular type of tungsten alloy has not been specified for this design, the thermal conductivity of the front plate k_W = 101 W/(m-K) was taken to be that of pure tungsten at 1573 K. Also, k_{He} = 323 W/(m-K) is the thermal conductivity of He at 873 K. As discussed previously, the maximum heat flux $q''_{\max}$ is determined from the surface and coolant temperatures mentioned above and R_{tot}:

$$q''_{\max} = \frac{T_s - T_{in}}{R_{tot} A_{PFC}} \tag{3.13}$$

Figure 3.10 tabulates the predicted $q''_{\max}$ for the HCFP design at the specified operating conditions based on the experimental results over the range of operating conditions for all the geometries tested. These results show that in the range of the expected Re all four configurations can accommodate heat fluxes from 13 MW/m^2 for the bare cooled surface to 18 MW/m^2 for the pin-covered surface. For the highest flow rates, the pin-covered surface can accommodate heat fluxes exceeding 19 MW/m^2.

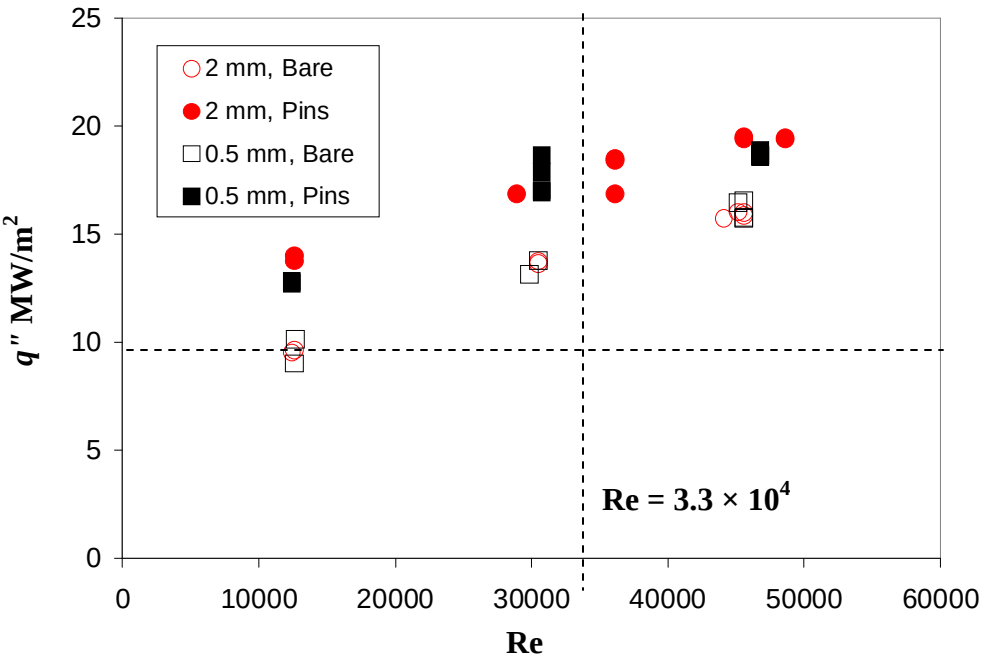

Figure 3.10: Maximum allowable heat flux

Figure 3.10 also shows that an increase in Re consistently results in an increase in q''_{max} for any configuration. This relationship should be expected since the heat transfer coefficient increases with increasing flow, and q''_{max} increases with heat transfer coefficient. Since Re only varies with mass flow rate in these experiments, q''_{max} increases with mass flow rate as well. These results suggest that q''_{max} values exceeding 19 MW/m^2 could be achieved for the 2 mm slot using a pin-fin covered surface geometry at Re exceeding 47,000. Limitations in the air supply system precluded experimental validation of this case, however.

CHAPTER 4: CONCLUSIONS AND RECOMENDATIONS

4.1: Summary

In this study, the thermal performance of four variations of a prototypical flat plate divertor:

1. 2 mm planar jet impinging on a bare surface
2. 2 mm planar jet impinging on surface, then flowing through a hexagonal pin array
3. 0.5 mm planar jet impinging on a bare surface
4. 0.5 mm planar jet impinging on surface, then flowing through a hexagonal pin array

were experimentally examined and compared with the thermal performance of the "baseline" case (#1) of a planar jet issuing from a 2 mm wide slot impinging on a bare surface. Conclusions and recommendations are made based on these experimental results.

4.2: Conclusions

The results for the 2 mm jet were compared with those for the 0.5 mm jet. This narrower jet was studied because for a given Reynolds number, this jet would have higher velocity which should give higher h_{eff} at the stagnation point. The 0.5 mm jet

consistently resulted in a lower h_{eff} and a significantly higher pressure drop than the 2 mm jet, however.

Comparing the results for the same jet impinging on a bare, *vs.* pin fin-covered, surface shows that adding a hexagonal array of 808 cylindrical pin-fins raised h_{eff} by as much as 180% and by at least 90% in all experiments. The increase in pressure drop associated with the pin-fin array was 40%-80% for the H = 2 mm jet with a corresponding increase in h_{eff} of nearly 150%. For the H = 0.5 mm jet, the pin fins increased the pressure drop by about 60% at Re = 45,000, and had almost no effect on the pressure drop at Re = 12,000, with an increase of about 100% in h_{eff} .

These results suggest that case #2, where a H = 2 mm jet impinges on the surface, then flows through an array of pin-fins, has the best thermal performance of these four configurations because it has the greatest increase in h_{eff} with a modest increase in pressure drop. Case #3, where a 0.5 mm jet impinges on a bare surface, has the worst thermal performance, with h_{eff} values comparable to the baseline case and significant increases in pressure drop for Re = 45,000. Estimates of the maximum heat that can be accommodated by these variations of the flat plate-type divertor suggest that increases in the coolant mass flow rate will also increase h_{eff} for all four configurations, albeit at the "cost" of higher pressure drop.

4.3: Future work, recommendations

Future research of the HCFP concept should focus on four goals:

1. Testing the HCFP geometry at higher heat fluxes to more closely match the expected operating conditions: This study has only tested the HCFP design at heat fluxes up to 0.72 MW/m^2, *vs.* the expected heat load of at least 10 MW/m^2. Obtaining experimental results at higher heat fluxes will increase confidence in the applicability of these results to the higher incident heat fluxes typical of plasma-facing components.
2. Testing the HCFP geometry using helium as the coolant: The effective heat transfer coefficient for He in this study was estimated based on the experimentally determined heat transfer coefficient for air. Directly experimenting with helium will provide a more accurate measurement.
3. Using the experimental data from this study to validate Computational Fluid Dynamics (CFD) models of this flow: In previous studies of other gas-cooled divertor designs, the experimental data have been compared against and used to validate numerical simulations of these designs that were performed with the FLUENT® CFD software package.
4. Using these validated CFD models to optimize the width of the slot and the geometry of the pin-fin array: Once validated, these numerical models can then be used to efficiently and economically determine optimal geometries for the pin-fin array (by varying the pitch and size of the pin fins, for example) and optimal values for slot width that maximize the increase in heat transfer coefficient while minimizing the associated pressure drop. Such an optimized geometry could then be tested experimentally.

APPENDIX A: ERROR ANALYSIS

This appendix quantifies the uncertainties associated with the experimental measurements and results. The total uncertainty associated with any measurement is the root-mean-square of the uncertainty due to statistical fluctuations, U_A and the uncertainty due to instrumentation, U_B. The uncertainty due to statistical fluctuations was determined by using a sample of 60 measurements, assuming a Gaussian distribution with a 95% confidence interval, and using formula A.1. The multiplier "z" was determined from a table in Vardeman and Jobe, and z =1.9 for all two-sided 95% confidence intervals. The uncertainty due to instrumentation was determined from given manufacturer specifications. An error propagation formula (A.3) is used to determine the uncertainty of derived quantities.

$$U_A = z\sigma_{Sample} \tag{A.1}$$

$$\sigma_{sample} = \sqrt{\frac{1}{N-1}\sum\left(x_i - \bar{x}\right)^2} \tag{A.2}$$

$$U_X\left(i, j.., k\right) = \sqrt{U_i^2\left(\frac{\partial X}{\partial i}\right)^2 + U_j^2\left(\frac{\partial X}{\partial j}\right)^2 + ... + U_k^2\left(\frac{\partial X}{\partial k}\right)^2} \tag{A.3}$$

$$U_{Total} = \sqrt{U_A^2 + U_B^2} \tag{A.4}$$

A.1 Uncertainty in Thermocouple Measurements

The manufacturer's stated instrumental uncertainty in the Omega thermocouples is ±1.5 ˚C. This is U_B. U_A is found using a representative set of 60 data points at nominal flow and power, which is the data collected for 30 minutes at steady state operation. As previously discussed, a 95% Gaussian confidence interval where z =1.9 is used to determine U_A. The total uncertainty for each thermocouple in each of the three power cases is shown in Tables A.1, A.2, and A.3.

Table A.1: Thermocouple uncertainty for low power case

	mean T [˚C]	σ_{sample}	U_A [˚C]	U_B [˚C]	U_{total} [˚C]
T1	195.5	1.089	2.068	1.50	2.55
T2	196.0	1.092	2.075	1.50	2.56
T3	186.4	1.037	1.971	1.50	2.48
T4	184.3	0.981	1.864	1.50	2.39
T5	193.5	1.013	1.924	1.50	2.44
T6	211.1	1.070	2.032	1.50	2.53
T7	214.3	1.060	2.014	1.50	2.51
T8	217.2	1.044	1.983	1.50	2.49
T9	211.0	1.048	1.991	1.50	2.49
T10	213.6	1.061	2.017	1.50	2.51
T11	216.7	1.082	2.056	1.50	2.55
Tin	23.4	0.432	0.820	1.50	1.71
Tout	64.1	0.409	0.778	1.50	1.69

Table A.2: Thermocouple uncertainty for medium power case

	mean T [˚C]	σ_{sample}	U_A [˚C]	U_B [˚C]	U_{total} [˚C]
T1	223.8	0.972	1.847	1.50	2.38
T2	227.2	1.068	2.029	1.50	2.52
T3	208.0	1.064	2.021	1.50	2.52
T4	210.7	1.046	1.988	1.50	2.49
T5	221.0	1.092	2.074	1.50	2.56
T6	261.8	0.764	1.451	1.50	2.09
T7	267.6	0.746	1.417	1.50	2.06
T8	273.7	0.719	1.367	1.50	2.03
T9	262.4	0.792	1.505	1.50	2.12
T10	267.3	0.777	1.476	1.50	2.10
T11	273.7	0.776	1.474	1.50	2.10
Tin	22.1	0.653	1.241	1.50	1.95
Tout	53.9	1.030	1.956	1.50	2.47

Table A.3: Thermocouple uncertainty for high power case

	mean T [˚C]	σ_{sample}	U_A [˚C]	U_B [˚C]	U_{total} [˚C]
T1	246.2	1.482	2.816	1.50	3.19
T2	248.6	1.481	2.815	1.50	3.19
T3	229.5	1.361	2.586	1.50	2.99
T4	225.7	1.559	2.963	1.50	3.32
T5	241.7	1.628	3.093	1.50	3.44
T6	297.5	1.894	3.599	1.50	3.90
T7	306.3	1.975	3.753	1.50	4.04
T8	315.0	2.007	3.813	1.50	4.10
T9	298.5	1.920	3.648	1.50	3.94
T10	305.3	1.986	3.774	1.50	4.06
T11	314.9	2.017	3.831	1.50	4.11
Tin	21.9	0.393	0.748	1.50	1.68
Tout	52.7	0.753	1.431	1.50	2.07

A.2: Uncertainty in mass flow rate

The mass flow rate is measured from an analog Rotameter. Therefore, statistical fluctuations cannot be detected. The flow rate is obtained in SCFM and converted to grams per second using equation A.5 which accounts for changes in temperature and pressure:

$$\dot{m}(SCFM)\sqrt{\frac{101353(Pa)}{P_{rot}(Pa)}}\ 4.71947E^{-4}\left(\frac{m^3/\sec}{ft^3/\min}\right)\rho_{rot}\left(\frac{kg}{m^3}\right)1000\frac{g}{kg}=\dot{m}\left(\frac{g}{s}\right) \quad \text{(A.5)}$$

Since ρ_{rot} depends on both the temperature and pressure in the rotameter, the mass flow rate (MFR) uncertainty depends on the rotameter reading of SCFM, T_{in}, and P_{gauge}. The resolution uncertainty of the rotameter is ± 0.5 of the smallest graduation, or 0.5 SCFM. Statistical and gauge uncertainties have already been determined for the T_{in} reading, and are listed in the tables in section A.1. Inlet pressure or P_{gauge} is subject to both gauge and resolution uncertainty, but statistical uncertainty is not considered since an analog meter is used. The pressure gauge uncertainty is listed as ± 3% of full scale, which is ± 3psi. The pressure gauge resolution uncertainty is ± 0.5 the smallest graduation, or 1psi. The uncertainties in SCFM, psi, and ˚C correspond to varying uncertainties in g/s, depending on the flow case. Therefore, uncertainty analysis has been done on three representative flow cases, and the results are tabulated in table A.4.

Table A.4: Mass flow rate uncertainty

	Corresponding Uncertainty in g/s					
Nominal RE	**SCFM**	**T_{in}**	**P_{guage}**	**$P_{resolution}$**	**U_{MFR}**	**% U_{MFR} (+/-)**
12,000	0.64	0.05	0.21	0.07	0.68 g/s	7.50%
30,000	0.64	0.14	0.69	0.23	0.98 g/s	4.50%
45,000	0.64	0.19	0.68	0.22	0.98 g/s	3.00%

A.3: Uncertainty in pressure drop

An Omega PX26-100DV series pressure transducer was used to digitally record the pressure drop across the test section. The manufacturer's stated accuracy is 1% of full scale, which is 1 psi. This is U_B. As in the temperature measurements, the statistical uncertainty, U_A is found using a representative sample of 60 data points collected at steady state operation, and representing 30 minutes of data. Once again, a two-sided 95% Gaussian confidence interval with z =1.9 is used, and tabulated for three separate flow cases. The results are shown in table A.5:

Table A.5: Pressure drop uncertainty

Nominal RE	**Mean P (psi)**	**σ_{sample}**	**U_A**	**U_B**	**U_{total}**	**%U(+/-)**
12,000	0.50	0.046	0.09	1.00	1.00	202.2%
30,000	12.87	0.342	0.65	1.00	1.19	9.3%
45,000	26.33	1.484	2.82	1.00	2.99	11.4%

A.4: Uncertainty in power measurement

The recorded power measurements are simply a product of the digitally recorded voltage measurements and the analog current reading. Therefore, the total uncertainty in the power measurement is a function of the instrumental and statistical uncertainty of the

voltage measurement, and the resolution uncertainty of the ammeter. The manufacturer's stated tolerance of the Agilent data acquisition unit which reads voltage is 0.01%. Using a two-sided 95% Gaussian confidence interval with 60 data points where z =1.9, statistical voltage uncertainty is found. The resolution of the ammeter is 0.5 of the smallest graduation, or 0.5 Amp. These uncertainties in voltage and current correspond to different uncertainties in power, depending on the power setting. Calculated uncertainties for the three basic power cases are shown in table A.6.

Table A.6: Heat flux uncertainty

Power Case	U_V (Watts)	U_C (Watts)	U_{total} (Watts)	% U (+/-)
Low	9.93	26.03	27.86	7.4%
Medium	9.43	37.81	38.97	4.9%
High	18.13	45.58	49.05	4.4%

A.5: Uncertainty in heat transfer coefficient

The uncertainty in the heat transfer coefficient is a product of the heat flux, the inlet temperature, T_{in} and the average surface temperature, T_s. The heat flux is calculated by dividing the power in by the cooled surface area, and there is no appreciable uncertainty in the cooled surface area. Therefore, the uncertainty in heat flux is proportional to the uncertainty in the power. The uncertainties in T_{in} and T_s are tabulated in section A.1, and correspond to different uncertainties in h_{eff} depending on the power and flow case. A form of equation A.3 is used to scale the effects of the temperature and heat flux uncertainties. The exact equation used is equation A.6:

$$U_{HTC} = \sqrt{U_{q''}^2 \frac{1}{\left(T_s - T_{in}\right)^2} + \left(U_{T_s}^2 + U_{T_{in}}^2\right) \frac{q''^2}{\left(T_s - T_{in}\right)^4}} \tag{A.6}$$

In this equation, T_s is the average of TC's 1-5, and U_{Ts} is the root-mean-square of the uncertainties of those same five TC's.

For the low flow, low power case, this resulted in U_{HTC} = ±102.4 W/m^{2}K or ±6.9%. For the medium flow, medium power case, this resulted in U_{HTC} = ±125.4 W/m^{2}K or ±5%. For the high flow, high power case, this resulted in U_{HTC} = ± 145.3 W/m^{2}K or ±4.4%.

APPENDIX B: EXPERIMENTAL SUMMARY TABLES

Table B.1: 1111

	Run 1	Run 2	Units	Description
$\dot{m}$	8.99	8.84	[g/s]	Measured Mass Flow Rate
Re	12,590	12,390	[-]	Jet Reynolds Number
$\mathbf{Q_{in}}$	373.6	383.8	[W]	Nominal Power Input
$\mathbf{Q_{out}}$	359.4	360.2	[W]	Power Out = $\dot{m}\, c_p(T_{out} - T_{in})$
% Losses	4%	6%	[-]	Heat Loss
q''_{actual}	0.224	0.230	[MW/m^2]	Incident Heat Flux
$\mathbf{P_{rot}}$	62	50	[psig]	Rotameter Pressure
$\mathbf{P_{out}}$	60	48	[psig]	Outlet Pressure
ΔP	0.16	0.29	[psi]	Measured Pressure Drop
$\mathbf{T_{in}}$	23.79	22.7	[^{o}C]	Inlet Temperature
$\mathbf{T_{out}}$	63.28	62.97	[^{o}C]	Outlet Temperature
$\mathbf{T_1}$	178.86	183.23	[^{o}C]	Embedded TC Ref. 1 in brass
$\mathbf{T_2}$	178.79	183.11	[^{o}C]	Embedded TC Ref. 2 in brass
$\mathbf{T_3}$	173.87	179.90	[^{o}C]	Embedded TC Ref. 3 in brass
$\mathbf{T_4}$	173.39	180.87	[^{o}C]	Embedded TC Ref. 4 in brass
$\mathbf{T_5}$	177.85	183.16	[^{o}C]	Embedded TC Ref. 5 in brass
$\mathbf{T_6}$	193.72	204.98	[^{o}C]	TC Ref. 6 in copper "neck"
$\mathbf{T_7}$	196.66	208.31	[^{o}C]	TC Ref. 7 in copper "neck"
$\mathbf{T_8}$	199.06	211.02	[^{o}C]	TC Ref. 8 in copper "neck"
$\mathbf{T_9}$	193.04	204.68	[^{o}C]	TC Ref. 9 in copper "neck"
$\mathbf{T_{10}}$	195.23	206.50	[^{o}C]	TC Ref. 10 in copper "neck"
$\mathbf{T_{11}}$	198.17	209.56	[^{o}C]	TC Ref. 11 in copper "neck"
$\mathbf{T_{peak\_1}}$	218.45	230.66	[^{o}C]	Peak Copper Temperature TC 1
$\mathbf{T_{peak\_2}}$	218.53	230.81	[^{o}C]	Peak Copper Temperature TC 2

Table B.2: 2111

	Run 1	Run 2	Units	Description
$\dot{m}$	8.99	9.025	[g/s]	Measured Mass Flow Rate
Re	12,590	12,652	[-]	Jet Reynolds Number
$\mathbf{Q_{in}}$	384.5	375.5	[W]	Nominal Power Input
$\mathbf{Q_{out}}$	370.4	344.2	[W]	Power Out = $\dot{m}\, c_p(T_{out} - T_{in})$
% Losses	4%	8%	[-]	Heat Loss
q''_{actual}	0.230	0.225	[MW/m^2]	Incident Heat Flux
$\mathbf{P_{rot}}$	62	51	[psig]	Rotameter Pressure
$\mathbf{P_{out}}$	60	48	[psig]	Outlet Pressure
ΔP	0.497	0.497	[psi]	Measured Pressure Drop
$\mathbf{T_{in}}$	23.44	22.19	[^{o}C]	Inlet Temperature
$\mathbf{T_{out}}$	64.14	59.83	[^{o}C]	Outlet Temperature
$\mathbf{T_1}$	195.52	171.34	[^{o}C]	Embedded TC Ref. 1 in brass
$\mathbf{T_2}$	195.98	173.32	[^{o}C]	Embedded TC Ref. 2 in brass
$\mathbf{T_3}$	186.44	163.74	[^{o}C]	Embedded TC Ref. 3 in brass
$\mathbf{T_4}$	184.28	164.97	[^{o}C]	Embedded TC Ref. 4 in brass
$\mathbf{T_5}$	193.47	170.3836	[^{o}C]	Embedded TC Ref. 5 in brass
$\mathbf{T_6}$	211.13	187.96	[^{o}C]	TC Ref. 6 in copper "neck"
$\mathbf{T_7}$	214.31	190.90	[^{o}C]	TC Ref. 7 in copper "neck"
$\mathbf{T_8}$	217.18	193.69	[^{o}C]	TC Ref. 8 in copper "neck"
$\mathbf{T_9}$	210.98	187.76	[^{o}C]	TC Ref. 9 in copper "neck"
$\mathbf{T_{10}}$	213.58	189.99	[^{o}C]	TC Ref. 10 in copper "neck"
$\mathbf{T_{11}}$	216.73	192.91	[^{o}C]	TC Ref. 11 in copper "neck"
$\mathbf{T_{peak\_1}}$	237.78	213.32	[^{o}C]	Peak Copper Temperature TC 1
$\mathbf{T_{peak\_2}}$	237.96	213.41	[^{o}C]	Peak Copper Temperature TC 2

Table B.3: 1122

	Run 1	Run 2	Units	Description
$\dot{m}$	21.74	21.74	[g/s]	Measured Mass Flow Rate
Re	30,493	30,493	[-]	Jet Reynolds Number
$\mathbf{Q_{in}}$	810.0	817.5	[W]	Nominal Power Input
$\mathbf{Q_{out}}$	723.8	728.4	[W]	Power Out = $\dot{m}\, c_p(T_{out} - T_{in})$
% Losses	11%	11%	[-]	Heat Loss
q''_{actual}	0.485	0.490	[MW/m^2]	Incident Heat Flux
$\mathbf{P_{rot}}$	33	33	[psig]	Rotameter Pressure
$\mathbf{P_{out}}$	22	22	[psig]	Outlet Pressure
ΔP	8.43	8.02	[psi]	Measured Pressure Drop
$\mathbf{T_{in}}$	23.02	21.97	[^{o}C]	Inlet Temperature
$\mathbf{T_{out}}$	55.92	55.07	[^{o}C]	Outlet Temperature
$\mathbf{T_1}$	227.37	223.23	[^{o}C]	Embedded TC Ref. 1 in brass
$\mathbf{T_2}$	226.55	221.86	[^{o}C]	Embedded TC Ref. 2 in brass
$\mathbf{T_3}$	215.73	216.47	[^{o}C]	Embedded TC Ref. 3 in brass
$\mathbf{T_4}$	215.87	218.32	[^{o}C]	Embedded TC Ref. 4 in brass
$\mathbf{T_5}$	224.72	222.81	[^{o}C]	Embedded TC Ref. 5 in brass
$\mathbf{T_6}$	260.95	267.31	[^{o}C]	TC Ref. 6 in copper "neck"
$\mathbf{T_7}$	266.79	273.65	[^{o}C]	TC Ref. 7 in copper "neck"
$\mathbf{T_8}$	272.27	279.42	[^{o}C]	TC Ref. 8 in copper "neck"
$\mathbf{T_9}$	260.17	266.81	[^{o}C]	TC Ref. 9 in copper "neck"
$\mathbf{T_{10}}$	265.31	270.81	[^{o}C]	TC Ref. 10 in copper "neck"
$\mathbf{T_{11}}$	271.75	277.31	[^{o}C]	TC Ref. 11 in copper "neck"
$\mathbf{T_{peak\_1}}$	314.05	319.95	[^{o}C]	Peak Copper Temperature TC 1
$\mathbf{T_{peak\_2}}$	314.24	320.26	[^{o}C]	Peak Copper Temperature TC 2

Table B.4: 2122

	Run 1	Run 2	Units	Description
$\dot{m}$	21.74	21.25	[g/s]	Measured Mass Flow Rate
Re	30,493	29820	[-]	Jet Reynolds Number
$\mathbf{Q_{in}}$	809.8	810.9	[W]	Nominal Power Input
$\mathbf{Q_{out}}$	699.6	700.4	[W]	Power Out = $\dot{m}\, c_p(T_{out} - T_{in})$
% Losses	14%	14%	[-]	Heat Loss
q''_{actual}	0.485	0.486	[MW/m^2]	Incident Heat Flux
$\mathbf{P_{rot}}$	33	32	[psig]	Rotameter Pressure
$\mathbf{P_{out}}$	16	15	[psig]	Outlet Pressure
ΔP	12.9	12.87	[psi]	Measured Pressure Drop
$\mathbf{T_{in}}$	22.08	22.20	[^{o}C]	Inlet Temperature
$\mathbf{T_{out}}$	53.87	54.77	[^{o}C]	Outlet Temperature
$\mathbf{T_1}$	223.79	239.23	[^{o}C]	Embedded TC Ref. 1 in brass
$\mathbf{T_2}$	227.24	241.95	[^{o}C]	Embedded TC Ref. 2 in brass
$\mathbf{T_3}$	208.01	224.00	[^{o}C]	Embedded TC Ref. 3 in brass
$\mathbf{T_4}$	210.70	226.68	[^{o}C]	Embedded TC Ref. 4 in brass
$\mathbf{T_5}$	221.01	236.90	[^{o}C]	Embedded TC Ref. 5 in brass
$\mathbf{T_6}$	261.78	285.62	[^{o}C]	TC Ref. 6 in copper "neck"
$\mathbf{T_7}$	267.58	291.79	[^{o}C]	TC Ref. 7 in copper "neck"
$\mathbf{T_8}$	273.74	297.94	[^{o}C]	TC Ref. 8 in copper "neck"
$\mathbf{T_9}$	262.36	285.84	[^{o}C]	TC Ref. 9 in copper "neck"
$\mathbf{T_{10}}$	267.34	290.91	[^{o}C]	TC Ref. 10 in copper "neck"
$\mathbf{T_{11}}$	273.72	297.57	[^{o}C]	TC Ref. 11 in copper "neck"
$\mathbf{T_{peak\_1}}$	315.45	339.86	[^{o}C]	Peak Copper Temperature TC 1
$\mathbf{T_{peak\_2}}$	315.75	340.43	[^{o}C]	Peak Copper Temperature TC 2

Table B.5: 1133

	Run 1	Run 2	Units	Description
$\dot{m}$	31.44	32.49	[g/s]	Measured Mass Flow Rate
Re	44,067	45,530	[-]	Jet Reynolds Number
$\mathbf{Q_{in}}$	1058.1	1044.3	[W]	Nominal Power Input
$\mathbf{Q_{out}}$	910.4	891.6	[W]	Power Out = $\dot{m}\, c_p(T_{out} - T_{in})$
% Losses	14%	15%	[-]	Heat Loss
q''_{actual}	0.634	0.625	[MW/m^2]	Incident Heat Flux
$\mathbf{P_{rot}}$	56.1	58	[psig]	Rotameter Pressure
$\mathbf{P_{out}}$	40	40	[psig]	Outlet Pressure
ΔP	12.10	12.67	[psi]	Measured Pressure Drop
$\mathbf{T_{in}}$	19.60	19.73	[^{o}C]	Inlet Temperature
$\mathbf{T_{out}}$	48.21	46.85	[^{o}C]	Outlet Temperature
$\mathbf{T_1}$	229.47	223.40	[^{o}C]	Embedded TC Ref. 1 in brass
$\mathbf{T_2}$	230.76	224.45	[^{o}C]	Embedded TC Ref. 2 in brass
$\mathbf{T_3}$	217.42	211.36	[^{o}C]	Embedded TC Ref. 3 in brass
$\mathbf{T_4}$	217.75	211.65	[^{o}C]	Embedded TC Ref. 4 in brass
$\mathbf{T_5}$	229.48	223.30	[^{o}C]	Embedded TC Ref. 5 in brass
$\mathbf{T_6}$	279.52	272.60	[^{o}C]	TC Ref. 6 in copper "neck"
$\mathbf{T_7}$	269.73	263.44	[^{o}C]	TC Ref. 7 in copper "neck"
$\mathbf{T_8}$	294.90	287.76	[^{o}C]	TC Ref. 8 in copper "neck"
$\mathbf{T_9}$	278.49	271.63	[^{o}C]	TC Ref. 9 in copper "neck"
$\mathbf{T_{10}}$	284.83	277.87	[^{o}C]	TC Ref. 10 in copper "neck"
$\mathbf{T_{11}}$	293.12	286.12	[^{o}C]	TC Ref. 11 in copper "neck"
$\mathbf{T_{peak\_1}}$	348.20	340.40	[^{o}C]	Peak Copper Temperature TC 1
$\mathbf{T_{peak\_2}}$	348.66	340.84	[^{o}C]	Peak Copper Temperature TC 2

Table B.6: 1134

	Run 1	Run 2	Units	Description
$\dot{m}$	32.17	32.49	[g/s]	Measured Mass Flow Rate
Re	45,092	45,530	[-]	Jet Reynolds Number
$\mathbf{Q_{in}}$	1240.0	1238.1	[W]	Nominal Power Input
$\mathbf{Q_{out}}$	1053.6	1057.8	[W]	Power Out = $\dot{m}\, c_p(T_{out} - T_{in})$
% Losses	15%	15%	[-]	Heat Loss
q''_{actual}	0.742	0.741	[MW/m^2]	Incident Heat Flux
$\mathbf{P_{rot}}$	58	58	[psig]	Rotameter Pressure
$\mathbf{P_{out}}$	41	40	[psig]	Outlet Pressure
ΔP	12.33	12.58	[psi]	Measured Pressure Drop
$\mathbf{T_{in}}$	19.78	19.76	[^{o}C]	Inlet Temperature
$\mathbf{T_{out}}$	52.14	51.93	[^{o}C]	Outlet Temperature
$\mathbf{T_1}$	257.63	258.15	[^{o}C]	Embedded TC Ref. 1 in brass
$\mathbf{T_2}$	258.93	259.12	[^{o}C]	Embedded TC Ref. 2 in brass
$\mathbf{T_3}$	243.67	243.68	[^{o}C]	Embedded TC Ref. 3 in brass
$\mathbf{T_4}$	244.12	257.88	[^{o}C]	Embedded TC Ref. 4 in brass
$\mathbf{T_5}$	257.53	244.28	[^{o}C]	Embedded TC Ref. 5 in brass
$\mathbf{T_6}$	315.93	316.82	[^{o}C]	TC Ref. 6 in copper "neck"
$\mathbf{T_7}$	306.20	307.66	[^{o}C]	TC Ref. 7 in copper "neck"
$\mathbf{T_8}$	333.64	334.60	[^{o}C]	TC Ref. 8 in copper "neck"
$\mathbf{T_9}$	314.85	315.82	[^{o}C]	TC Ref. 9 in copper "neck"
$\mathbf{T_{10}}$	322.18	323.18	[^{o}C]	TC Ref. 10 in copper "neck"
$\mathbf{T_{11}}$	331.79	332.89	[^{o}C]	TC Ref. 11 in copper "neck"
$\mathbf{T_{peak\_1}}$	395.30	396.71	[^{o}C]	Peak Copper Temperature TC 1
$\mathbf{T_{peak\_2}}$	395.84	397.13	[^{o}C]	Peak Copper Temperature TC 2

Table B.7: 2133

	Run 1	Run 2	Units	Description
$\dot{m}$	32.49	32.17	[g/s]	Measured Mass Flow Rate
Re	45,530	45,092	[-]	Jet Reynolds Number
$\mathbf{Q_{in}}$	1027.8	1046.8	[W]	Nominal Power Input
$\mathbf{Q_{out}}$	813.9	852.7	[W]	Power Out = $\dot{m}\, c_p(T_{out} - T_{in})$
% Losses	21%	19%	[-]	Heat Loss
q''_{actual}	0.615	0.627	[MW/m^2]	Incident Heat Flux
$\mathbf{P_{rot}}$	58	58	[psig]	Rotameter Pressure
$\mathbf{P_{out}}$	22	27	[psig]	Outlet Pressure
ΔP	25.58	26.20	[psi]	Measured Pressure Drop
$\mathbf{T_{in}}$	19.00	21.25	[^{o}C]	Inlet Temperature
$\mathbf{T_{out}}$	43.75	47.45	[^{o}C]	Outlet Temperature
$\mathbf{T_1}$	207.17	215.56	[^{o}C]	Embedded TC Ref. 1 in brass
$\mathbf{T_2}$	209.09	217.81	[^{o}C]	Embedded TC Ref. 2 in brass
$\mathbf{T_3}$	193.48	201.36	[^{o}C]	Embedded TC Ref. 3 in brass
$\mathbf{T_4}$	190.23	197.80	[^{o}C]	Embedded TC Ref. 4 in brass
$\mathbf{T_5}$	203.63	211.65	[^{o}C]	Embedded TC Ref. 5 in brass
$\mathbf{T_6}$	249.40	259.55	[^{o}C]	TC Ref. 6 in copper "neck"
$\mathbf{T_7}$	256.71	267.10	[^{o}C]	TC Ref. 7 in copper "neck"
$\mathbf{T_8}$	264.02	274.75	[^{o}C]	TC Ref. 8 in copper "neck"
$\mathbf{T_9}$	249.79	260.23	[^{o}C]	TC Ref. 9 in copper "neck"
$\mathbf{T_{10}}$	255.35	266.06	[^{o}C]	TC Ref. 10 in copper "neck"
$\mathbf{T_{11}}$	263.24	274.37	[^{o}C]	TC Ref. 11 in copper "neck"
$\mathbf{T_{peak\_1}}$	315.06	327.93	[^{o}C]	Peak Copper Temperature TC 1
$\mathbf{T_{peak\_2}}$	315.37	328.28	[^{o}C]	Peak Copper Temperature TC 2

Table B.8: 2134

	Run 1	Run 2	Units	Description
$\dot{m}$	32.49	32.49	[g/s]	Measured Mass Flow Rate
Re	45,530	45,530	[-]	Jet Reynolds Number
$\mathbf{Q_{in}}$	1121.2	1116.9	[W]	Nominal Power Input
$\mathbf{Q_{out}}$	1009	1014.7	[W]	Power Out = $\dot{m}\, c_p(T_{out} - T_{in})$
% Losses	10%	9%	[-]	Heat Loss
q''_{actual}	0.671	0.669	[MW/m^2]	Incident Heat Flux
$\mathbf{P_{rot}}$	58	58	[psig]	Rotameter Pressure
$\mathbf{P_{out}}$	22	22	[psig]	Outlet Pressure
ΔP	26.28	26.33	[psi]	Measured Pressure Drop
$\mathbf{T_{in}}$	19.39	21.88	[^{o}C]	Inlet Temperature
$\mathbf{T_{out}}$	50.10	52.75	[^{o}C]	Outlet Temperature
$\mathbf{T_1}$	244.13	246.24	[^{o}C]	Embedded TC Ref. 1 in brass
$\mathbf{T_2}$	246.54	248.60	[^{o}C]	Embedded TC Ref. 2 in brass
$\mathbf{T_3}$	227.41	229.47	[^{o}C]	Embedded TC Ref. 3 in brass
$\mathbf{T_4}$	223.77	225.71	[^{o}C]	Embedded TC Ref. 4 in brass
$\mathbf{T_5}$	239.80	241.66	[^{o}C]	Embedded TC Ref. 5 in brass
$\mathbf{T_6}$	295.77	297.50	[^{o}C]	TC Ref. 6 in copper "neck"
$\mathbf{T_7}$	304.53	306.25	[^{o}C]	TC Ref. 7 in copper "neck"
$\mathbf{T_8}$	313.39	315.04	[^{o}C]	TC Ref. 8 in copper "neck"
$\mathbf{T_9}$	296.61	298.47	[^{o}C]	TC Ref. 9 in copper "neck"
$\mathbf{T_{10}}$	303.45	305.34	[^{o}C]	TC Ref. 10 in copper "neck"
$\mathbf{T_{11}}$	313.02	314.94	[^{o}C]	TC Ref. 11 in copper "neck"
$\mathbf{T_{peak\_1}}$	374.97	376.59	[^{o}C]	Peak Copper Temperature TC 1
$\mathbf{T_{peak\_2}}$	375.43	377.05	[^{o}C]	Peak Copper Temperature TC 2

Table B.9: 2211

	Run 1	Run 2	Units	Description
$\dot{m}$	8.84	8.84	[g/s]	Measured Mass Flow Rate
Re	12,390	12,390	[-]	Jet Reynolds Number
$\mathbf{Q_{in}}$	377.6	376.8	[W]	Nominal Power Input
$\mathbf{Q_{out}}$	353.4	344.8	[W]	Power Out = $\dot{m}\, c_p(T_{out} - T_{in})$
% Losses	6%	8%	[-]	Heat Loss
q''_{actual}	0.226	0.226	[MW/m^2]	Incident Heat Flux
$\mathbf{P_{rot}}$	50	50	[psig]	Rotameter Pressure
$\mathbf{P_{out}}$	47	47	[psig]	Outlet Pressure
ΔP	1.38	1.35	[psi]	Measured Pressure Drop
$\mathbf{T_{in}}$	22.43	22.49	[^{o}C]	Inlet Temperature
$\mathbf{T_{out}}$	61.90	61.00	[^{o}C]	Outlet Temperature
$\mathbf{T_1}$	90.19	91.13	[^{o}C]	Embedded TC Ref. 1 in brass
$\mathbf{T_2}$	96.22	97.40	[^{o}C]	Embedded TC Ref. 2 in brass
$\mathbf{T_3}$	89.34	91.00	[^{o}C]	Embedded TC Ref. 3 in brass
$\mathbf{T_4}$	90.47	89.59	[^{o}C]	Embedded TC Ref. 4 in brass
$\mathbf{T_5}$	89.87	91.00	[^{o}C]	Embedded TC Ref. 5 in brass
$\mathbf{T_6}$	113.85	116.80	[^{o}C]	TC Ref. 6 in copper "neck"
$\mathbf{T_7}$	116.59	119.28	[^{o}C]	TC Ref. 7 in copper "neck"
$\mathbf{T_8}$	119.73	122.29	[^{o}C]	TC Ref. 8 in copper "neck"
$\mathbf{T_9}$	113.99	116.46	[^{o}C]	TC Ref. 9 in copper "neck"
$\mathbf{T_{10}}$	116.39	119.05	[^{o}C]	TC Ref. 10 in copper "neck"
$\mathbf{T_{11}}$	119.49	122.11	[^{o}C]	TC Ref. 11 in copper "neck"
$\mathbf{T_{peak\_1}}$	139.79	142.39	[^{o}C]	Peak Copper Temperature TC 1
$\mathbf{T_{peak\_2}}$	139.90	142.48	[^{o}C]	Peak Copper Temperature TC 2

Table B.10: 1211

	Run 1	Run 2	Units	Description
$\dot{m}$	8.99	8.99	[g/s]	Measured Mass Flow Rate
Re	12,590	12,590	[-]	Jet Reynolds Number
$\mathbf{Q_{in}}$	377.9	383.1	[W]	Nominal Power Input
$\mathbf{Q_{out}}$	355.6	375.3	[W]	Power Out = $\dot{m}\, c_p(T_{out} - T_{in})$
% Losses	6%	2%	[-]	Heat Loss
q''_{actual}	0.226	0.229	[MW/m^2]	Incident Heat Flux
$\mathbf{P_{rot}}$	62	62	[psig]	Rotameter Pressure
$\mathbf{P_{out}}$	60	60	[psig]	Outlet Pressure
ΔP	0.267	0.344	[psi]	Measured Pressure Drop
$\mathbf{T_{in}}$	23.23	19.19	[^{o}C]	Inlet Temperature
$\mathbf{T_{out}}$	62.30	60.42	[^{o}C]	Outlet Temperature
$\mathbf{T_1}$	87.41	86.59	[^{o}C]	Embedded TC Ref. 1 in brass
$\mathbf{T_2}$	87.80	87.18	[^{o}C]	Embedded TC Ref. 2 in brass
$\mathbf{T_3}$	87.01	86.18	[^{o}C]	Embedded TC Ref. 3 in brass
$\mathbf{T_4}$	86.20	85.37	[^{o}C]	Embedded TC Ref. 4 in brass
$\mathbf{T_5}$	86.61	85.8	[^{o}C]	Embedded TC Ref. 5 in brass
$\mathbf{T_6}$	105.83	105.26	[^{o}C]	TC Ref. 6 in copper "neck"
$\mathbf{T_7}$	108.58	108.12	[^{o}C]	TC Ref. 7 in copper "neck"
$\mathbf{T_8}$	111.23	110.85	[^{o}C]	TC Ref. 8 in copper "neck"
$\mathbf{T_9}$	105.28	104.75	[^{o}C]	TC Ref. 9 in copper "neck"
$\mathbf{T_{10}}$	107.65	107.20	[^{o}C]	TC Ref. 10 in copper "neck"
$\mathbf{T_{11}}$	110.75	110.37	[^{o}C]	TC Ref. 11 in copper "neck"
$\mathbf{T_{peak\_1}}$	131.10	131.34	[^{o}C]	Peak Copper Temperature TC 1
$\mathbf{T_{peak\_2}}$	131.19	131.43	[^{o}C]	Peak Copper Temperature TC 2

Table B.11: 2222

	Run 1	Run 2	Units	Description
$\dot{m}$	21.89	21.89	[g/s]	Measured Mass Flow Rate
Re	30,708	30,708	[-]	Jet Reynolds Number
$\mathbf{Q_{in}}$	809.0	811.6	[W]	Nominal Power Input
$\mathbf{Q_{out}}$	704.8	672.8	[W]	Power Out = $\dot{m}\, c_p(T_{out} - T_{in})$
% Losses	13%	17%	[-]	Heat Loss
q''_{actual}	0.484	0.486	[MW/m^2]	Incident Heat Flux
$\mathbf{P_{rot}}$	36	36	[psig]	Rotameter Pressure
$\mathbf{P_{out}}$	14	14	[psig]	Outlet Pressure
ΔP	18.41	17.74	[psi]	Measured Pressure Drop
$\mathbf{T_{in}}$	21.83	21.89	[^{o}C]	Inlet Temperature
$\mathbf{T_{out}}$	53.61	52.23	[^{o}C]	Outlet Temperature
$\mathbf{T_1}$	102.59	104.28	[^{o}C]	Embedded TC Ref. 1 in brass
$\mathbf{T_2}$	112.34	114.46	[^{o}C]	Embedded TC Ref. 2 in brass
$\mathbf{T_3}$	101.15	104.84	[^{o}C]	Embedded TC Ref. 3 in brass
$\mathbf{T_4}$	101.52	100.01	[^{o}C]	Embedded TC Ref. 4 in brass
$\mathbf{T_5}$	101.41	103.27	[^{o}C]	Embedded TC Ref. 5 in brass
$\mathbf{T_6}$	151.51	157.81	[^{o}C]	TC Ref. 6 in copper "neck"
$\mathbf{T_7}$	156.94	162.66	[^{o}C]	TC Ref. 7 in copper "neck"
$\mathbf{T_8}$	163.40	168.95	[^{o}C]	TC Ref. 8 in copper "neck"
$\mathbf{T_9}$	151.80	157.27	[^{o}C]	TC Ref. 9 in copper "neck"
$\mathbf{T_{10}}$	156.95	162.79	[^{o}C]	TC Ref. 10 in copper "neck"
$\mathbf{T_{11}}$	163.36	169.09	[^{o}C]	TC Ref. 11 in copper "neck"
$\mathbf{T_{peak\_1}}$	204.72	210.67	[^{o}C]	Peak Copper Temperature TC 1
$\mathbf{T_{peak\_2}}$	204.97	210.86	[^{o}C]	Peak Copper Temperature TC 2

Table B.12: 2223

	Run 1	Run 2	Units	Description
$\dot{m}$	21.89	21.89	[g/s]	Measured Mass Flow Rate
Re	30,708	30,708	[-]	Jet Reynolds Number
$\mathbf{Q_{in}}$	1084.5	1084.6	[W]	Nominal Power Input
$\mathbf{Q_{out}}$	982.6	917.3	[W]	Power Out = $\dot{m}\, c_p(T_{out} - T_{in})$
% Losses	9%	15%	[-]	Heat Loss
q''_{actual}	0.649	0.649	[MW/m^2]	Incident Heat Flux
$\mathbf{P_{rot}}$	36	36	[psig]	Rotameter Pressure
$\mathbf{P_{out}}$	14	14	[psig]	Outlet Pressure
ΔP	18.20	17.76	[psi]	Measured Pressure Drop
$\mathbf{T_{in}}$	21.95	22.12	[^{o}C]	Inlet Temperature
$\mathbf{T_{out}}$	66.26	63.49	[^{o}C]	Outlet Temperature
$\mathbf{T_1}$	130.01	130.37	[^{o}C]	Embedded TC Ref. 1 in brass
$\mathbf{T_2}$	142.30	143.64	[^{o}C]	Embedded TC Ref. 2 in brass
$\mathbf{T_3}$	128.01	130.66	[^{o}C]	Embedded TC Ref. 3 in brass
$\mathbf{T_4}$	128.48	125.40	[^{o}C]	Embedded TC Ref. 4 in brass
$\mathbf{T_5}$	128.15	129.18	[^{o}C]	Embedded TC Ref. 5 in brass
$\mathbf{T_6}$	194.03	199.35	[^{o}C]	TC Ref. 6 in copper "neck"
$\mathbf{T_7}$	201.24	205.89	[^{o}C]	TC Ref. 7 in copper "neck"
$\mathbf{T_8}$	209.82	214.28	[^{o}C]	TC Ref. 8 in copper "neck"
$\mathbf{T_9}$	194.62	198.97	[^{o}C]	TC Ref. 9 in copper "neck"
$\mathbf{T_{10}}$	201.45	206.26	[^{o}C]	TC Ref. 10 in copper "neck"
$\mathbf{T_{11}}$	209.93	214.48	[^{o}C]	TC Ref. 11 in copper "neck"
$\mathbf{T_{peak\_1}}$	264.78	269.19	[^{o}C]	Peak Copper Temperature TC 1
$\mathbf{T_{peak\_2}}$	265.17	269.48	[^{o}C]	Peak Copper Temperature TC 2

Table B.13: 1222

	Run 1	Run 2	Units	Description
$\dot{m}$	25.73	25.73	[g/s]	Measured Mass Flow Rate
Re	36,036	36,063	[-]	Jet Reynolds Number
$\mathbf{Q_{in}}$	832.8	801.5	[W]	Nominal Power Input
$\mathbf{Q_{out}}$	763.0	756.9	[W]	Power Out = $\dot{m}\, c_p(T_{out} - T_{in})$
% Losses	8%	6%	[-]	Heat Loss
q''_{actual}	0.499	0.480	[MW/m^2]	Incident Heat Flux
$\mathbf{P_{rot}}$	52	52	[psig]	Rotameter Pressure
$\mathbf{P_{out}}$	39	39	[psig]	Outlet Pressure
ΔP	9.062	0.344	[psi]	Measured Pressure Drop
$\mathbf{T_{in}}$	22.50	19.26	[^{o}C]	Inlet Temperature
$\mathbf{T_{out}}$	51.77	48.30	[^{o}C]	Outlet Temperature
$\mathbf{T_1}$	95.47	91.51	[^{o}C]	Embedded TC Ref. 1 in brass
$\mathbf{T_2}$	96.53	92.54	[^{o}C]	Embedded TC Ref. 2 in brass
$\mathbf{T_3}$	94.50	90.57	[^{o}C]	Embedded TC Ref. 3 in brass
$\mathbf{T_4}$	93.33	89.51	[^{o}C]	Embedded TC Ref. 4 in brass
$\mathbf{T_5}$	94.62	90.76	[^{o}C]	Embedded TC Ref. 5 in brass
$\mathbf{T_6}$	135.89	131.07	[^{o}C]	TC Ref. 6 in copper "neck"
$\mathbf{T_7}$	141.44	136.51	[^{o}C]	TC Ref. 7 in copper "neck"
$\mathbf{T_8}$	147.09	142.11	[^{o}C]	TC Ref. 8 in copper "neck"
$\mathbf{T_9}$	134.75	129.98	[^{o}C]	TC Ref. 9 in copper "neck"
$\mathbf{T_{10}}$	139.93	135.04	[^{o}C]	TC Ref. 10 in copper "neck"
$\mathbf{T_{11}}$	146.48	141.50	[^{o}C]	TC Ref. 11 in copper "neck"
$\mathbf{T_{peak\_1}}$	189.52	183.75	[^{o}C]	Peak Copper Temperature TC 1
$\mathbf{T_{peak\_2}}$	189.75	183.92	[^{o}C]	Peak Copper Temperature TC 2

Table B.14: 1223

	Run 1	Run 2	Units	Description
$\dot{m}$	25.73	20.58	[g/s]	Measured Mass Flow Rate
Re	36,063	28,860	[-]	Jet Reynolds Number
$\mathbf{Q_{in}}$	1077.7	1081.3	[W]	Nominal Power Input
$\mathbf{Q_{out}}$	989.6	987.3	[W]	Power Out = $\dot{m}\, c_p(T_{out} - T_{in})$
% Losses	8%	9%	[-]	Heat Loss
q''_{actual}	0.645	0.647	[MW/m^2]	Incident Heat Flux
$\mathbf{P_{rot}}$	52	40	[psig]	Rotameter Pressure
$\mathbf{P_{out}}$	39	30	[psig]	Outlet Pressure
ΔP	8.91	7.30	[psi]	Measured Pressure Drop
$\mathbf{T_{in}}$	22.52	22.74	[^{o}C]	Inlet Temperature
$\mathbf{T_{out}}$	60.49	70.09	[^{o}C]	Outlet Temperature
$\mathbf{T_1}$	115.16	127.24	[^{o}C]	Embedded TC Ref. 1 in brass
$\mathbf{T_2}$	116.14	128.19	[^{o}C]	Embedded TC Ref. 2 in brass
$\mathbf{T_3}$	113.83	125.72	[^{o}C]	Embedded TC Ref. 3 in brass
$\mathbf{T_4}$	112.40	124.52	[^{o}C]	Embedded TC Ref. 4 in brass
$\mathbf{T_5}$	113.96	126.09	[^{o}C]	Embedded TC Ref. 5 in brass
$\mathbf{T_6}$	166.58	177.99	[^{o}C]	TC Ref. 6 in copper "neck"
$\mathbf{T_7}$	173.55	185.07	[^{o}C]	TC Ref. 7 in copper "neck"
$\mathbf{T_8}$	180.71	192.30	[^{o}C]	TC Ref. 8 in copper "neck"
$\mathbf{T_9}$	165.13	176.69	[^{o}C]	TC Ref. 9 in copper "neck"
$\mathbf{T_{10}}$	171.73	183.28	[^{o}C]	TC Ref. 10 in copper "neck"
$\mathbf{T_{11}}$	179.94	191.53	[^{o}C]	TC Ref. 11 in copper "neck"
$\mathbf{T_{peak\_1}}$	234.48	246.36	[^{o}C]	Peak Copper Temperature TC 1
$\mathbf{T_{peak\_2}}$	234.80	246.67	[^{o}C]	Peak Copper Temperature TC 2

Table B.15: 1233

	Run 1	Run 2	Units	Description
$\dot{m}$	32.49	34.67	[g/s]	Measured Mass Flow Rate
Re	45,537	48,594	[-]	Jet Reynolds Number
$\mathbf{Q_{in}}$	1043.7	1027.6	[W]	Nominal Power Input
$\mathbf{Q_{out}}$	916.1	852.1	[W]	Power Out = $\dot{m}\, c_p(T_{out} - T_{in})$
% Losses	12%	17%	[-]	Heat Loss
q''_{actual}	0.625	0.615	[MW/m^2]	Incident Heat Flux
$\mathbf{P_{rot}}$	52	58	[psig]	Rotameter Pressure
$\mathbf{P_{out}}$	31	30	[psig]	Outlet Pressure
ΔP	22.74	22.58	[psi]	Measured Pressure Drop
$\mathbf{T_{in}}$	22.58	22.15	[^{o}C]	Inlet Temperature
$\mathbf{T_{out}}$	50.41	46.41	[^{o}C]	Outlet Temperature
$\mathbf{T_1}$	102.61	102.30	[^{o}C]	Embedded TC Ref. 1 in brass
$\mathbf{T_2}$	104.24	105.15	[^{o}C]	Embedded TC Ref. 2 in brass
$\mathbf{T_3}$	101.62	96.92	[^{o}C]	Embedded TC Ref. 3 in brass
$\mathbf{T_4}$	100.38	98.24	[^{o}C]	Embedded TC Ref. 4 in brass
$\mathbf{T_5}$	101.90	101.00	[^{o}C]	Embedded TC Ref. 5 in brass
$\mathbf{T_6}$	153.16	163.94	[^{o}C]	TC Ref. 6 in copper "neck"
$\mathbf{T_7}$	160.00	171.02	[^{o}C]	TC Ref. 7 in copper "neck"
$\mathbf{T_8}$	167.10	179.54	[^{o}C]	TC Ref. 8 in copper "neck"
$\mathbf{T_9}$	151.79	164.49	[^{o}C]	TC Ref. 9 in copper "neck"
$\mathbf{T_{10}}$	158.28	171.01	[^{o}C]	TC Ref. 10 in copper "neck"
$\mathbf{T_{11}}$	166.38	179.77	[^{o}C]	TC Ref. 11 in copper "neck"
$\mathbf{T_{peak\_1}}$	219.99	232.41	[^{o}C]	Peak Copper Temperature TC 1
$\mathbf{T_{peak\_2}}$	220.26	232.54	[^{o}C]	Peak Copper Temperature TC 2

Table B.16: 1234

	Run 1	Run 2	Units	Description
$\dot{m}$	32.49	34.67	[g/s]	Measured Mass Flow Rate
Re	45,537	48,594	[-]	Jet Reynolds Number
$\mathbf{Q_{in}}$	1265.3	1248.6	[W]	Nominal Power Input
$\mathbf{Q_{out}}$	1119.4	1050.9	[W]	Power Out = $\dot{m}\, c_p(T_{out} - T_{in})$
% Losses	12%	16%	[-]	Heat Loss
q''_{actual}	0.758	0.748	[MW/m^2]	Incident Heat Flux
$\mathbf{P_{rot}}$	52	58	[psig]	Rotameter Pressure
$\mathbf{P_{out}}$	31	30	[psig]	Outlet Pressure
ΔP	22.74	22.56	[psi]	Measured Pressure Drop
$\mathbf{T_{in}}$	22.66	22.41	[^{o}C]	Inlet Temperature
$\mathbf{T_{out}}$	56.67	52.33	[^{o}C]	Outlet Temperature
$\mathbf{T_1}$	118.14	119.21	[^{o}C]	Embedded TC Ref. 1 in brass
$\mathbf{T_2}$	120.09	122.43	[^{o}C]	Embedded TC Ref. 2 in brass
$\mathbf{T_3}$	116.86	112.20	[^{o}C]	Embedded TC Ref. 3 in brass
$\mathbf{T_4}$	115.38	113.80	[^{o}C]	Embedded TC Ref. 4 in brass
$\mathbf{T_5}$	117.19	117.12	[^{o}C]	Embedded TC Ref. 5 in brass
$\mathbf{T_6}$	178.83	193.36	[^{o}C]	TC Ref. 6 in copper "neck"
$\mathbf{T_7}$	187.00	201.90	[^{o}C]	TC Ref. 7 in copper "neck"
$\mathbf{T_8}$	195.47	212.17	[^{o}C]	TC Ref. 8 in copper "neck"
$\mathbf{T_9}$	177.24	194.52	[^{o}C]	TC Ref. 9 in copper "neck"
$\mathbf{T_{10}}$	185.02	202.40	[^{o}C]	TC Ref. 10 in copper "neck"
$\mathbf{T_{11}}$	194.70	212.96	[^{o}C]	TC Ref. 11 in copper "neck"
$\mathbf{T_{peak\_1}}$	258.88	276.20	[^{o}C]	Peak Copper Temperature TC 1
$\mathbf{T_{peak\_2}}$	259.26	276.48	[^{o}C]	Peak Copper Temperature TC 2

Table B.17: 2233

	Run 1	Run 2	Units	Description
$\dot{m}$	33.34	33.34	[g/s]	Measured Mass Flow Rate
Re	46,723	46,723	[-]	Jet Reynolds Number
$\mathbf{Q_{in}}$	1037.5	1047.9	[W]	Nominal Power Input
$\mathbf{Q_{out}}$	857.9	882.3	[W]	Power Out = $\dot{m}\, c_p(T_{out} - T_{in})$
% Losses	17%	16%	[-]	Heat Loss
q''_{actual}	0.621	0.627	[MW/m^2]	Incident Heat Flux
$\mathbf{P_{rot}}$	59	59	[psig]	Rotameter Pressure
$\mathbf{P_{out}}$	28	28	[psig]	Outlet Pressure
ΔP	25.55	25.51	[psi]	Measured Pressure Drop
$\mathbf{T_{in}}$	22.6	22.73	[^{o}C]	Inlet Temperature
$\mathbf{T_{out}}$	48.0	48.86	[^{o}C]	Outlet Temperature
$\mathbf{T_1}$	111.57	111.94	[^{o}C]	Embedded TC Ref. 1 in brass
$\mathbf{T_2}$	111.84	112.16	[^{o}C]	Embedded TC Ref. 2 in brass
$\mathbf{T_3}$	110.54	111.49	[^{o}C]	Embedded TC Ref. 3 in brass
$\mathbf{T_4}$	111.02	112.35	[^{o}C]	Embedded TC Ref. 4 in brass
$\mathbf{T_5}$	111.93	111.75	[^{o}C]	Embedded TC Ref. 5 in brass
$\mathbf{T_6}$	171.90	172.83	[^{o}C]	TC Ref. 6 in copper "neck"
$\mathbf{T_7}$	179.32	180.32	[^{o}C]	TC Ref. 7 in copper "neck"
$\mathbf{T_8}$	188.11	189.23	[^{o}C]	TC Ref. 8 in copper "neck"
$\mathbf{T_9}$	172.08	172.78	[^{o}C]	TC Ref. 9 in copper "neck"
$\mathbf{T_{10}}$	178.75	179.49	[^{o}C]	TC Ref. 10 in copper "neck"
$\mathbf{T_{11}}$	187.82	188.73	[^{o}C]	TC Ref. 11 in copper "neck"
$\mathbf{T_{peak\_1}}$	241.21	243.45	[^{o}C]	Peak Copper Temperature TC 1
$\mathbf{T_{peak\_2}}$	241.40	243.68	[^{o}C]	Peak Copper Temperature TC 2

Table B.18: 2234

	Run 1	Run 2	Units	Description
$\dot{m}$	33.34	33.34	[g/s]	Measured Mass Flow Rate
Re	46,723	46,723	[-]	Jet Reynolds Number
$\mathbf{Q_{in}}$	1247.3	1239.2	[W]	Nominal Power Input
$\mathbf{Q_{out}}$	1043.5	1031.8	[W]	Power Out = $\dot{m}\, c_p(T_{out} - T_{in})$
% Losses	16%	17%	[-]	Heat Loss
q''_{actual}	0.747	0.742	[MW/m^2]	Incident Heat Flux
$\mathbf{P_{rot}}$	59	59	[psig]	Rotameter Pressure
$\mathbf{P_{out}}$	28	28	[psig]	Outlet Pressure
ΔP	25.53	25.45	[psi]	Measured Pressure Drop
$\mathbf{T_{in}}$	22.77	22.66	[^{o}C]	Inlet Temperature
$\mathbf{T_{out}}$	53.67	53.21	[^{o}C]	Outlet Temperature
$\mathbf{T_1}$	128.60	125.21	[^{o}C]	Embedded TC Ref. 1 in brass
$\mathbf{T_2}$	128.53	125.07	[^{o}C]	Embedded TC Ref. 2 in brass
$\mathbf{T_3}$	127.28	124.49	[^{o}C]	Embedded TC Ref. 3 in brass
$\mathbf{T_4}$	127.27	124.24	[^{o}C]	Embedded TC Ref. 4 in brass
$\mathbf{T_5}$	128.36	125.00	[^{o}C]	Embedded TC Ref. 5 in brass
$\mathbf{T_6}$	199.91	194.31	[^{o}C]	TC Ref. 6 in copper "neck"
$\mathbf{T_7}$	208.71	202.89	[^{o}C]	TC Ref. 7 in copper "neck"
$\mathbf{T_8}$	219.13	213.05	[^{o}C]	TC Ref. 8 in copper "neck"
$\mathbf{T_9}$	200.52	194.45	[^{o}C]	TC Ref. 9 in copper "neck"
$\mathbf{T_{10}}$	208.53	202.20	[^{o}C]	TC Ref. 10 in copper "neck"
$\mathbf{T_{11}}$	219.27	212.72	[^{o}C]	TC Ref. 11 in copper "neck"
$\mathbf{T_{peak\_1}}$	282.65	275.30	[^{o}C]	Peak Copper Temperature TC 1
$\mathbf{T_{peak\_2}}$	282.94	275.60	[^{o}C]	Peak Copper Temperature TC 2

APPENDIX C: TEMPERATURE PROFILES

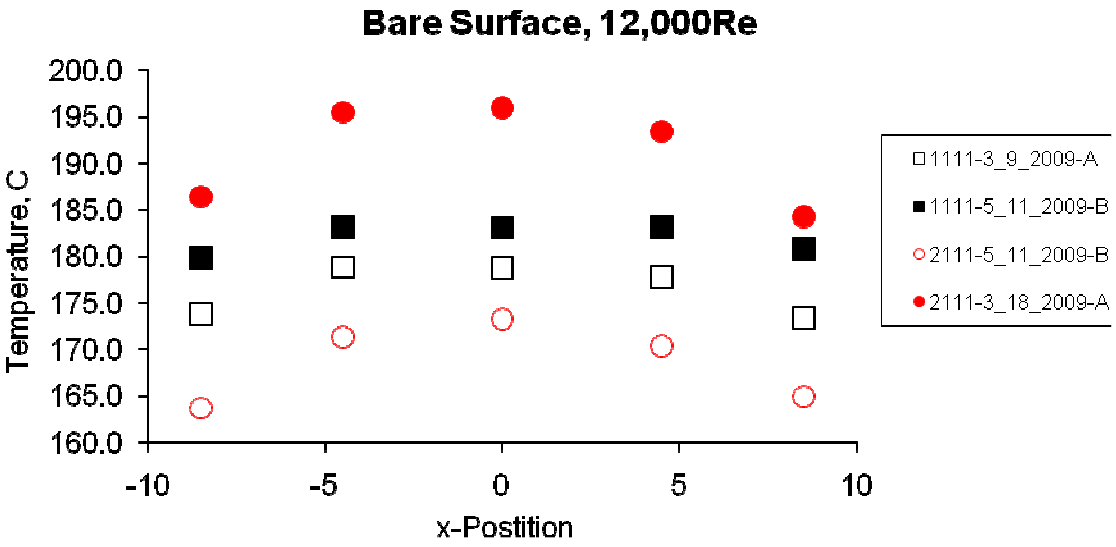

Figure C.1: Temperature Profile; bare surface, 12,000 Re

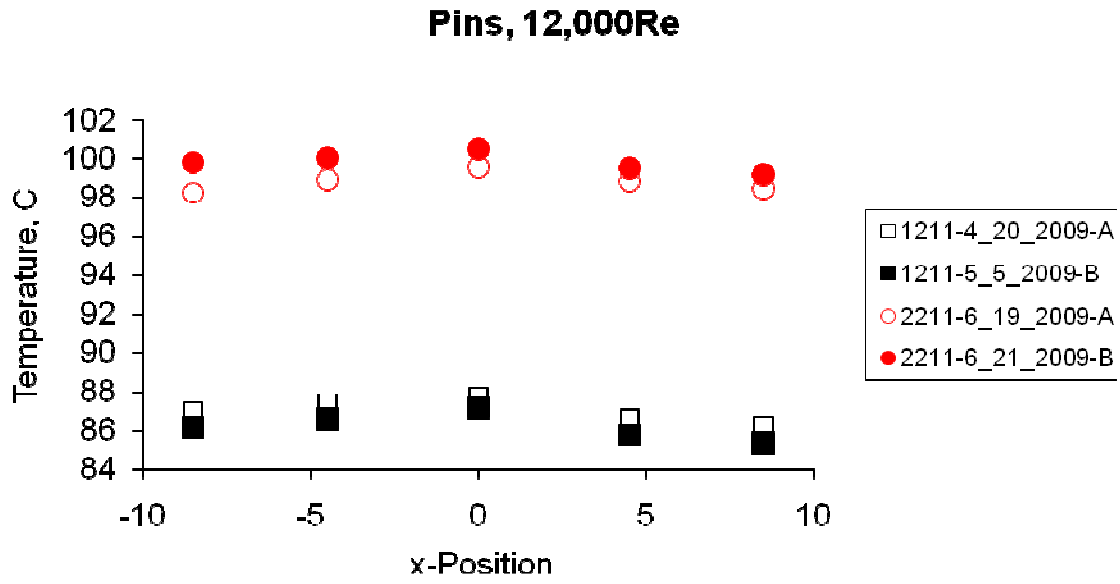

Figure C.2: Temperature profile; pins, 12,000 Re

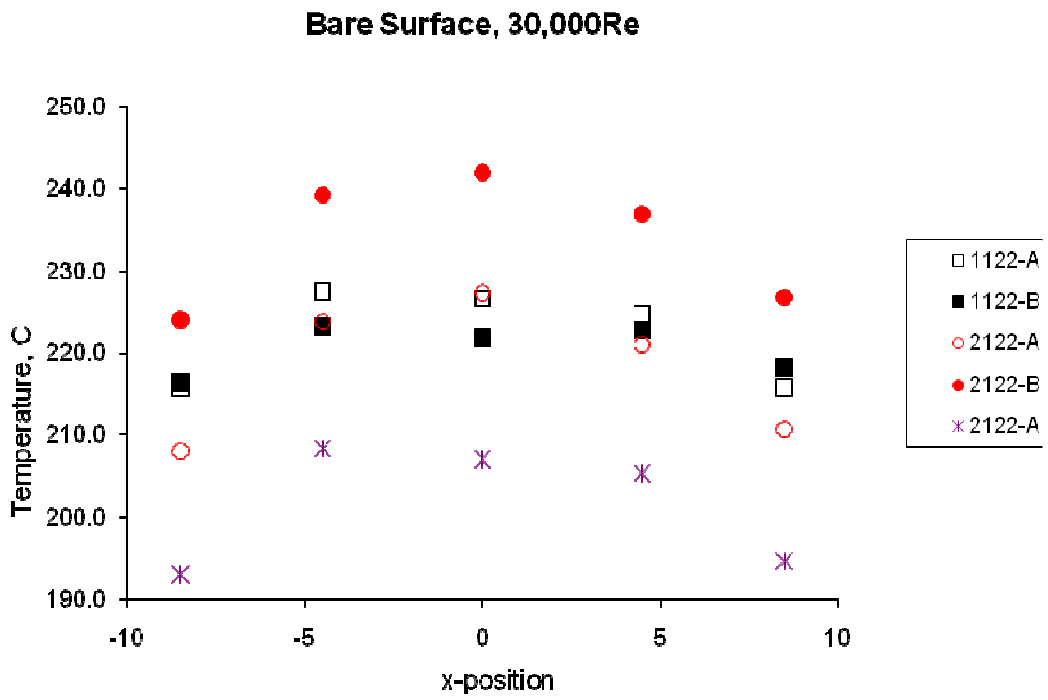

Figure C.3: Temperature profile; bare surface, 30,000 Re

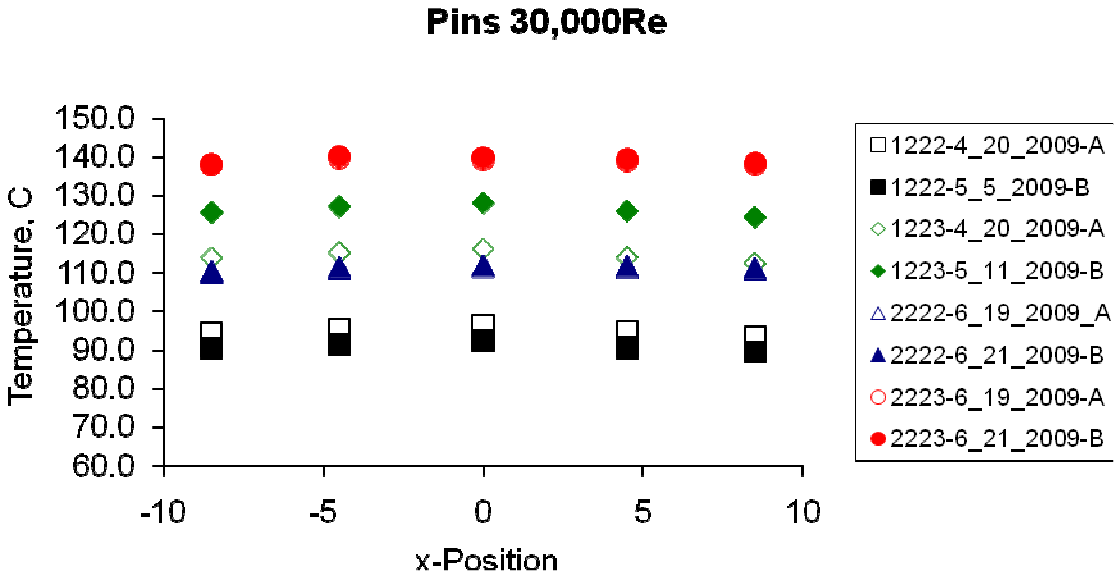

Figure C.4: Temperature profile; pins, 30,000 Re

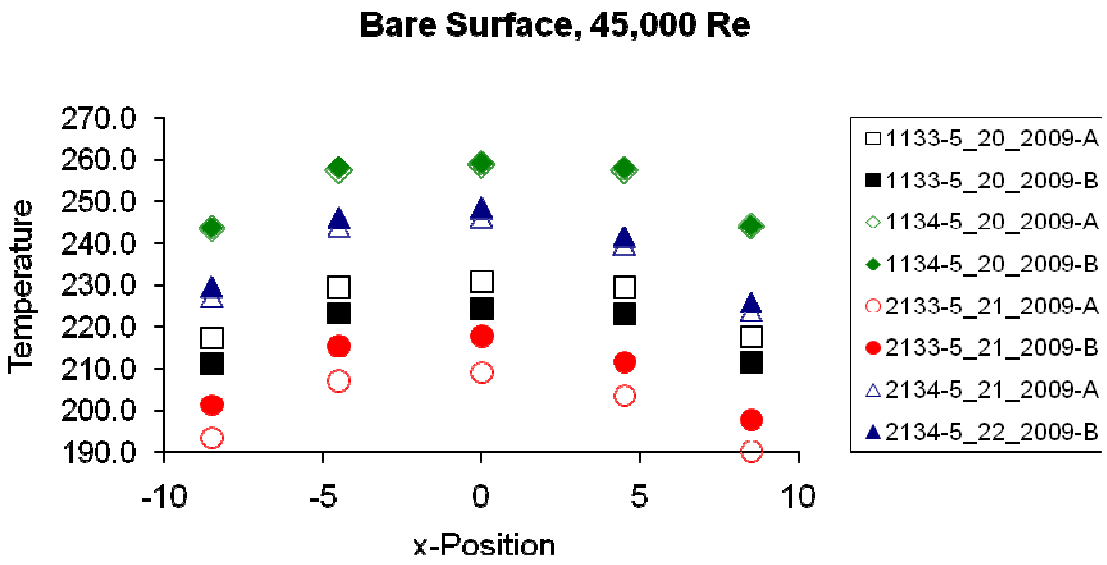

Figure C.5: Temperature profile; bare surface, 45,000 Re

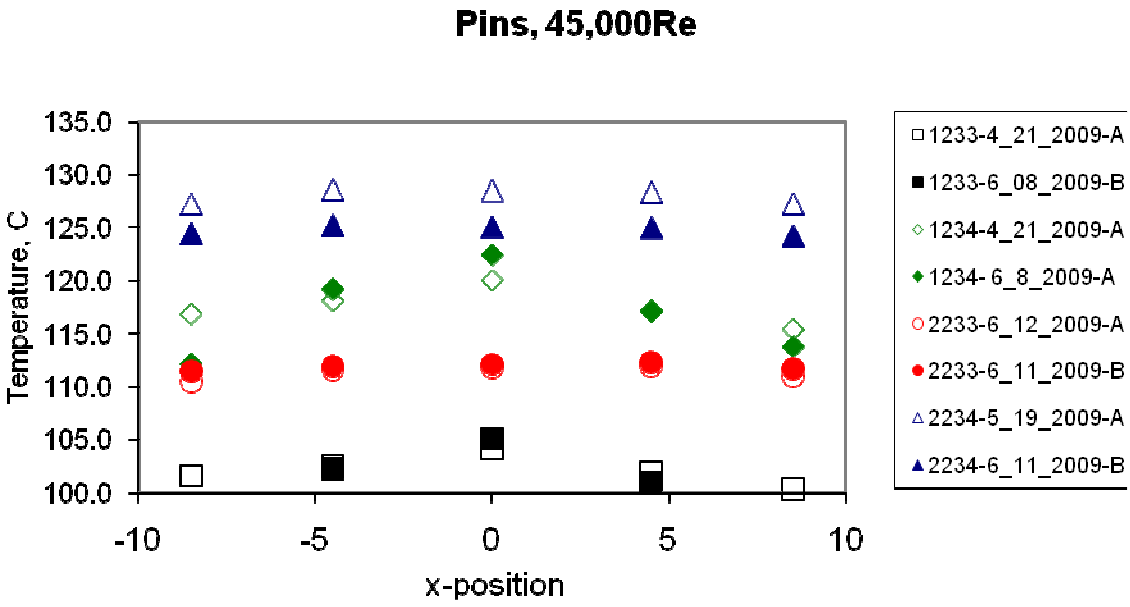

Figure C.6: Temperature profile; pins, 45,000 Re

BIBLIOGRAPHY

[1] C.B. Baxi, and C. Wong, "Review of helium cooling for fusion reactor applications" *Fusion Engineering and Design*, vols. 51-52: pp. 319-324, 2000.

[2] L.V. Boccaccini, et al. "He-cooled divertor concepts" In US-Japan workshop on fusion power plants and related advanced technologies, Tokyo, Japan, 11-13 Jan. 2006

[3] L. Crosatti, "Experimental and numerical investigation of gas-cooled divertor modules," Ph.D. thesis Mech. Eng. Dept., GA Tech, Atlanta, GA, 2008.

[4] E. Diegele, R. Krussmann, "Modular He-cooled divertor for power plant application" *Fusion Eng. Des.* vol. 66-68, pp. 383-387, 2003

[5] R. Gardon and J.C. Akfirat "Heat transfer characteristics of impinging two-dimensional air jets" *J. Heat Transfer*, vol. 88, pp.101-108, 1966

[6] E. Gayton, "Experimental and numerical investigation of the thermal performance of the gas-cooled divertor plate concept," M.S. thesis, Mech. Eng. Dept., GA Tech, Atlanta, GA, 2008.

[7] S. Hermsmeyer, and K. Kleefeldt, "Review and comparative assessment of helium cooled divertor concepts," FZKA 6597, 2001

[8] S. Hermsmeyer, and S. Malang, "Gas-cooled high performance divertor for a power plant" *Fusion Eng. Des*., vol. 197, pp. 61–62, 2002.

[9] T. Ihli, et al., "Design and performance study of the helium-cooled T-tube divertor concept," *Fusion Eng. Des.*, vol. 82, pp. 249–264, 2007.

[10] F. Incropera, and D. DeWitt, "One-Dimensional, Steady State Conduction" and "External Flow," in *Fundamentals of Heat and Mass Transfer*, 6th ed. Hoboken, NJ: John Wiley & Sons, 2007. Ch. 3, pp. 139-154, and Ch. 7, pp. 403-455

[11] ITER. "Official ITER website", June 2009. [http://www.iter.org] accessed June 2009.

[12] K. Kleefeldt, and S. Gordeev, "Performance limits of a helium-cooled divertor (unconventional design)" in FZKA 6401, 2000.

[13] R. Kruessmann, et al. "Conceptual design of a he-cooled divertor with integrated flow and heat transfer promoters" PPCS Subtask TW3-TRP-001-D2, Part II Detailed version, FZKA 6975, 2004

[14] Z.H. Lin, Y.J. Chou, Y.H. Hung, "Heat transfer behaviors of a confined slot jet impingement" *Int. J. Heat Mass Transfer*, vol. 40, pp. 1095-1107, 1997

[15] P. Norajitra, et al, “Development of a helium-cooled divertor concept: design-related requirements on materials and fabrication technology” J. Nuclear Materials Vol 332-333, pp. 1594-1598, 2004

[16]P. Norajitra, et al., “Status of he-cooled divertor development” FZKA 7100, TW4-TRP-001-D2, 2005b.

[17] P. Norajitra, et al., “He-cooled divertor for DEMO: experimental verification of the conceptual modular design,” *Fusion Eng. Des.* vol. 81, pp. 341-346, 2006

[18] Y. Peles, et al., “Forced convective heat transfer across a pin fin micro heat sink,” *J. Heat Transfer* vol. 48 pp. 3615-3627, 2005

[19] A.R. Raffray, et al, “Dynamic chamber armor behavior in IFE and MFE” *Fusion Eng. Des.* Vol. 63-64, pp 597-608, 2002

[20] J.Y. San, and W.Z. Shiao, “Effects of jet plate size and plate spacing on the stagnation nusselt number for a confined circular air jet impinging on a flat plate”. *Int. J. Of Heat And Mass Transfer*, vol. 49, pp. 3477–3486, 2006.

[21] S. Sharafat, et al., “Ultra low pressure-drop helium-cooled porous tungsten PFC,” *Fusion Sci. Tech*. vol. 52, pp. 559-565, 2007.

[22] W.M. Stacey, "Introduction" in An Introduction to the Physics and Technology of Magnetic Confinement Fusion. Atlanta, GA, John Wiley & Sons, 1984, ch. 1, pp. 1-19

[23] S.B. Vardeman, and J.M. Jobe, "Probability: The Mathematics of Randomness" in *Basic Engineering Data Collection and Analysis*, Pacific Grove, CA, Duxbury, 2001, Ch. 5, Sec. 2, pp 249-259

[24] X. R.Wang, et al., "Updates of helium-cooled flat plate divertor design and analysis," *ARIES-Pathways Meeting*, Madison, WI, May 28-29, [http://wwwferp. ucsd.edu/ARIES/MEETINGS/0805/Wang.pdf], accessed September 2008.

[25] X.R. Wang, et al., "Design optimization of high-performance helium-cooled divertor plate concept," *TOFE 18*, San Francisco, CA, Sept. 28 – Oct. 2, 2008b

[26] Frank M. White, "Free turbulence: Jets, Wakes, and Mixing Layers" in Viscous Fluid Flow 2nd ed. New York, NY, McGraw-Hill, Inc., 1991, ch 6, pp. 470-481

[27] K.S. Yang, et al. "A comparative study of the airside performance of heat sinks having pin fin configurations" *Int. J. of Heat and Mass Transfer,* vol. 50, pp. 4661-4667, 2007

[28] M. Yoda, et al., “Studies of the thermal performance of gas-cooled divertors” *US-Japan Workshop*, 2009

[29] D. Zhou and S.J. Lee, “Forced convective heat transfer with impinging rectangular jets” *Int. J. of Heat and Mass Transfer*, vol. 50, pp.1916-1926, May 2007